AN ANALYTIC REPRESENTATIVE ELEMENT RATE DECLINE MODEL WITH FRACTURE AND MATRIX COUPLING IN NATURALLY FRACTURED RESERVOIR DEPLETION

by

Togzhan Mynbayeva

THESIS SUPERVISOR

Dr. Randy Doyle Hazlett

Thesis submitted to the School of Mining and Geosciences of Nazarbayev University in Partial Fulfillment of the Requirements for the Degree of
Master of Science in Petroleum Engineering

Nazarbayev University
16 May 2025

ORIGINALITY STATEMENT

I, Togzhan Mynbayeva, hereby declare that this submission is my own work and to the best of my knowledge it contains no materials previously published or written by another person, or substantial proportions of material which have been accepted for the award of any other degree or diploma at Nazarbayev University or any other educational institution, except where due acknowledgement is made in the thesis.

Any contribution made to the research by others, with whom I have worked at NU or elsewhere is explicitly acknowledged in the thesis.

I also declare that the intellectual content of this thesis is the product of my own work, except to the extent that assistance from others in the project's design and conception or in style, presentation and linguistic expression is acknowledged.

Signed on May 16, 2025

_____

ABSTRACT

Naturally Fractured Reservoirs (NFRs) host significant global hydrocarbon reserves but pose considerable modeling challenges due to their inherent heterogeneity and complex flow dynamics. While dual-porosity concepts are widely used, many analytical models, particularly those employing representative element volumes (REVs) for rate decline analysis, simplify the problem by decoupling the fracture and matrix pressure systems. This often involves assuming instantaneous fracture pressure depletion, which may be misleading in flow regime timing in reservoirs with substantial matrix storage or moderate fracture-to-matrix permeability contrasts (k_f/k_x).

An improved analytical REV model that explicitly couples the transient drainage of the matrix with the transient depletion of the fracture system is developed and validated in this thesis to overcome this limitation. The core novelty lies in incorporating a time-dependent average fracture pressure, $P_f(t)$, as the dynamic boundary condition governing 1D linear matrix flow, relaxing the assumption of instantaneous fracture pressure drop. The model is formulated for a 2D REV consisting of a matrix block penetrated by two parallel symmetric fractures and explicitly includes parameters for matrix block geometry (aspect ratio a/b) and size variations (scaling factor S). Analytical solutions for average system pressure, instantaneous flow rate, and their Bourdet derivatives were derived and implemented numerically using Python programming language.

Model validation confirmed that the new coupled solution converges to previous decoupled results (Hazlett et al., 2024) under limiting conditions of high permeability contrast ($k_f/k_x > 10^4$). However, significant and theoretically expected departures were observed at lower k_f/k_x ratios ($\leq 10^4$) and low fracture volume fractions ($v_f < 0.01$), demonstrating the importance of coupling in these regimes. Sensitivity analyses quantified the influence of key parameters: k_f/k_x primarily controls the transition duration between fracture and matrix linear flow regimes; v_f influences the intercepts of these regimes and transition zone magnitude; matrix aspect ratio (a/b) affects the separation and timing of depletion signatures; and the scaling factor (S) introduces a predictable time shift related to block size. Empirical correlations relating transient diagnostic features to k_f/k_x and v_f were developed. Analysis of heterogeneous mixtures (varying a/b or S) revealed that the presence of even small fractions of slower-draining blocks disproportionately impacts the overall

system response, thus indicating that a simple volume-weighted averaging can be misleading, especially for derivative analysis.

According to this study's findings, the coupled analytical model that was created offers a more physically sound framework for examining the pressure and rate decline in NFRs, particularly in situations where the timescales for matrix depletion and fracture are not widely separated. The explicit inclusion of coupling and geometric factors enhances the understanding of transient behavior and highlights the complex impact of heterogeneity on production signatures.

ACKNOWLEDGEMENTS

I would like to express my deepest gratitude to my thesis supervisor, Dr. Randy Doyle Hazlett, for his exceptional guidance, patience, and unwavering support throughout the course of this research. His expertise and mentorship have been instrumental in shaping the direction and successful completion of this thesis.

I gratefully acknowledge Chevron, USA, and Tengizchevroil (TCO) for their generous financial support, without which this study would not have been possible. This thesis was conducted as part of the funded project (SMG2023005), titled “Mechanical Stratigraphy Research Project.” I also wish to express my gratitude to the American Association of Petroleum Geologists (AAPG) Foundation Grants-in-Aid Program for providing additional financial support that helped facilitate this research.

I am also sincerely thankful to Dr. Milovan Fustic, Dr. Bas den Brok, Byron Haynes, and Dr. Shabeeb Alajmei for their meticulous and thoughtful reviews. Their insightful comments and constructive feedback greatly enhanced the clarity, rigor, and overall quality of this work. I truly appreciate the time and attention they devoted to evaluating my research.

I am especially grateful to my family, friends, fellow research assistants, and colleagues for their enduring encouragement, thoughtful conversations, and steady presence throughout my academic journey.

Finally, I would like to extend my heartfelt thanks to Sanzhar Kalkanbay for his constant support, patience, and belief in me. His presence was a source of strength and reassurance through the most demanding phases of this work.

TABLE OF CONTENTS

LIST OF FIGURES

LIST OF TABLES

1. INTRODUCTION

1.1 Background

The importance of Naturally Fractured Reservoirs (NFRs) cannot be overstated – more than 60% of confirmed global oil reserves and about 40% of natural gas reserves are hosted within fractured carbonate reservoirs (Ahmed, 2019). NFRs are characterized by high hydrocarbon productivity, however their inherent heterogeneity and complexity make them particularly challenging to model. This complexity arises not only from the uncertain geometry and connectivity of the fracture network but also from the multi-scale nature of fracturing (from micro-cracks to large faults) and potential stress-sensitivity effects that can alter fracture permeability during depletion. According to Nelson (2001), ignoring fracture presence is nevertheless a common practice in Exploration & Production (E&P) industry due to technical complications that fracture evaluation, quantification, and modelling implies. This oversight may lead to: 1) significant loss in recovery factor; 2) the application of inappropriate recovery patterns and drilling of unnecessary in-fill wells; 3) inefficient capital expenditure during field development; and 4) improper assessment of economic opportunities (Nelson, 2001). Therefore, identifying the fracture presence as early as possible during field life and developing appropriate field management strategies are crucial.

Modelling fluid flow in NFRs has been a challenging task and a subject of significant research interest since the 1960s. Despite the advancements in numerical simulation nowadays, analytical models remain valuable tools for providing fundamental physical insights, rapid screening of reservoir behavior, validating numerical results, and interpreting well test or production data efficiently. The widely used analytical NFR models developed by Warren & Root (1963) and Kazemi (1969) proposed dual porosity concepts, treating fractures and matrix as distinct continua with fluid transfer occurring between them. The Warren & Root model, a cornerstone in NFR analysis, assumed pseudo-steady state flow from the matrix blocks to the fractures. While groundbreaking, these early models often relied on simplified geometrical representations and transfer functions.

Subsequent research aimed to refine these concepts, introducing transient inter-porosity flow concepts and considering various matrix block shapes and fracture network configurations.

However, many analytical approaches, even more recent ones, introduce simplifying assumptions to maintain tractability. A common simplification, particularly relevant for rate decline analysis using representative elements, involves decoupling the pressure dynamics of the fracture and matrix systems. This is often achieved by assuming an instantaneous or very rapid pressure drop within the high-permeability fracture system, effectively imposing a constant (often zero) pressure boundary condition on the matrix blocks for all time after depletion starts. While this assumption holds reasonably well for reservoirs with extremely high fracture-to-matrix permeability contrasts where fractures deplete orders of magnitude faster than the matrix, it becomes less accurate for systems with moderate permeability contrasts or significant matrix storage contributions. In such cases, the fracture pressure declines gradually, and its transient behavior directly influences the driving force for matrix depletion, meaning that decouples models may misrepresent the timing and shape of the flow regimes observed in well test or production data.

The novelty presented in this thesis lies in addressing this limitation. This thesis develops an analytical representative element model that explicitly couples the transient depletion of the fracture system with the transient drainage of the matrix. Instead of assuming instantaneous fracture depletion, this work incorporates a time-dependent average fracture pressure, $P_f(t)$, as the dynamic boundary condition governing matrix flow. This coupling allows for a more physically realistic representation of the pressure dynamics, particularly crucial for accurately modeling reservoirs where fracture and matrix depletion timescales are not vastly separated. Furthermore, the model explicitly incorporates parameters for matrix block geometry (aspect ratio a/b) and size variations (scaling factor S), allowing for investigation into their influence on the coupled system response and the effects of heterogeneity.

1.2 Objectives of the Thesis

1.2.1 Main Objectives

The main objective of this study is to develop and validate an enhanced analytical representative element (REV) model for pressure and rate decline analysis in naturally fractured reservoirs (NFRs) by incorporating the coupling between fracture depletion and matrix drainage dynamics, relaxing the assumption of instantaneous fracture pressure drop used in prior models.

1.2.2 Specific Objectives

The detailed objectives of this study are to:

- Derive the mathematical formulation for coupled fracture and matrix pressure depletion within a defined REV, considering time-dependent average fracture pressure.
- Develop analytical expressions for average system pressure, instantaneous flow rate, and their corresponding Bourdet derivatives for the coupled model.
- Implement the derived analytical solutions numerically using Python programming language, ensuring convergence and accuracy.
- Validate the new coupled model by comparing its predictions against results from previous decoupled models (e.g., Hazlett et al., 2024) under limiting conditions (high permeability ratios).
- Investigate the conditions (e.g., low permeability ratios, low fracture volume fraction) where the fracture-matrix coupling significantly impacts pressure and rate decline behavior.
- Conduct a sensitivity analysis to evaluate the influence of key reservoir and fracture parameters (permeability ratio, fracture volume fraction, matrix aspect ratio, scaling factor) on the pressure and rate transient responses predicted by the coupled model.
- Explore the impact of reservoir heterogeneity by analyzing the model response for mixtures of matrix blocks with different geometries (a/b) and sizes (S).
- Develop empirical correlations based on sensitivity analysis results to potentially aid in parameter estimation from transient data.

1.3 Scope of Work

This study focuses on the theoretical development and analytical solution of fluid flow in a specific 2D Representative Element Volume (REV) consisting of a matrix block penetrated by parallel fractures.

- The model assumes single-phase, slightly compressible fluid flow under isothermal conditions with constant fluid and rock properties.

- Matrix and fracture properties are considered homogeneous within their respective domains.
- The model employs a spatially averaged, time-dependent fracture pressure as the boundary condition for 1D linear matrix flow.
- Numerical implementation is performed in Python to evaluate the derived analytical solutions.
- Model validation is conducted by comparison with specific published results (Hazlett et al., 2024).
- Sensitivity analyses are performed for specific ranges of permeability ratio (k_f/k_x), fracture volume fraction (v_f), matrix aspect ratio (a/b), and scaling factor (S).
- Heterogeneity is explored using simple volume-weighted mixtures of two distinct matrix block types (differing in a/b or S).
- The study does not include simulation using numerical reservoir simulators or application to real field data.

2. LITERATURE REVIEW

2.1 Introduction to Fractures and Naturally Fractured Reservoirs

2.1.1 Definition of a Fracture and its Types

Fractures are a fundamental geological feature that play a crucial role in shaping fluid flow behavior in reservoirs. In hydrocarbon-bearing formations, fractures may enhance or even serve as main pathways for fluid flow, or they may hinder it by creating flow barriers and anisotropy. Naturally Fractured Reservoirs (NFRs) are reservoirs where fractures play a dominant role in hydrocarbon storage and transport, distinguishing them from conventional reservoirs. This section provides an overview of fractures, their classification, and the development of NFR classification systems.

The term "Fracture" is quite generic and can be defined differently by different disciplines. In geological context, the most common definition of a fracture is "a discontinuity or parting in a material caused by brittle failure" and can be detected on various ranges of scales: from micrometers up to several kilometers (Narr, Schechter, & Thompson, 2006). However, this definition is rather broad and may refer to both natural and induced fractures, as well as various types of fractures, such as joints, faults, cracks, veins, etc. The definitions of common fracture types are adopted from Narr, Schechter, & Thompson (2006) and summarized in Table 1.

Table 1. Definitions of fracture types, adopted from Narr, Schechter & Thompson *(2006)*

Fracture Term	**Definition**
Fracture	Discontinuity or parting in a material caused by brittle failure.
Joint	One of a set of parallel extensional fractures with no shearing offset. Multiple set of joints is referred as "joint system" or "joint cluster".
Fault	A shear fracture with a displacement parallel to fracture surface.

Deformation band	Planar fractures formed due to failure and contain crushed particles from the host rock and have braided appearance. They also can be observed as small shear offset faults and tend to form conjugate sets.
Crack	Individual isolated fractures with both natural or induced origin and no shearing offset.
Vein	A mineral-filled fracture

Since fractures may be observed both on outcrops and in the subsurface, it is important to define fractures in a reservoir context due to the scope of the current study. Nelson (2001) defined "Reservoir Fracture" as "a macroscopic planar discontinuity in rock of natural origin, formed due to deformation or physical diagenesis".

There are two main naturally occurring fracture types with which we are concerned in a reservoir: joints and faults. Joints are extension fractures that are parallel (or at high angle) to the bedding plane with no shearing offset and often appearing as a set or cluster; whereas faults are shear fractures with a displacement parallel to fracture surface (Narr, Schechter, & Thompson, 2006). The illustration of difference between joints and faults can be seen in Figure 1.

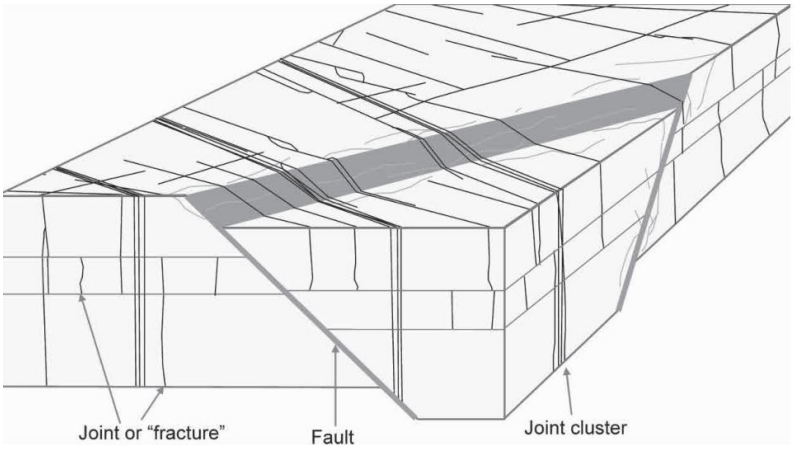

Figure 1. Illustration of joints and a fault *(Narr, Schechter, & Thompson, 2006)*

In the context of reservoir engineering, fractures are assessed in terms of their ability to either contribute or hinder the fluid flow. Joints represent the primary set of fractures that contribute to

the reservoir fluid flow, as they are typically open and form a well-connected fracture network. On the other hand, faults can either facilitate or hinder fluid movement through the reservoir rock, depending on their degree of openness and the material's composition and texture present within fault zone. Since faults may act as flow barriers, they are common cause of formation of compartmentalized reservoirs. Understanding these fracture type differences is essential in evaluating fractured reservoirs, as fracture connectivity and permeability strongly influence reservoir performance. In cases where the presence and behavior of fractures are dominant, they define a distinct category of reservoirs—Naturally Fractured Reservoirs (NFRs).

2.1.2 NFR Definition and Development of Classification System

Naturally Fractured Reservoir (NFR) is defined as "a reservoir in which naturally occurring fractures either have, or are predicted to have, a significant effect on reservoir fluid flow either in the form of increased reservoir permeability and/or reserves or increased permeability anisotropy" (Nelson, 2001).

Since NFRs vastly vary in their fracture and matrix characteristics, several researchers have proposed classification schemes to distinguish different types of NFRs based on fracture contribution to permeability and storage.

The first attempt to classify NFRs was made by McNaughton & Garb in 1975, who categorized them based on fractures capacity to store reservoir fluid without considering fracture and matrix permeability. Their classification consisted of three types of NFRs—A, B, and C. Later in 1983, Aguilera expanded McNaughton & Garb's classification and classified Type B reservoirs into two subtypes by introducing matrix permeability. Therefore, Type B-I reservoirs feature low matrix porosity but possess enough matrix permeability that ensures efficient fluid transfer from matrix to fracture. In contrast, Type B-II reservoirs exhibit both low matrix porosity and permeability which is insufficient for fluid production from the matrix.

Building on this framework, Nelson (2001) modified the classification by considering variations in both matrix and fracture permeability and porosity relative to each other. His classification consisted of four types of NFRs – I, II, III, and IV. The illustration of this classification can be seen in Figure 2. From the illustration, it can be seen that the reservoirs where fractures mainly

control fluid storage and movement are classified as Type I, and these reservoirs are known to have sharp production decline as well as early water or gas coning. Type II reservoirs have fractures that mainly control fluid flow across the reservoir, but the fluid storage is split between fracture and matrix. The quality of these reservoirs depends on the matrix permeability, as low matrix permeability will hinder fluid production stored in matrix and fluid from fractures will be produced only; whereas reservoirs with sufficiently high matrix permeability will enhance fluid production considerably. This concept is similar to reservoirs of Types B-I and B-II introduced by Aguilera (1983). Fractures in Type III reservoirs enhance fluid movement in the reservoir along with the matrix, but do not essentially contribute to the fluid storage, compared to the matrix. Type III reservoirs are the equivalent of conventional reservoirs, where the presence of fractures does not play a significant role in fluid production. Finally, Type IV fractures do not have any contribution to the fluid flow as well as fluid storage, as they rather act as flow barriers and compartmentalize reservoir. Nelson's classification is the most widely used one to this day.

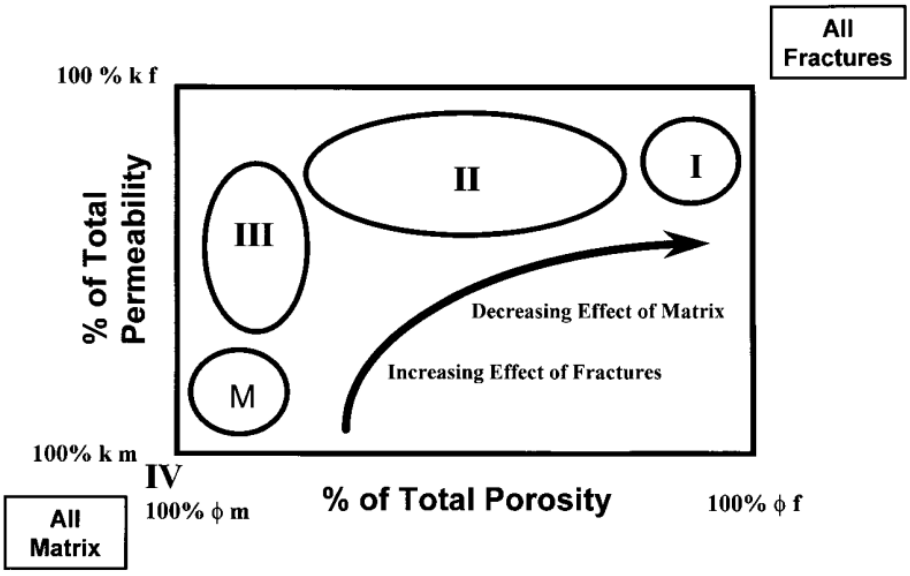

Figure 2. NFR Classification by Nelson (2001)

Later in 2021, Sun & Politt presented their own classification based of their empirical study of NFRs all over the world. Study by Sun & Politt (2021) covered 310 fractured reservoirs all over the world and considered each reservoir case by case with the focus on specific geological and petrophysical characteristics of each reservoir, their production history and applied field management strategies, and ultimate oil recovery achieved. Based on this comprehensive analysis, they developed their own classification, which serves as an intermediate framework between the

models proposed by Nelson (2001) and McNaughton & Garb (1975). A summary comparison of these three classification systems is presented in Table 2. It can be seen that Sun & Politt (2021) classification is more detailed and based of empirically defined matrix porosity threshold, whereas classifications by Nelson (2001) and McNaughton & Garb (1975) were more conceptual.

Table 2. Comparison of different NFR classifications by Sun & Politt *(2021)*

Nelson (2001)	**McNaughton & Garb** (1975)	**Sun & Politt** (2021)
Type I – Fractures provide the essential reservoir porosity and permeability.	Type C – Storage capacity entirely within fractures.	Type 1 – tight matrix: fractures and solution-enhanced fracture porosity provide both storage capacity and fluid-flow pathways.
Type II – Fractures provide the essential reservoir permeability.	Type B – Storage capacity split between fractures and matrix.	Type 2 – macroporous (>20 μm pore size) matrix provides the primary storage capacity while fractures and solution-enhanced fracture porosity provide essential fluid-flow pathways.
	Type A – great majority of storage capacity in the rock matrix.	Type 3 – microporous (<20 μm pore size) matrix provides all storage capacity while fractures only provide essential fluid-flow pathways.
Type III – Fractures assist permeability in an already producible reservoir.	Not included in the classification	Included in Type 2 of this classification
Type IV – Fractures provide no additional porosity or permeability but create significant reservoir anisotropy (barriers).	Not included in the classification	Not included in the classification

In addition to their classification, Sun & Politt (2021) provided a summary of key reservoir characteristics for each NFR type they identified. Table 3 presents their findings, common

lithology of the reservoirs, detailing matrix and fracture porosity and permeability, and ultimate oil recovery factors.

Table 3. Sun & Politt (2021) NFR classification by and their reservoir characteristics

NFR type	**Lithology**	**Matrix properties**	**Fracture properties**	**Ultimate Oil Recovery factor**
Type 1 – tight matrix: fractures and solution-enhanced fracture porosity provide both storage capacity and fluid-flow pathways.	Basement, dolomite, limestone	Negligible matrix porosity and permeability	Porosity: 0.8 – 5.8% (avg 3.2%); Well test permeability: - avg: 184 mD - max: 3700 mD	13–55% (avg 31%)
Type 2 – macroporous (>20 μm pore size) matrix provides the primary storage capacity while fractures and solution-enhanced fracture porosity provide essential fluid-flow pathways.	Limestone, dolomite, sandstone, volcanics	Porosity: 4–20% (avg 11%); Air permeability: - avg: 5 mD - max: 100 mD	Porosity: 0.1–1.5% (avg 0.95%); Well test permeability: - avg: 103 mD - max: 3280 mD	7–65% (avg 35%)
Type 3 – microporous (<20 μm pore size) matrix provides all storage capacity while fractures only provide essential fluid-flow pathways.	Chalk, chalky limestone, diatomite, chert, siltstone	Porosity: 5–34% (avg 20%); Air permeability: - avg: 2 mD - max: 5 mD	Porosity: 0.1–2% (avg 0.9%); Well test permeability: - avg: 62 mD - max: 1800 mD	8–57% (avg 30%)

2.2 Fracture Properties and Characterization Methods

It is essential to characterize fractures in NFRs in order to estimate their impact on fluid flow and reservoir performance. Their characteristics, such as aperture, length, height, and connectivity, determine the extent to which hydrocarbons can be extracted efficiently. However, fractures vary significantly in size and orientation, making their quantification complex. A combination of direct and indirect measurement techniques, including borehole imaging, core analysis, seismic interpretation, and well testing analysis is required to assess their impact on reservoir behavior (Nelson, 2001). This section explores the fundamental properties of fractures and the methods used to characterize them in the subsurface.

A fracture can be characterized by its aperture, size, geometry, and orientation. It can be also characterized via shapes of matrix blocks as well as their density.

2.2.1 Fracture Aperture

Fracture aperture, also referred to as fracture width or opening, is defined as the distance between fracture walls. Typical fracture aperture values range from 10 to 200 μm (van Golf-Racht, 1982). Fracture apertures may be open or closed with mineral precipitation. Typically, fracture walls are never smooth, giving rise to fracture walls of irregular shape; however, for modelling convenience, fractures are treated as planar surfaces with aperture (width), w, transecting the bulk rock matrix.

The importance of estimating fracture aperture is that it directly relates to fracture permeability. To derive the relationship between aperture and permeability, Snow (1969) and Aguilera (1980) formulated the equation for a parallel plate model (also known as cubic flow equation) by integrating Darcy's law with viscous flow dynamics:

$$q = \frac{w^3 h}{12\mu L}\Delta p \tag{2.1}$$

By comparing cubic flow equation with Darcy's law (where cross-sectional flow area is $A = wh$):

$$k = \frac{w^2}{12} \tag{2.2}$$

This formula allows to estimate permeability of a fracture based on average value of aperture. For instance, if average value of an aperture is 10 μm, then permeability of this fracture is approximately 8,400 mD.

2.2.2 Fracture Size and Geometry

Though fractures have apertures in scale of a few microns, their length or height can be detected on various ranges of scales: from micrometers up to several kilometers (Narr, Schechter, & Thompson, 2006). Fracture height is a vertical extent of a fracture perpendicular to the bedding plane, while fracture length is a horizontal one parallel to the bedding plane. Thus, fracture height controls vertical communication across stratigraphic layers, whereas fracture length controls lateral drainage area as well as inter-well connectivity.

Typically, fractures have elliptical shape due to the way stress is distributed in the rock. Since tensile fractures propagate perpendicular to the least principle stress, the highest stress concentration at the crack tips cause fractures to be longer in one direction and shorter in another, thus forming elliptical shape. However, to make calculations more manageable, fracture shape is approximated to rectangular.

It is also relevant to mention that the distribution of the fracture length, density, connectivity, and geometry are scale dependent (Odling, 1997).

The study by Bonnet, et al. (2001) analyzed various 1D datasets containing trace lengths of fractures that intersect scanlines and revealed that the number and lengths of fractures recorded obey a power-law distribution. This finding is consistent with the study conducted by Odling (1997), who studied joint systems in sandstones at western Norway. Odling (1997) found that the fracture trace lengths also appear to follow a power-law distribution with an exponent of -2.1, which can be seen on Figure 3. An additional observation from Figure 3 is that power-law distribution is effective for various scales of fracture lengths – from several centimeters up to several kilometers. According to Bonnet, et al. (2001), the more heterogeneous is the fractured reservoir, the stronger is the relationship. However, the understanding of the reason behind it is still unclear.

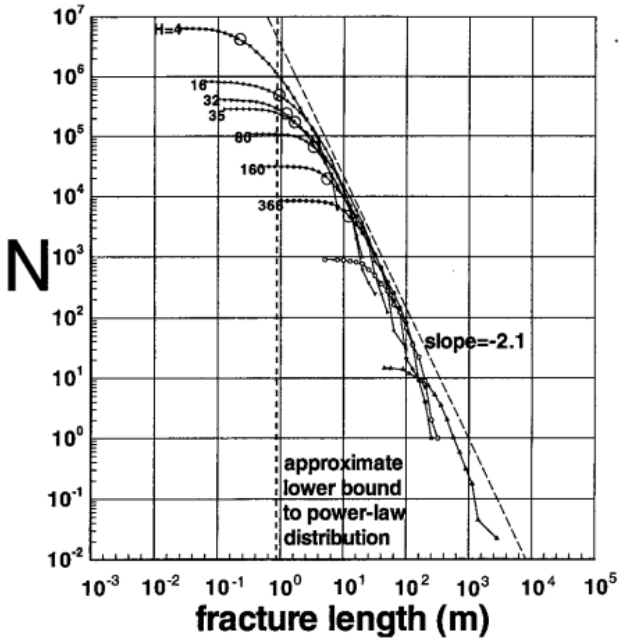

Figure 3. Number of fractures against trace fracture lengths combined from different maps. Fractures from all maps and different scales follow a power-law distribution with an exponent of -2.1 *(Odling, Scaling and connectivity of joint systems in sandstones from western Norway, 1997)*

Vermilye & Scholz (1995) studied the relationship between vein length and maximum aperture observed from seven different outcrops and in total collected data on 664 fractures. According to the results, there is a proportional linear relationship between fracture length and its aperture as evidenced by Figure 4. The importance of the outcomes of these studies is that it is key for development of correlations for fracture geometries.

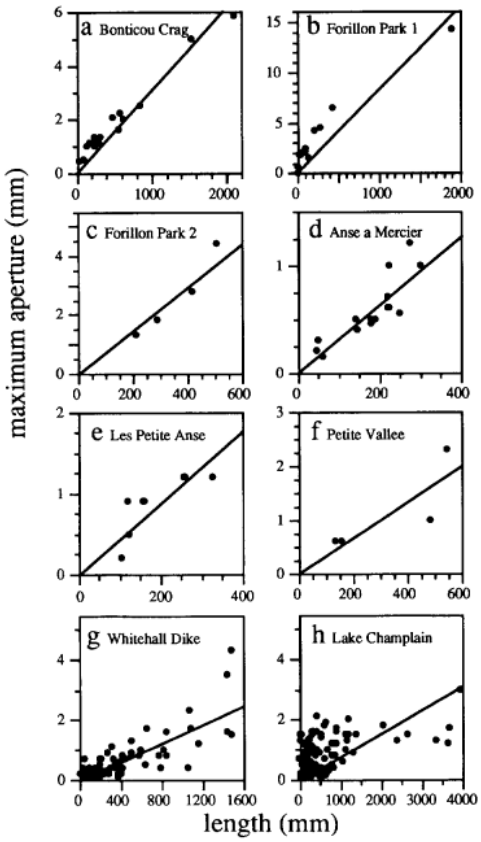

Figure 4. Maximum aperture vs length of fracture measurements from various locations *(Vermilye & Scholz, 1995)*.

2.2.3 Fracture Orientation

It is significant to account for fracture orientations as they determine the main axes of anisotropy, which identifies the preferred and restricted fluid flow directions. Understanding the main axes of anisotropy aids in well placement and production optimization strategies.

Naturally, fracture orientations align with the dominant stress fields that existed at the time of their formation, thus creating fracture clusters in the directions of the principle stresses. These patterns are influenced by the local and regional tectonic stress regimes, as well as mechanical properties of the rock, and the mode of fracture propagation (Mode I, II, and III – tensile, shear, and tearing) (Narr, Schechter, & Thompson, 2006). It is also important to note that fracture orientations are not scale-dependent, unlike other fracture properties mentioned in this chapter (Odling, 1997).

Fracture orientations are quantified by dip angle and strike azimuth. The dip angle is the degree of vertical inclination of a planar surface, while strike azimuth is its horizontal orientation relative to

a reference direction, typically north, as demonstrated by Figure 5. These measurements can be plotted on Stereonet diagrams to visually analyze the full orientation of fractures. Conversely Rose diagrams use strike azimuth data to illustrate the frequency and directional trends of fracture sets, as can be seen in Figure 6. However, neither diagram provides information about the spatial distribution of fractures in the field.

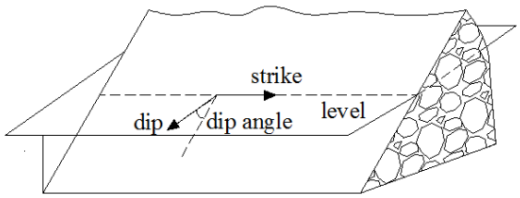

Figure 5. Illustration of fracture plane orientations *(Han, Wang, Jiao, Wang, & Wang, 2020)*

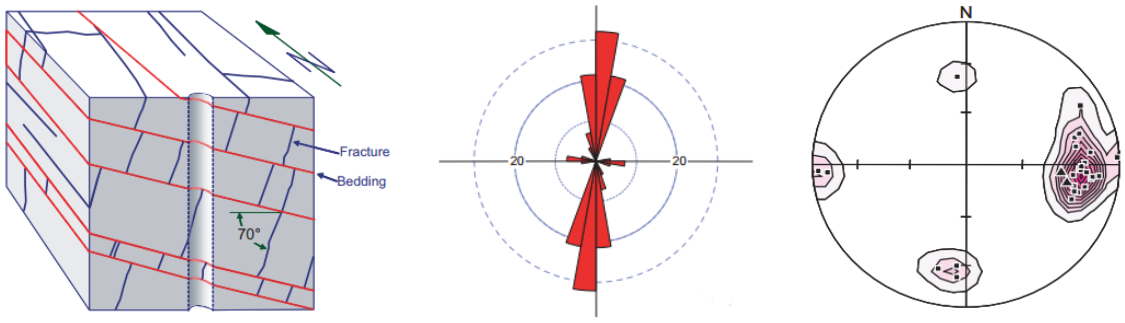

Figure 6. (a) Illustration of a fractured rock matrix block with fracture orientations displayed on (b) rose diagram and (c) stereonet *(Narr, Schechter, & Thompson, 2006)*.

To account for spatial distribution of fractures along a well, tadpole plots are usually used. In general, tadpole plots are visual representation of dipmeter log data, where a tadpole's head indicates depth and dip magnitude, whereas tail indicates its dip direction with upward direction typically pointing to north (Narr, Schechter, & Thompson, 2006). These plots are used to display both bedding and fracture orientations and can be distinguished by various symbols or colors, as can be seen in Figure 7 below.

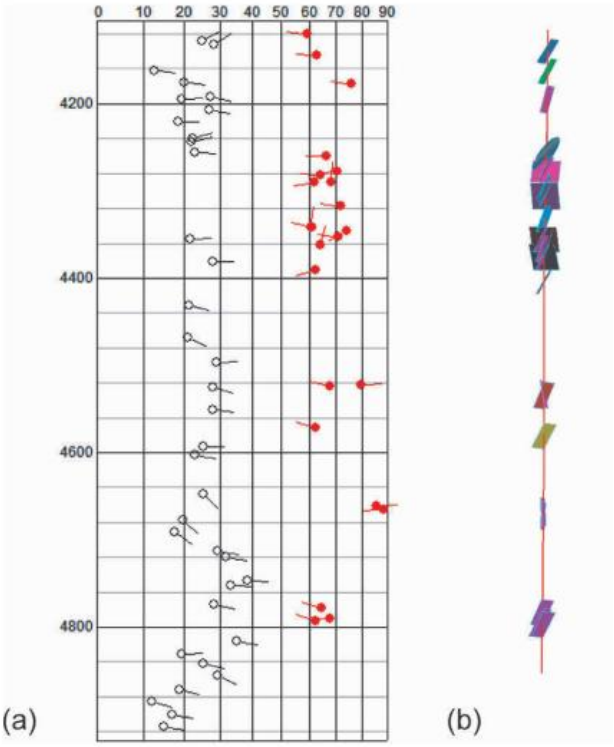

Figure 7. (a) Tadpole plot displaying bedding (white) and fracture (red) orientations; the x-axis represents dip angle, the y-axis represents depth; (b) 3D visualization of fracture orientations along wellbore *(Narr, Schechter, & Thompson, 2006)*.

2.2.4 Fracture Intensity and Connectivity

Besides defining fracture size, geometry, and orientation, it is crucial to account for fracture intensity and connectivity, in order to understand how fluid movement will be affected by the presence of fractures as well as to identify effective well placement and production strategy. While fracture intensity quantifies the abundance of fractures in a rock matrix, fracture connectivity describes how individual fractures are linked together to form a fracture network. The high fracture intensity itself is not a guarantee of an effective fluid movement, since isolated fractures may contribute little to reservoir permeability despite their abundance.

Fracture intensity is a measure of the number of fractures per unit length, area or volume of rock. It is important to distinguish this from the related but not synonymous term “fracture spacing”, as it is defined as an average distance between fractures along 1D line (such as borehole or scanline) (Dershowitz & Herda, 1992). Table 4 summarizes classification of fracture intensity based on

dimensions of the measurements and fractures proposed by Dershowitz & Herda (1992). According to their study, they concluded that although P_{11} and P_{22} are both useful in deriving 3D fracture intensity measurements, P_{22} is generally preffered as it is more reliable. The other types of fracture intensity measures are not recommended due to problematic interpretation and simulation.

Table 4. Measures of Fracture Intensity *(Dershowitz & Herda, 1992)*

Dimensions of Measurement Region / **Dimensions of Fracture Measure**	**1D (line): Borehole or Scanline**	**2D (area): Traceplane**	**3D (volume): Rock Mass**
1: Number of fractures	P_{11}: Number of fractures per unit length [L^{-1}]	P_{21}: Number of fractures per unit area [L^{-2}]	P_{31}: Number of fractures per unit volume [L^{-3}]
2: Dimension one less than that of measurement region		P_{22}: Length of fracture traces per unit area of trace plane [L^{-1}]	P_{32}: Area of fractures per unit rock volume [L^{-1}]
3: Dimension equal to that of measurement region			P_{33}: Volume of fractures per unit volume of rock [-]

It is also important to understand what geological and mechanical factors influence its magnitude in the subsurface. Table 5 summarizes the key controlling factors and their mechanisms.

Table 5. Factors affecting fracture intensity and their description.

Controlling factor	**Description / Mechanism**
Lithology	Lithology of a rock controls its ductility. Formations containing rocks with low ductility (such as dolomite, quartz, and feldspar) will have higher fracture intensity.
Porosity	The fracture intensity is higher for low porosity rocks.
Bed thickness	Emprically, it was observed that fracture intensity is higher for thin beds.
Structure curvature	High fracture intensity is observed for highly curved structures (e.g. folds) due to high magnitude of stress experienced by the formation.
Proximity to faults	High fracture intensity is observed near faults due to high stress concentrations.

Fracture connectivity is defined as the degree of linkage of individual fractures with each other to form continuous networks across reservoir. The connection between sufficient amount of fractures may significantly enhance fluid flow by creating pathways for fluid transmission.

The extent of fracture connection relies on the above-mentioned fracture properties, including fracture size, aperture, orientation, intensity, and spatial correlation among fractures (Berkowitz, Bour, Davy, & Odling, 2000). In fact, field observations made by Odling (1999) suggest that joint systems have higher fracture connectivity due to high fracture intensity and multiple fracture orientation sets; conversely, fault systems are poorly connected due to less fracture intensity and more uniform fracture orientations. Furthermore, Berkowitz (2000) investigated that the presence of fractures of various sizes in joint systems contributes to their high connectivity—with large fractures controlling connectivity at large scales, and smaller fractures enhancing local-scale connectivity. In fault systems, however, connectivity tends to emerge only at large scales, as small-scale fractures are often absent or insufficiently developed. It is also important to note that fracture

aperture also matters – even a highly connected system will fail to transmit fluids—and may actually impede movement—if the apertures are sealed or negligibly small.

It is also important to study fracture termination patterns to tie it with fracture connectivity. In cores and outcrops, one can observe that fractures may propagate, terminate or step-over the bed boundary. Study by Cooke & Underwood (2001) combined observations from different studies and concluded that fractures tend to propagate through strongly welded or well cemented bedding contacts. Conversely, for bedding contacts with weak cementation, fractures tend to terminate at these bedding boundaries. However, in practice, it is common to account neither strong nor weak bed contacts, which are classified as moderate-strength interfaces by the authors. Fractures accounting these moderate-strength interfaces tend to step-over (or jog) to the right or left, which depends on the distribution of flaws in the zones of tensile stress concentration.

Numerous studies attempted to quantify fracture connectivity, and their approached included analyzing different topology styles, counting fracture intersections from borehole images, studying fracture cluster interconnections on 2D maps and using seismic attenuations (Ozkaya & Mattner, 2003; Rubino, Guarracino, Muller, & Holliger, 2013; Ghosh & Mitra, 2009; Sanderson & Nixon, 2018; Odling, et al., 1999). The key takeaway from these different approaches is that scientists recognize the existence of a percolation threshold, a sufficient number of intersected fractures that creates an efficient network, which is sensitive to both geometric and topological properties.

2.2.5 Fracture Characterization Methods

While fracture properties such as aperture, orientation, and intensity are critical to reservoir performance, their measurement is often limited by data availability and resolution. As a result, fracture characterization relies on a combination of direct observations and indirect interpretations. This section introduces the principal methods used in industry and research to identify and quantify fracture systems in NFRs.

The direct methods of detecting fractures implies visually observing fractures, such as from core sample (Figure 8), borehole image logs (Figure 9), or using outcrop analogs of reservoirs. Fracture detection from core analysis implies visual inspection of cores for fractures from which information about fracture size, geometry, filling, aperture, and orientations can be logged.

Moreover, by conducting laboratory tests, it is possible to retrieve information about fracture permeability and rock strength. This method is limited to high costs, technical difficulties to retrieve cores from highly fractured zones and small scale observations.

On the other hand, borehole image logs (such as Formation Microimager, FMI) cover bigger scale by allowing to map fractures around the borehole wall, from which information about fracture locations, orientations, intensity, aperture, as well as filling can be retireved. However, the quality of these measurements depends on the quality of the logging, borehole quality, as well as depth of investigation and vertical resolution of the logging tool itself. Moreover, the deeper insight on fracture spacing is obtained from horizontal and deviated wells, vertical wells provide little information on fracture spacing. Additionally, it is impossible to assess fracture connectivity between wells with the use of image logs alone.

Outcrop analogs provide an invaluable insight into fracture properties, including fracture geometry, size, aperture, intensity, connectivity, and spatial orientation across scales ranging from milimeters up to hundreds of meters, which cannot be captured with well logs and core samples. The fracture data gathered from outcrop analogs is useful in forming the understanding of fracture network, recognizing patterns and relationships, which is helpful in constructing realistic reservoir models. This method is cost-effective and allows the collection of large datasets, from which further statistical information can be extracted. However, the suitability of an outcrop as an analog must be thorougly evaluated and any differences from the reservoir must be taken into account. Moreover, any fracture measurements taken from an outcrop must be used with caution, as weathering effects may affect the gathered data.

Figure 8. Examples of fractured core samples *(Warrlich, et al., 2010)*

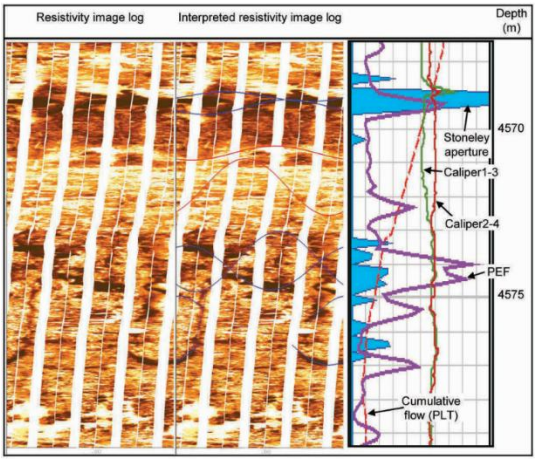

Figure 9. Example of interpreted borehole image log (right) and other well logs (left) in the fractured zone (Courtesy of TengizChevroil)

In contrast, indirect methods allow to detect fractures based on analysing their impact on rock or fluid behavior. Conventional well logs evaluation allows to identify fracture presence from the combination of observations from caliper, resistivity, and acoustic logs. Nevertheless, this method does not allow to quantify any fracture properties, but rather to confirm fracture presence itself; besides, this method is not highly reliable as interpretation of anomalous log responses is non-unique and can be even misleading.

Another indirect method of fracture detection is possible with the help of seismic data. The attenuation and velocity of seismic waves allow to detect fracture locations and their trends on a continuously large scale. It is possible to spot field-scale fracture networks and major faults. However, this method requires high resolution and thorough interpretation, and smaller fractures are not typically captured.

Analyzing well testing results is another indirect method of detecting fracture presence, as well as understand matrix-fracture interaction at scales ranging from tens to thousands of meters. During well testing 2 main data types are gathered – pressure and flow rate change over time. Pressure Transient Analysis (PTA) involves analyzing pressure data from drawdown or buildup tests on semilog and log-log scales. A typical pressure response for drawdown test in NFR is illustrated in Figure 10. On a semilog plot, the pressure response usually appears to have two parallel half-slope lines, whereas on log-log scale, the pressure derivative curve shows a characteristic "dip", also known as "V-shape" or "U-shape".

Therefore, PTA allows to diagnose fracture presence, detect flow regimes, and compute fracture properties, such as porosity, permeability, storativity, and matrix-fracture transfer coefficients. By using PTA, it is also possible to detect interwell connectivity (interference well testing) and detect boundaries (conductive or sealed faults). However, this method requires to shut-in wells for buildup tests and high quality pressure data is a must. In low permeability reservoirs, longer test durations are necessary, increasing costs. Moreover, though PTA allows to compute fracture data, its results may be non-unique, as different fracture property combinations may produce similar pressure response.

Rate Transient Analysis (RTA) is considered to be an extension of PTA and utilizes both pressure and flow rate data. Unlike PTA, RTA usually deals with longer periods of time and does not require any production interventions. By having sufficient production history, RTA can capture long-term fracture behavior and half-slope linear flow regime, as depicted in Figure 11. Additionally, RTA allows to estimate effective fracture permeability. However, like PTA, RTA results may be non-unique, as different combinations of fracture properties may yield similar production declines.

Typically, it is recommended to use combinations of PTA and RTA in order to make reliable fracture properties computations, since neither of these methods is reliable on its own.

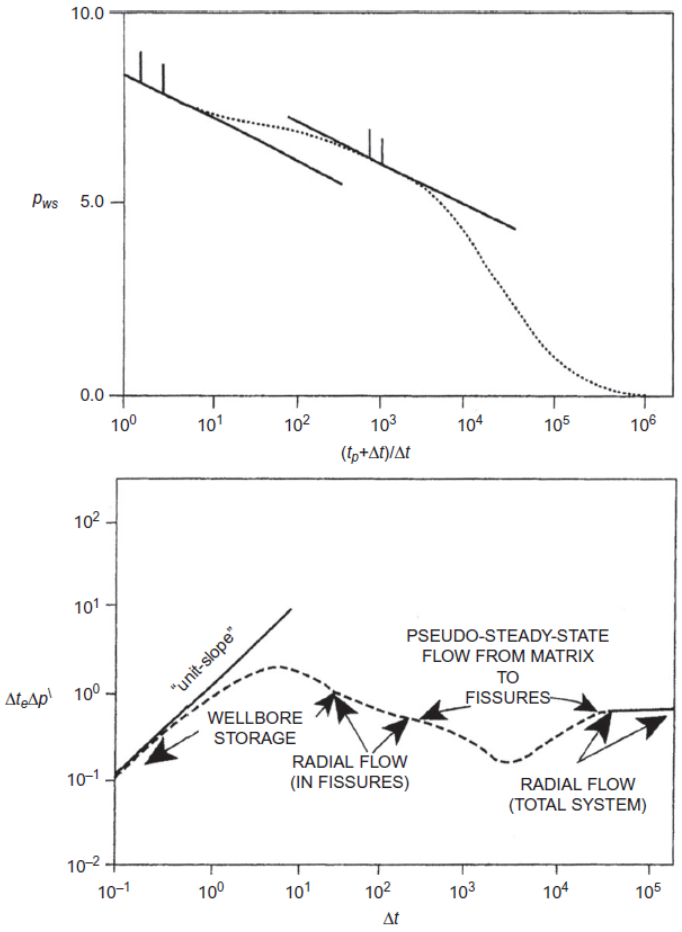

Figure 10.Typical drawdown test response for dual porosity system appears as two parallel half-slope straight lines on semi log plot (up) and V-shaped "dip" on log-log plot (down) *(Ahmed, 2019)*

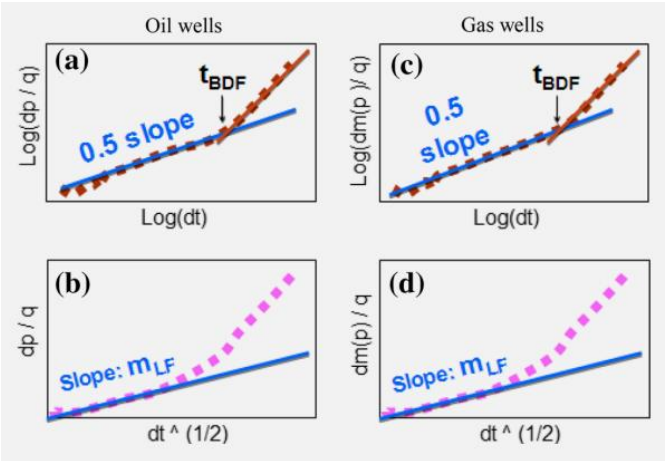

Figure 11. Example of RTA for dual-porosity system on oil (left) and gas (right) wells with half-slope line representing fracture behavior *(Bahrami, Pena, & Lusted, 2016)*

2.3 Physical properties of Fracture and Matrix and their Relationship

2.3.1 Definition of Dual Porosity System

Before examining existing NFR models, it is essential to define the physical properties that serve as their foundation. Reservoir performance in NFRs is highly dependent not only on fracture properties defined in the previous subchapter, but also on matrix properties and interaction between them.

Fractured reservoir rocks exhibit high heterogeneity because fluids are stored and transmitted through two distinct systems – matrix and fracture.

Matrix porosity Φ_m, is defined as a fraction of the interconnected void space between rock grains and typically forms during sediment deposition and, thus, preserves the rock's original characteristics. This type of porosity often correlates with permeability, as it is influenced by the size, shape, and spatial distribution of the grains (Ahmed, 2019). Additionally, matrix porosity may also incorporate secondary porosity, also known as induced porosity, a fraction of void space formed during diagenesis after sediment deposition.

Fracture porosity Φ_f provides an additional storage pathway through fracture systems, which can dominate fluid flow regime despite its small volumetric contribution.

In dual porosity reservoirs, the total porosity Φ_t of the system is defined as the sum of matrix and fracture porosities and corresponds to the static definition of rock storage. Empirically, it was proved that the fracture porosity is much less than the matrix porosity (van Golf-Racht, 1982).

The typical values for fracture porosity defined by van Golf-Racht (1982) are:

1. Macrofracture network (fracture aperture > 100 μm): $\Phi_f = 0.01 – 0.5\%$
2. Isolated fissures (or microfractures with aperture < 100 μm): $\Phi_f = 0.001 – 0.01\%$
3. Fissure network: $\Phi_f = 0.01 – 2\%$
4. Vugs (in Karstic rock): $\Phi_f = 0.1 – 3\%$

Moreover, as a rule of thumb, fracture porosity can be estimated from total porosity using the following empirically established relationship (van Golf-Racht, 1982):

1. If $\Phi_t < 10\%$, then $\Phi_{fmax} < 0.1\Phi_t$
2. If $\Phi_t > 10\%$, then $\Phi_{fmax} < 0.04\Phi_t$

As evident from these fracture porosity ranges, fractures typically have a minimal impact on overall rock storage. However, when total rock porosity is low ($\Phi_t < 5\%$) and transient flow dynamics are considered, an accurate estimation of fracture porosity becomes essential (van Golf-Racht, 1982).

Nelson (2001) presented another way to estimate fracture porosity. He claims that the fracture porosity for a set of parallel fractures is a function of fracture aperture and spacing, which can be computed by the following equation:

$$\phi_f = \left(\frac{w}{D+w}\right) * 100 \tag{2.3}$$

Where,

w – average effective fracture aperture (width), [cm]

D – average fracture spacing between parallel fractures, [cm]

The plot below can present the following relationship:

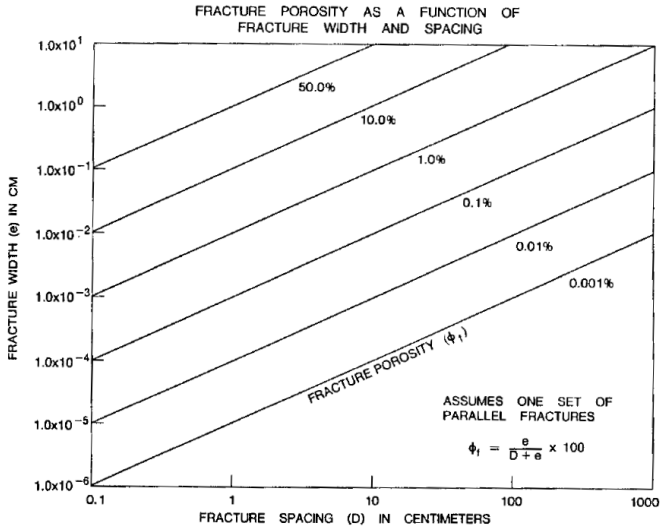

Figure 12. Fracture porosity as a function of fracture (width) aperture and fracture spacing *(Nelson, 2001)*

2.3.2 Fracture and Matrix Permeability

Permeability is another important parameter, as it quantifies the ability rock to transmit a fluid. Earlier, permeability of a single fracture was defined using parallel plate model and cubic flow equation to be:

$$k_f = \frac{w^2}{12} \tag{2.2}$$

This formula can be slightly modified to account for the average fracture spacing D between parallel plates, thus (Huitt, 1956; Snow, 1968; Sharp, Maini, & Brekke, 1972):

$$k_f = \frac{w^3}{12D} \tag{2.4}$$

It should be noted that these equations are valid for single phase, Newtonian laminar flow.

Parsons (1966) proposed total permeability of the system, accounting for both matrix and fracture permeabilities of different fracture sets:

$$k_{fm} = k_m + \frac{e_1^3 \cos^2 \alpha_1}{12D_1} + \cdots + \frac{e_n^3 \cos^2 \alpha_n}{12D_n} \tag{2.5}$$

Where,

k_{fm} – total permeability (fracture + matrix)

k_m – matrix permeability

α – angle between the axis of the pressure gradient and fracture planes

n – number of fracture sets.

This equation assumes that flow across the fracture-matrix surface does not significantly alter the flow within either system. However, this assumption holds primarily in cases where matrix permeability is either very high or negligible, as crossflow effects become insignificant under these conditions. This equation proposed by Parsons (1966) aligned with the empirically derived fracture

permeability by Witherspoon & Gale (1977) and is a good approximation at the exploration stage of a field. The equations accounting for crossflow were proposed by Barenblatt, Zheltov, & Kochina (1960) and Duguid (1973), however they are not typically used due to their complexity.

Nelson (2001) demonstrated alternative approach of fracture permeability estimation, by using its relationship with fracture aperture and spacing:

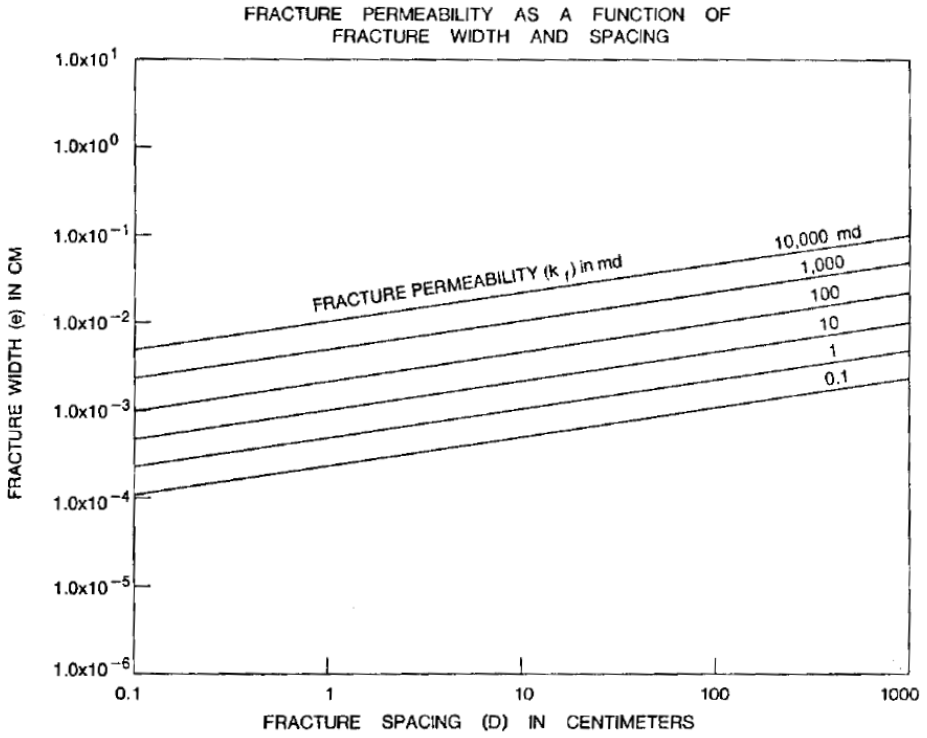

Figure 13. Fracture permeability as a function of fracture (width) aperture and fracture spacing (Nelson, 2001)

Van Golf-Racht (1982) estimated fracture porosity and permeability based on the geometric model used to approximate NFRs. Reiss (1976) proposed three such models—slides, matches, and cubes (Figure 14)—to represent different fracture distributions. The selection of an appropriate model depends on the relative densities of horizontal and vertical fractures. For instance, if these densities are equal, then the cube model is the most suitable representation of the system; in contrast, if either horizontal or vertical fracture density dominates, then either slides or match model can be applied. Using these frameworks, van Golf-Racht (1982) derived equations for computing areal fracture density (A_{fD}), fracture porosity (Φ_f), and fracture permeability (k_f) as functions of either porosity block dimension (a) or fracture aperture (b).

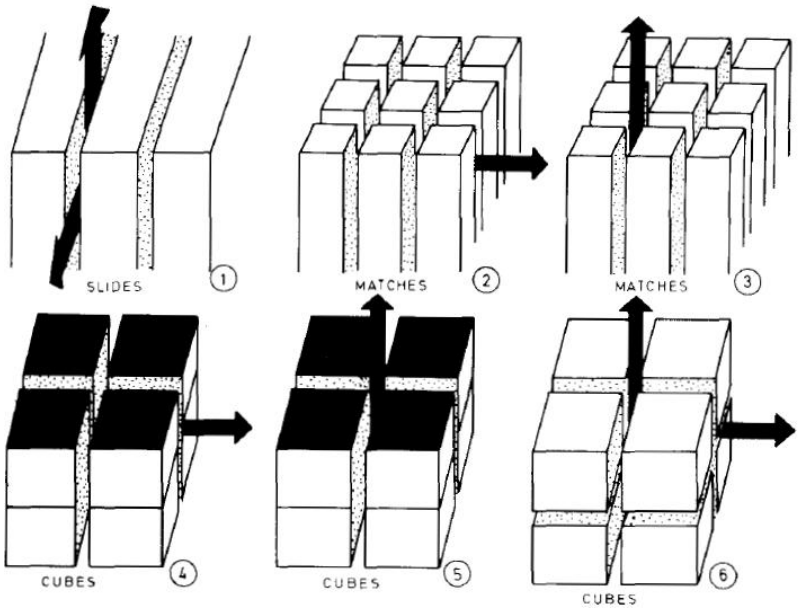

Figure 14. Simplified geometrical approximations of NFRs by Reiss (1976)

Table 6. Summary of equations used to compute fracture density, porosity, and permeability, based on different simplified geometrical NFR models *(van Golf-Racht, 1982)*

MODEL		DIMENSIONLESS EQUATIONS				DIMENSIONAL EQUATIONS			
Nº	TYPE	A_{fD}	ϕ_f	$k_f(\phi_f,a)$	$k_f(\phi_f,b)$	A_{fD} cm^{-1}	ϕ_f %	$k_f(\phi_f,a)$ darcy	$k_f(\phi_f,b)$ darcy
1	SLIDES	$\frac{1}{a}$	$\frac{b}{a}$	$\frac{1}{12}a^2\phi_f^3$	$\frac{1}{12}b^2\phi_f$	$\frac{1}{a}$	$\frac{1}{100}\frac{b}{a}$	$8{,}33\,a^2\phi_f^3$	$8{,}33\times10^{-4}b^2\phi_f$
2	MATCHES	$\frac{1}{a}$	$\frac{2b}{a}$	$\frac{1}{96}a^2\phi_f^3$	$\frac{1}{24}b^2\phi_f$	$\frac{1}{a}$	$\frac{1}{100}\frac{2b}{a}$	$1{,}04\,a^2\phi_f^3$	$4{,}16\times10^{-4}b^2\phi_f$
3	MATCHES	$\frac{2}{a}$	$\frac{2b}{a}$	$\frac{1}{48}a^2\phi_f^3$	$\frac{1}{12}b^2\phi_f$	$\frac{2}{a}$	$\frac{1}{100}\frac{2b}{a}$	$2{,}08\,a^2\phi_f^3$	$8{,}33\times10^{-4}b^2\phi_f$
4	CUBES	$\frac{1}{a}$	$\frac{2b}{a}$	$\frac{1}{96}a^2\phi_f^3$	$\frac{1}{12}b^2\phi_f$	$\frac{1}{a}$	$\frac{1}{100}\frac{2b}{a}$	$1{,}04\,a^2\phi_f^3$	$4{,}16\times10^{-4}b^2\phi_f$
5	CUBES	$\frac{2}{a}$	$\frac{2b}{a}$	$\frac{1}{48}a^2\phi_f^3$	$\frac{1}{12}b^2\phi_f$	$\frac{2}{a}$	$\frac{1}{100}\frac{2b}{a}$	$2{,}08\,a^2\phi_f^3$	$8{,}33\times10^{-4}b^2\phi_f$
6	CUBES	$\frac{2}{a}$	$\frac{3b}{a}$	$\frac{1}{162}a^2\phi_f^3$	$\frac{1}{18}b^2\phi_f$	$\frac{2}{a}$	$\frac{1}{100}\frac{3b}{a}$	$0{,}62\,a^2\phi_f^3$	$5{,}55\times10^{-4}b^2\phi_f$

UNITS : K (Darcy), a (cm); b (microns); ϕ_f (percent units)

Meanwhile, the relationship between matrix permeability and porosity is mostly empirical and cannot be represented by a single equation. This is because both these properties develop during sediment deposition and subsequent diagenesis, and their correlation is a function of lithology of the reservoir rock. As shown in the figure below, this relationship appears linear on a semilog scale and for each lithology, it has its own slope and intercept.

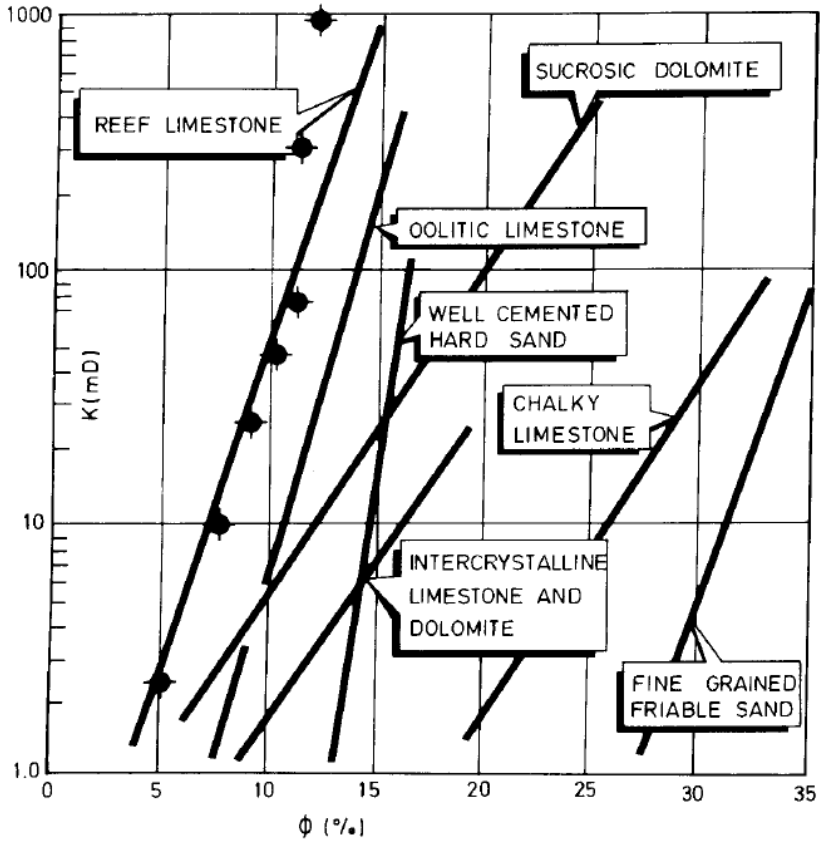

Figure 15. Relationship between matrix permeability and porosity as a function of lithology *(van Golf-Racht, 1982)*

Therefore, in general, the relationship between matrix permeability and porosity can be expressed with the following generalized equation (van Golf-Racht, 1982):

$$\log k_m = a\Phi_m + b \tag{2.6}$$

2.4 Existing NFR models

2.4.1 Origins of Dual Porosity Model

Modelling fluid behavior in NFRs has been a challenging task and a subject of significant research interest since the 1960s. The first dual porosity model was first introduced by Barenblatt et al. (1960), who proposed treating fractures and matrix as separate continua. This approach addressed the limitations of single porosity models, which could not capture the dynamics of fractured reservoirs.

Barenblatt et al. (1960) defined fractures to have low storage capacity (low porosity), but high permeability, while matrix to have high storage capacity, but low permeability. The fluid exchange between the two systems was driven by the pressure difference between matrix p_m and fracture p_f, governed by a transfer term:

$$v = \frac{\alpha}{\mu}\left(p_m - p_f\right) \tag{2.7}$$

where,

v – volume of fluid transferred from matrix to pressure per unit time and rock volume,

α – dimensionless geometrical parameter of fractured rock,

μ – fluid viscosity

$(p_m - p_f)$ – pressure difference between matrix and fractures.

The authors derived two coupled governing equations for the dual-porosity system:

1. Fracture system (high permeability, pseudo-steady state flow):

$$k_f \Delta p_f + \alpha\left(p_m - p_f\right) = 0 \tag{2.8}$$

2. Matrix system (low permeability, transient flow):

$$\left(c_m + \phi_m c_{fl}\right)\frac{\partial p_m}{\partial t} + \frac{\alpha}{\mu}\left(p_m - p_f\right) = 0 \tag{2.9}$$

where,

k_f – fracture permeability,

c_m – matrix compressibility,

Φ_m – matrix porosity,

c_{fl} – fluid compressibility.

By combining these equations, Barenblatt et al. (1960) obtained a single equation for fracture pressure p_f:

$$\frac{\partial p_f}{\partial t} - \eta\frac{\partial \Delta p_f}{\partial t} = \kappa \Delta p_f \tag{2.10}$$

where,

κ – the coefficient of piezo-conductivity and equals to $\kappa = \frac{k_f}{\mu(c_m + \phi_m c_{fl})}$,

η – the dimensionless parameter characterizing fissured rocks and equals to $\eta = \frac{k_f}{\alpha}$.

The dimensionless parameter η decreases with the finer matrix blocks and denser fracturing. This parameter is an important one, as it is scaling the dispersion term $\eta\frac{\partial \Delta p_f}{\partial t}$ that represents time lag in pressure equilibration between matrix and fracture. This time lag arises because fluid transfer depends on the slow flow in the matrix and rapid flow in the fractures. To sum up, the model introduced by Barenblatt et al. (1960) became foundational for subsequent NFR studies, as it proposed the concept of pressure discontinuities and transient lag effects.

2.4.2 Classical Dual Porosity Model

Following Barenblatt et al.'s (1960) foundational work, Warren & Root (1963) revolutionized dual porosity model by introducing well-known “Sugar Cube” model, where matrix blocks are idealized as identical homogeneous cubes separated by orthogonal fractures (Figure 16).

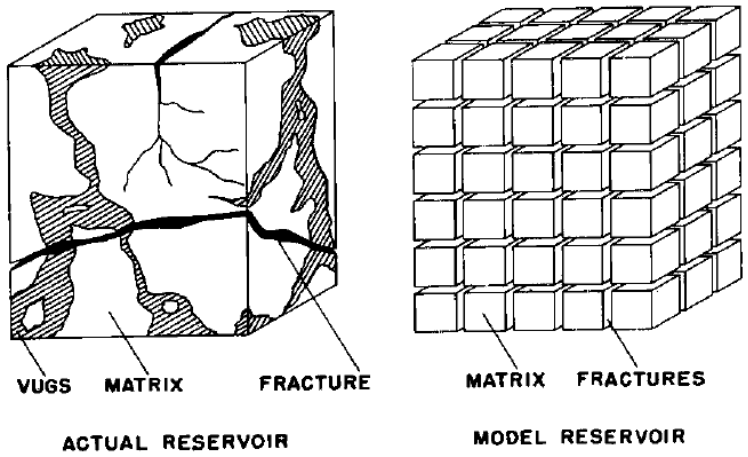

Figure 16. Idealization of the heterogeneous porous medium Warren & Root (1963)

The idea of treating matrix and fracture as separate continua is similar to Barenblatt et al.’s (1960) idea, where matrix has high storage, but low permeability, and fracture has low storage, but high permeability. The key parameters introduced by Warren & Root (1963) are:

1. Interporosity Flow Coefficient, λ – a parameter that quantifies the ease of fluid transfer from matrix to fracture, where small λ represents tight matrix with slow matrix-fracture transfer. It can be computed by the following formula:

$$\lambda = \frac{\sigma k_m r_w^2}{k_f}, \sigma = \frac{12}{L^2} \tag{2.11}$$

   where,

   σ – is a shape factor for cubic matrix blocks, and L is a size of matrix blocks.

2. Storativity Ratio, ω – a fraction of fracture contribution to the total rock storage, where smaller ω represents more matrix contribution compared to fracture. It can be computed as follows:

$$\omega = \frac{\phi_f c_f}{\phi_f c_f + \phi_m c_m} \tag{2.12}$$

The main governing equations introduced by the authors are:

1. Fracture system:

$$\frac{k_{fx}}{\mu}\frac{\partial^2 p_f}{dx^2} + \frac{k_{fy}}{\mu}\frac{\partial^2 p_f}{dy^2} - \phi_m c_m \frac{\partial p_m}{\partial t} = \phi_f c_f \frac{\partial p_f}{\partial t} \tag{2.13}$$

2. Matrix system:

$$\phi_m c_m \frac{\partial p_m}{\partial t} = \alpha \frac{k_m}{\mu}\left(p_f - p_m\right) \tag{2.14}$$

It should be noted that Warren & Root (1963) equations have PSS assumption, unlike Barenblatt, et al. (1960), who assume transient matrix flow. Thus, using PSS flow assumption simplifies calculations for well test analysis. The matrix-fracture fluid transfer term is:

$$\tau = \sigma \frac{k_m}{\mu}\left(p_m - p_f\right) \tag{2.15}$$

This transfer term accounts for matrix permeability, unlike Barenblatt, et al. (1960) who did not account for it.

The combined dimensionless solution for pressure drawdown/buildup behavior derived using Laplace transforms is:

$$p_{wf}(\tau) = \frac{1}{2}\left[\ln \tau + 0.80908 + Ei\left(-\frac{\lambda\tau}{\omega(1-\omega)}\right) - Ei\left(-\frac{\lambda\tau}{1-\omega}\right)\right] \tag{2.16}$$

This solution reveals that at early time, there is fracture dominated flow, that is controlled by ω, while at late-time, pressure drop is controlled by matrix-fracture interaction that is governed by λ.

The solution proposed by Warren & Root is an industry standard for analyzing dual porosity systems, as it is possible to estimate ω and λ by PTA. In Figure 17, the authors generated theoretical buildup curves from which two parallel half-slope straight lines can be observed on a semilog

scale. The first slope is used to estimate fracture storage ω, while the second one reflects homogeneous reservoir behavior (ω + (1- ω)).

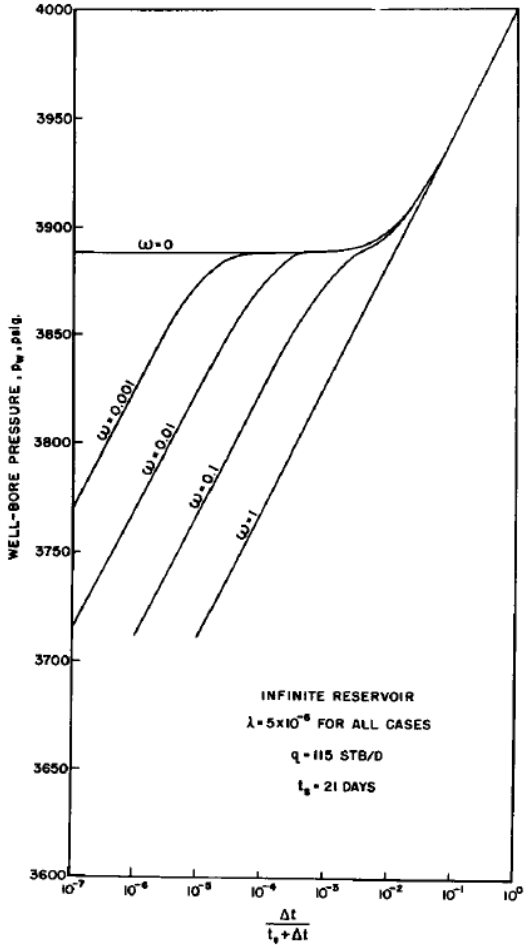

Figure 17. Theoretical Buildup curves generated by Warren & Root (1963)

Overall, despite the model developed by Warren & Root (1963) having a lot of simplifications and a main limitation of assuming a uniform dual system, it is still a good estimate of dual porosity systems, which bridged Barenblatt, et al. (1960) theory and practical well test analysis.

2.4.3 Further Evolution of Dual Porosity Model

The classical dual porosity model was further refined by Odeh (1965), Kazemi (1969), De Swaan (1976), Najurieta (1980), and Streltsova (1983). Odeh (1965) proposed his model based on his field observations where two parallel half-slope straight lines were not observed for naturally fractured reservoirs, but he rather observed response similar to homogeneous reservoirs. Odeh

(1965) simplified the "double porosity" model by assuming a homogeneously fractured reservoir where fractures and matrix are uniformly distributed. Unlike Warren & Root's geometric matrix-fracture system, Odeh's model does not require specific matrix block geometry, spacing, or anisotropy. This generalization allowed Odeh to derive equations functionally identical to those for homogeneous reservoirs, using two key parameters:

1. β – bulk volume fraction occupied by fractures.
2. $(c\Phi)_{av}$ – average porosity-compressibility product of the combined fracture-matrix system.

Thus, the final governing equation derived by Odeh (1965) is:

$$\Delta p = -\frac{q\mu}{4\pi k_f h\beta}\left[Ei\left(-\frac{r^2\mu(\beta\phi_f c_f + (1-\beta)\phi_m c_m)}{4k_f\beta t}\right)\right] \tag{2.17}$$

The application is quite similar to what proposed Warren & Root (1963) – by constructing pressure buildup curve on semilog scale and extrapolating the straight slope line (Figure 18), it is possible to compute $k_f h\beta$, which represents the effective flow capacity of the reservoir.

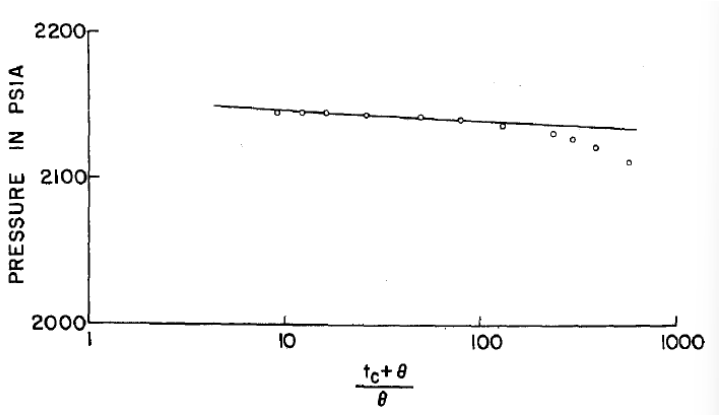

Figure 18. Pressure buildup curve and extrapolated straight line by Odeh (1965)

The further refinement was made by Kazemi (1969), as he challenged Warren & Root's (1963) model for assuming pseudo-steady state matrix flow and re-derived equations for full unsteady-state flow. The study by Kazemi (1969) arrived at the similar conclusions made by Warren & Root (1963), as he obtained buildup curves with two parallel half-slope straight lines and the validated parameter introduced by Warren & Root – interporosity flow coefficient, λ. Kazemi's interporosity flow coefficient is computed by:

$$\lambda = \frac{12 k_m r_w^2}{k_f h^2} \tag{2.18}$$

The main difference between their outcomes is that due to transient matrix flow, pressure drop at earlier time is higher compared to Warren & Root.

Later in 1976, De Swaan challenged the model proposed by Warren & Root, particularly empirical parameters such as fracture storativity, ω, interporosity flow coefficient, λ, and shape factor, σ, as these parameters lack direct physical ties to matrix dimensions or fracture properties. Thus, De Swaan (1976) eliminated these parameters and re-derived solutions using measurable properties:

1. $k_f h_f$ – permeability-thickness product for fractures
2. $\phi_m x_m$ – porosity-matrix block dimension product for matrix

The key governing equation proposed by De Swaan (1976) is:

$$\Delta p = \frac{q_w \mu}{4\pi h_f k_f} \ln\left(\frac{4\eta t}{1.78 r_w^2}\right) \tag{2.19}$$

This equation can be applied for both early time fracture dominated flow, as well as late time flow dominated by matrix-fracture fluid transfer. The parameter used to distinguish these types of flow is hydraulic diffusivity, η:

1. For early time fracture dominated flow, fracture hydraulic diffusivity is computed by:

$$\eta_f = \frac{k_f}{\phi_f \mu c} \tag{2.20}$$

2. For late time, during the matrix-fracture fluid transfer, the hydraulic diffusivity will depend on matrix block geometry:
   a. For slab shaped matrix blocks:

$$\eta_{sl} = \frac{1}{\frac{1}{\eta_f} + \frac{k_m h_m}{k_f h_f}\frac{1}{\eta_m}} \approx \frac{k_f h_f}{\mu c \phi_m h_m} \tag{2.21}$$

   b. For spherical matrix blocks:

$$\eta_{sp} = \frac{1}{\frac{1}{\eta_f} + \frac{2k_m}{3k_f h_f}\frac{1}{\eta_m}} \approx \frac{3k_f h_f}{2\mu c \phi_m h_m} \tag{2.22}$$

c. For composite reservoir with varying matrix block sizes and porosities:

$$\eta_{co} = \frac{1}{\frac{1}{\eta_f} + \frac{\mu c}{k_f h_f} x_m \phi_m} \tag{2.23}$$

The solution proposed by De Swaan (1976) is more practical, as it is possible to directly estimate $k_f h_f$ from the early-time slope and $\phi_m x_m$ from the late-time line's intercept. However, it should be noted that this model does not consider the transition zone.

Later in 1980, Najurieta modified model by De Swaan (1976), by focusing on transition interaction between fractures and matrix. He introduced 4 new parameters: fracture transmissivity, T_f, fracture storage, S_f, matrix storage, S_m, and time constant, τ, which is related to matrix block size. So, the approximate line-source solution of Najurieta's model is:

$$\Delta p_f = \frac{q_w B_o}{4\pi N T_f} Ei\left(-\frac{r^2}{4\eta_{co} t}\right) \tag{2.24}$$

where, η_{co} represents the dynamic interaction between fractures and matrix. This parameter can be computed for different fracture-matrix geometries:

1. For set of horizontal parallel fractures:

$$\eta_{co} = \frac{T_f}{S_f + S_m\sqrt{\frac{t}{\tau}}\tanh\sqrt{\frac{\tau}{t}}} \tag{2.25}$$

2. For set of cross-cutting 3D orthogonal fractures:

$$\eta_{co} = \frac{T_f}{S_f + S_m\left(\sqrt{\frac{t}{\tau}}\coth\sqrt{\frac{\tau}{t}} - \frac{t}{\tau}\right)} \tag{2.26}$$

The results of Najurieta's model match Kazemi's model, thus offering improved accuracy for PTA in fractured reservoirs.

Finally, Streltsova (1983) challenged Warren & Root model, by introducing spatial pressure gradients and matrix storage effects into the matrix-fracture fluid transfer term, addressing inconsistencies of pressure response with field observations. Specifically, Warren & Root's model predicted an S-shaped transitional pressure curve with an inflection point, whereas Streltsova observed a linear transitional segment in field data. Her gradient-flow model resolved this discrepancy by showing that there is a linear transitional pressure segment on a semilog plot that forms a straight line with half the slope, from which permeability can be estimated. The governing equations underpinning her model are:

1. Fracture Pressure:

$$\Delta\bar{p} = \frac{q}{2\pi T}\frac{1}{s}K_0\left\{\sqrt{\bar{s} + r_D\sqrt{\frac{\bar{s}\phi_m c_m}{\phi_f c_f}}\left(\frac{H}{h}\right)\tanh\frac{1}{r_D}\sqrt{\frac{\bar{s}\phi_m c_m}{\phi_f c_f}}}\right\} \tag{2.27}$$

2. Matrix Pressure:

$$\Delta\bar{p}_m = \Delta\bar{p}\frac{\tanh\left(H\sqrt{\frac{s}{\eta_m}}\right)}{H\sqrt{\frac{s}{\eta_m}}} \tag{2.28}$$

By incorporating spatial gradients and matrix storage, Streltsova's model improved the accuracy of permeability estimation and provided a framework for analyzing fractured reservoirs with limited test durations.

2.4.4 Rate Decline Analysis in NFRs

The Rate Transient Analysis (RTA) is an extension of Pressure Transient Analysis (PTA) and provides a robust reservoir evaluation method by interpreting flow rate and pressure data collected continuously over the production lifecycle for bottomhole constrained production, such as in unconventional reservoirs that are extensively fractured. Unlike PTA, RTA does not require well shut-in periods; instead, it uses the whole production data. Various transformations—such as converting data into material balance time or applying pseudopressure and pseudotime transformations for gas wells—can be used within RTA to recast data as an equivalent constant rate problem. Among the analytical techniques available, the Decline Curve Analysis (DCA)

method is most employed, especially in unconventional reservoirs (Hazlett, Farooq, & Babu, A complement to decline curve analysis, 2021). DCA involves fitting observed flow rates over time to exponential decline curves, determining parameters that characterize production decline, forecasting future performance, and estimating reservoir reserves.

The classical DCA model is introduced by Arps (1945) and modified later by Robertson (1988). The main concept is to curve fit flow rate data to a family of hyperbolic functions at early times to capture rapid decline, then transition to an exponential function for late-time behavior:

$$q(t) = \begin{cases} \dfrac{q_i}{(1 + BD_1 t)^{\frac{1}{B}}}, & t < D^* \\ q_i \exp(-D_2 t), & t \geq D^* \end{cases} \tag{2.29}$$

where,

q_i – initial rate,

D_1 and D_2 – Decline constants,

B – decline exponent, typically $0<B\leq1.0$, but often empirically > 1.0 (Ilk, Rushing, Perego, & Blasingame, 2008),

D* - transition time between hyperbolic and exponential decline.

The main disadvantage of this model is that these fitted parameters are not directly related to reservoir properties (Hazlett, Farooq, & Babu, A complement to decline curve analysis, 2021).

To address this, Ilk, et al. (2008) introduced "power law loss ratio" rate decline model:

$$D = D_\infty + D_1 t^{-(1-n)} \tag{2.30}$$

$$q(t) = q_i \exp\left(-D_\infty t - \frac{D_1 t^n}{n}\right) \tag{2.31}$$

where,

D_1 and D_∞ are decline constants at t=1 and $t\rightarrow\infty$, respectively, and

n is a time exponent.

This model adapts to transient, transition, and boundary-dominated flow regimes.

Valkó & Lee (2010) proposed Stretched Exponential Decline as the modification of Arps (1945) model:

$$q(t) = q_i \exp\left(-\frac{t}{\tau}\right)^n \tag{2.32}$$

where,

τ – characteristic time constant that controls decline speed,

n – stretching exponent, in range from 0 to 1.0.

This model accounts for varying flow regimes in fractured rock volumes and captures reservoir heterogeneity via the exponent *n*.

Duong (2011) introduced a model for fractured reservoirs experiencing long-term linear or bilinear flow:

$$q(t) = q_i t^{-m} \exp\left[\frac{a}{1-m}(t^{1-m} - 1)\right] \tag{2.33}$$

where,

a and *m* are intercept and power law slope, respectively.

All these models seek to better approximate the complexities observed in fractured reservoirs. Each model offers unique advantages depending on reservoir type, flow regime, and data availability. While classical DCA remains a practical tool for rapid forecasting, modern methods provide deeper insights into reservoir heterogeneity and fracture networks, enhancing reserve estimation accuracy.

3. METHODOLOGY

This research is based on theoretical and computational modeling approach aimed at enhancing the analytical understanding of fluid flow dynamics in NFRs. Initially, a conceptual model of the Representative Element Volume (REV) is defined, along with explicit assumptions necessary for simplifying the governing equations. Representative Element Volume is a unit cell, the smallest volume over which observations, analyses and measurements can be performed that will yield a value of representative of the whole (Hill, 1963). Subsequently, fundamental governing equations, accompanied by relevant initial and boundary conditions, are introduced. These equations are then analytically derived based on the predefined assumptions. After establishing the analytical formulations, the numerical implementation is carried out using the Python programming language, where the correctness and reliability of the implemented model are verified through comparisons with results of the study published by Hazlett, et al (2024). Lastly, a sensitivity analysis is conducted to systematically evaluate the influence of aspect ratio (a/b) and scaling factor (S) on the model outcomes, providing further validation and robustness to the developed analytical representative element model.

3.1 Model Development

3.1.1 Conceptual Model and Assumptions

The Representative Element Volume (REV) of this study is based on the model developed by Hazlett, et al. (2024) and consists of a 2D matrix block (dimensions 2a x 2b) fully penetrated with 2 parallel vertical fractures (aperture w, length 2b) as illustrated on Figure 19. The matrix is characterized by high storage capacity, but low permeability, k_x, while fractures offer high permeability, k_f, but low storage capacity.

Initially, both matrix and fracture are assumed to be fully saturated with a single-phase fluid. As depletion starts, fractures act as primary pathways for fluid flow, thus depleting rapidly due to high k_f, creating pressure sink at withdrawal points $(\pm a, -b)$. The fluid flow in matrix is symmetrical and perpendicular to fractures, thus creating linear flow from $x=0$ to $x=\pm a$.

Earlier, Hazlett, et al. (2024) modeled fracture depletion with time but assumed that due to the large contrast in process time scales for fluid flow, the boundary condition imposed on matrix depletion could ignore fracture temporal pressure change ($P_f = 0 \; for \; t > 0$), thus decoupling fracture and matrix flow. This simplification relies on a high k_f/k_x ratio ($\geq 10^4$), where fracture depletion occurs orders of magnitude faster than matrix drainage. Consequently, matrix flow reduces to a 1D transient problem with a constant boundary condition (P=0 at x=±a).

This work relaxes Hazlett's et al (2024) assumption by introducing a time-dependent average fracture pressure, $\bar{P}_f(t)$, enabling coupled fracture-matrix dynamics. This modification captures gradual fracture depletion, critical for reservoirs with moderate k_f/k_x ratios. Matrix depletion is still modeled as one-dimensional flow, but the average fracture pressure compensates for spatial variations in driving force for matrix depletion due to pressure gradients in the fracture.

The Key Assumptions applied for the model are:

1. Representative Element Volume (REV) treatment.
2. Transient 1D flow.
3. Spatially averaged fracture pressure $\bar{P}_f(t)$ as characteristic matrix depletion driving force.
4. Single phase flow with constant fluid properties (c, μ = const) under isothermal conditions.
5. Homogeneous matrix and fracture properties.
6. Negligible influence of the source term on fracture average pressure.

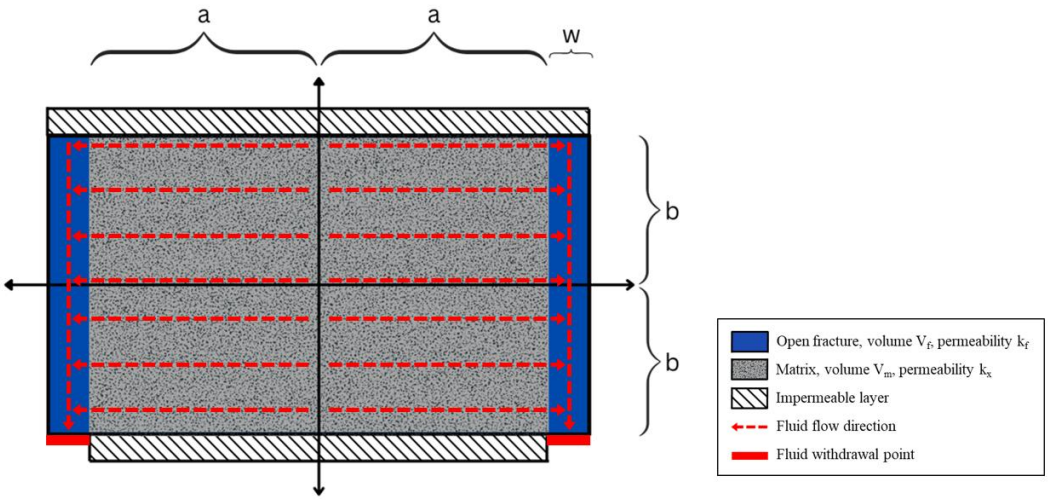

Figure 19. Representative Element Model consisting of 2D Matrix block with 2 parallel vertical fractures (blue) and withdrawal points at $(\pm a, -b)$. Based on model developed by Hazlett, et al. (2024).

3.1.2 Mathematical Formulation of Fracture Depletion

The fluid flow from fractures is similar to linear heat flow in the solid bounded by 2 parallel plates. Carslaw & Jaeger (1959) provided various solutions for describing heat conduction in solids. The governing differential equation of linear heat flow in a medium is:

$$\frac{\partial v}{\partial t} = \kappa \frac{\partial^2 v}{\partial x^2} \tag{3.1}$$

where,

v – temperature,

κ – thermal conductivity,

t – time,

x – direction of flow.

By applying initial and boundary conditions of $v = 0\ at\ x = -L\ and\ x = L\ and\ v = f(x)\ at\ t = 0$, the resulting equation describing heat flow in the slab $-L < x < L$ with constant initial temperature V_0 is (Carslaw & Jaeger, 1959):

$$v = \frac{4V_0}{\pi} \sum_{n=0}^{\infty} \frac{(-1)^n}{(2n+1)} e^{-\frac{\pi^2 \kappa}{4l^2}(2l+1)^2 t} \cos \frac{(2n+1)\pi x}{2l} \tag{3.2}$$

Hazlett, et al. (2024) used this 1D solution to describe pressure change in fractures:

$$P_f(x,t) = \frac{4P_i}{\pi} \sum_{n=0}^{\infty} \frac{(-1)^n}{(2n+1)} e^{-\frac{\pi^2 k_f}{4l^2}(2l+1)^2 \tau} \cos \frac{(2n+1)\pi x}{2l} \tag{3.3}$$

where,

P_f – pressure in the fractures, analogous of temperature v,

P_i – initial pressure, analogous of initial temperature V0,

k_f – fracture permeability, analogous of thermal conductivity κ,

τ – dimensionless time, $\tau = \frac{t}{\mu c}$.

n – dummy variable.

By further averaging and simplifying Equation (3.3) for two-sided drainage, the equation describing average fracture pressure is:

$$\frac{\bar{P}_f(t)}{P_i} = \frac{8}{\pi^2}\sum_{n=0}^{\infty}\frac{e^{-\frac{\pi^2 k_f(2n+1)^2\tau}{4b^2}}}{(2n+1)^2} \tag{3.4}$$

We note that this expression yields a correct normalized pressure value since

$$\sum_{n=0}^{\infty}\frac{1}{(2n+1)^2} = \frac{\pi^2}{8}$$

We apply this slight correction to the prior model. By defining the lumped dimensionless time,

$$t_D = \frac{k_x}{a^2}\tau = \frac{k_x}{a^2}\frac{t}{\mu c}$$

The average pressure in the fractures is (Hazlett, Syrymov, & Younis, 2024):

$$\frac{\bar{P}_f(t)}{P_i} = \frac{8}{\pi^2}\sum_{n=0}^{\infty}\frac{e^{-\frac{\pi^2}{4}(2n+1)^2 t_D\left(\frac{k_f}{k_x}\right)\left(\frac{a}{b}\right)^2}}{(2n+1)^2} \tag{3.5}$$

To amplify small changes in pressure response, it is common practice to compute its Bourdet derivative. Bourdet derivative is widely used in well testing to identify flow regimes and conduct further analysis.

To derive the Bourdet derivative of pressure, the following definition can be applied:

$$\frac{d\frac{\bar{P}_f(t_D)}{P_i}}{dlnt_D} = t_D * \frac{d\frac{\bar{P}_f(t_D)}{P_i}}{dt_D} \tag{3.6}$$

The Bourdet derivative of the average dimensionless pressure in the fractures is:

$$\frac{d\frac{\bar{P}_f(t)}{P_i}}{dlnt_D} = t_D\left\{2\left(\frac{k_f}{k_x}\right)\left(\frac{a}{b}\right)^2\sum_{n=0}^{\infty}e^{-\frac{\pi^2}{4}(2n+1)^2 t_D\left(\frac{k_f}{k_x}\right)\left(\frac{a}{b}\right)^2}\right\} \tag{3.7}$$

Since it is impossible to measure the average fracture pressure, it is proposed to relate the change in average pressure to the cumulative fluid produced. The equation for instantaneous flow rate, *q*, for either matrix or fracture is

$$q = -cV_{ref}\frac{d\bar{p}}{dt} \tag{3.8}$$

where,

c – compressibility of the reservoir fluid,

V_{ref} – reference volume of the fluid.

Thus, the instantaneous flow rate from the fracture is:

$$q_f = 2\frac{P_i V_m}{\mu}\left(\frac{V_f}{V_m}\right)\left(\frac{k_x}{a^2}\right)\left(\frac{k_f}{k_x}\right)\left(\frac{a}{b}\right)^2 \sum_{n=0}^{\infty} e^{-\frac{\pi^2}{4}(2n+1)^2 t_D\left(\frac{k_f}{k_x}\right)\left(\frac{a}{b}\right)^2} \tag{3.9}$$

It should be noted that Equations (3.5), (3.7), and (3.9) are both used for previous and new approach computation of average dimensionless pressure.

3.1.3 Mathematical Formulation of Matrix Depletion

To describe matrix depletion, the solution by Carslaw & Jaeger (1959) for linear heat flow in the solid bounded by 2 parallel plates can be also used as for the fracture depletion. However, in this instance, Equation (3.1) is solved with the following initial and boundary conditions:

$$\frac{dv}{dx} = 0, when\ x = 0$$
$$v = \phi_2(t), when\ x = L$$
$$v = f(x), when\ t = 0$$

By applying Duhamel's Theorem, the solution by Carslaw & Jaeger (1959) is:

$$v = \frac{2}{l}\sum_{n=0}^{\infty} e^{-\frac{\kappa(2n+1)^2\pi^3 l}{4l^2}} \cos\frac{(2n+1)\pi x}{2l}\left\{\frac{(2n+1)\pi\kappa(-1)^n}{2l}\int_0^l e^{\frac{\kappa(2n+1)^2\pi^2\lambda}{4l^2}}\phi_2(\lambda)\partial\lambda + \int_0^l f(x')\cos\frac{(2n+1)\pi x'}{2l}dx'\right\} \tag{3.10}$$

By applying the analogy between heat conduction and mass transport:

$$\frac{P_m(x,t)}{P_i} = \frac{2}{a}\sum_{m=0}^{\infty} e^{-\frac{\pi^2 k_x(2m+1)^2 t}{4a^2}} \cos\frac{\pi(2m+1)x}{2a}\left[\int_0^a \cos\frac{\pi(2m+1)\hat{x}}{2a}d\hat{x} + \frac{\pi(2m+1)k_x(-1)^m}{2a}\int_0^t e^{\frac{\pi^2 k_x(2m+1)^2\tau}{4a^2}}\eta(\tau)d\tau\right] \tag{3.11}$$

where the boundary value pressure takes on the spatially independent average pressure in the depleting boundary fracture,

$$\eta(\tau) = \frac{\bar{P}_f}{P_i} = \frac{8}{\pi^2}\sum_{n=0}^{\infty}\frac{e^{-\frac{\pi^2 k_f (2n+1)^2 \tau}{4b^2}}}{(2n+1)^2} \tag{3.12}$$

With further simplification and spatial averaging, the average pressure in the matrix is:

$$\left(\frac{\bar{P}_m(t)}{P_i}\right)_{new} = \frac{8}{\pi^2}\sum_{m=0}^{\infty}\frac{e^{-\frac{\pi^2}{4}(2m+1)^2 t_D}}{(2m+1)^2} + \frac{64}{\pi^4}\sum_{m=0}^{\infty}\sum_{n=0}^{\infty}\frac{e^{-\frac{\pi^2}{4}(2m+1)^2 t_D} - e^{-\frac{\pi^2}{4}\left[\left(\frac{k_f}{k_x}\right)\left(\frac{a}{b}\right)^2 (2n+1)^2\right] t_D}}{(2n+1)^2\left[\left(\frac{k_f}{k_x}\right)\left(\frac{a}{b}\right)^2 (2n+1)^2 - (2m+1)^2\right]} \tag{3.13}$$

The Bourdet derivative of the average dimensionless pressure in the matrix is:

$$\left(\frac{d\frac{\bar{P}_m(t)}{P_i}}{dlnt_D}\right)_{new}$$

$$= 2t_D\left\{\frac{8}{\pi^2}\sum_{m=0}^{\infty}\sum_{n=0}^{\infty}\frac{\left(\frac{k_f}{k_x}\right)\left(\frac{a}{b}\right)^2 e^{-\frac{\pi^2}{4}\left[\left(\frac{k_f}{k_x}\right)\left(\frac{a}{b}\right)^2 (2n+1)^2\right] t_D} - \left(\frac{2m+1}{2n+1}\right)^2 e^{-\frac{\pi^2}{4}(2m+1)^2 t_D}}{\left[\left(\frac{k_f}{k_x}\right)\left(\frac{a}{b}\right)^2 (2n+1)^2 - (2m+1)^2\right]}\right.$$

$$\left. - \sum_{m=0}^{\infty} e^{-\frac{\pi^2}{4}(2m+1)^2 t_D}\right\} \tag{3.14}$$

Equation (3.13) adds the second matrix-fracture coupling term that is absent from previous result which was simply

$$\left(\frac{\bar{P}_m(t)}{P_i}\right)_{prev} = \frac{8}{\pi^2}\sum_{m=0}^{\infty}\frac{e^{-\frac{\pi^2}{4}(2m+1)^2 t_D}}{(2m+1)^2} \tag{3.15}$$

and its Bourdet derivative is:

$$\left(\frac{d\frac{\bar{P}_m(t)}{P_i}}{dlnt_D}\right)_{prev} = 2t_D\left\{\sum_{m=0}^{\infty} e^{-\frac{\pi^2}{4}(2m+1)^2 t_D}\right\} \tag{3.16}$$

The instantaneous flow rate, q_m, for the matrix is derived from Equations (3.8) and (3.13):

$$q_{m,new}$$

$$= 2\frac{P_i V_m}{\mu}\left(\frac{k_x}{a^2}\right)\left\{\frac{8}{\pi^2}\sum_{m=0}^{\infty}\sum_{n=0}^{\infty}\frac{\left(\frac{k_f}{k_x}\right)\left(\frac{a}{b}\right)^2 e^{-\frac{\pi^2}{4}\left[\left(\frac{k_f}{k_x}\right)\left(\frac{a}{b}\right)^2(2n+1)^2\right]t_D} - \left(\frac{2m+1}{2n+1}\right)^2 e^{-\frac{\pi^2}{4}(2m+1)^2 t_D}}{\left[\left(\frac{k_f}{k_x}\right)\left(\frac{a}{b}\right)^2(2n+1)^2-(2m+1)^2\right]}\right.$$

$$\left. -\sum_{m=0}^{\infty} e^{-\frac{\pi^2}{4}(2m+1)^2 t_D}\right\} \tag{3.17}$$

This formulation introduces a novel double summation over both m and n that incorporates additional decay factors through exponential terms, thereby extending the original derivation.

In contrast, earlier work employed a simplified form of the flow rate, derived from Equations (3.8) and (3.15), given by:

$$q_{m,prev} = \frac{P_i V_m}{\mu}\left(\frac{k_x}{a^2}\right)\left\{\sum_{m=0}^{\infty} e^{-\frac{\pi^2}{4}(2m+1)^2 t_D}\right\} \tag{3.18}$$

3.1.4 Mathematical Formulation of the Total System

The total dimensionless average pressure of the system is the volume-weighted average of matrix and fracture pressure:

$$\frac{\overline{P}(t)}{P_i} = \left(\frac{V_m}{V_f + V_m}\right)\frac{\bar{P}_m(t)}{P_i} + \left(\frac{V_f}{V_f + V_m}\right)\frac{\bar{P}_f(t)}{P_i} \tag{3.19}$$

which can be also re-written as:

$$\left(\frac{\bar{P}(t)}{P_i}\right)_{new} = \frac{8}{\pi^2}\left(\frac{1}{\frac{V_f}{V_m}+1}\right)\left\{\sum_{m=0}^{\infty}\frac{e^{-\frac{\pi^2}{4}(2m+1)^2 t_D}}{(2m+1)^2}\right.$$
$$+\frac{8}{\pi^2}\sum_{m=0}^{\infty}\sum_{n=0}^{\infty}\frac{e^{-\frac{\pi^2}{4}(2m+1)^2 t_D}-e^{-\frac{\pi^2}{4}\left[\left(\frac{k_f}{k_x}\right)\left(\frac{a}{b}\right)^2(2n+1)^2\right]t_D}}{(2n+1)^2\left[\left(\frac{k_f}{k_x}\right)\left(\frac{a}{b}\right)^2(2n+1)^2-(2m+1)^2\right]}$$
$$\left.+\frac{V_f}{V_m}\sum_{n=0}^{\infty}\frac{e^{-\frac{\pi^2}{4}(2n+1)^2 t_D\left(\frac{k_f}{k_x}\right)\left(\frac{a}{b}\right)^2}}{(2n+1)^2}\right\} \tag{3.20}$$

The Bourdet derivative of the average dimensionless pressure of the total system is:

$$\left(\frac{d\left(\frac{\bar{P}(t)}{P_i}\right)}{dlnt_D}\right)_{new}$$
$$=-2t_D\left(\frac{1}{1+\frac{V_f}{V_m}}\right)\left\{\sum_{m=0}^{\infty}e^{-\frac{\pi^2}{4}(2m+1)^2 t_D}\right.$$
$$+\frac{8}{\pi^2}\sum_{m=0}^{\infty}\sum_{n=0}^{\infty}\frac{\frac{(2m+1)^2}{(2n+1)^2}e^{-\frac{\pi^2}{4}(2m+1)^2 t_D}-\left(\frac{k_f}{k_x}\right)\left(\frac{a}{b}\right)^2 e^{-\frac{\pi^2}{4}\left[\left(\frac{k_f}{k_x}\right)\left(\frac{a}{b}\right)^2(2n+1)^2\right]t_D}}{\left[\left(\frac{k_f}{k_x}\right)\left(\frac{a}{b}\right)^2(2n+1)^2-(2m+1)^2\right]}$$
$$\left.+\frac{V_f}{V_m}\left(\frac{k_f}{k_x}\right)\left(\frac{a}{b}\right)^2\sum_{n=0}^{\infty}e^{-\frac{\pi^2}{4}(2n+1)^2 t_D\left(\frac{k_f}{k_x}\right)\left(\frac{a}{b}\right)^2}\right\} \tag{3.21}$$

Total instantaneous production rate of the system can be derived using Equations (3.8) and (3.20):

$$q_{new} = 2\frac{P_i V_m}{\mu}\left(\frac{k_x}{a^2}\right)\left\{\sum_{m=0}^{\infty} e^{-\frac{\pi^2}{4}(2m+1)^2 t_D} + \frac{8}{\pi^2}\sum_{m=0}^{\infty}\sum_{n=0}^{\infty}\frac{\frac{(2m+1)^2}{(2n+1)^2}e^{-\frac{\pi^2}{4}(2m+1)^2 t_D} - \left(\frac{k_f}{k_x}\right)\left(\frac{a}{b}\right)^2 e^{-\frac{\pi^2}{4}\left[\left(\frac{k_f}{k_x}\right)\left(\frac{a}{b}\right)^2(2n+1)^2\right]t_D}}{\left[\left(\frac{k_f}{k_x}\right)\left(\frac{a}{b}\right)^2(2n+1)^2 - (2m+1)^2\right]} + \frac{V_f}{V_m}\left(\frac{k_f}{k_x}\right)\left(\frac{a}{b}\right)^2\sum_{n=0}^{\infty} e^{-\frac{\pi^2}{4}(2n+1)^2 t_D\left(\frac{k_f}{k_x}\right)\left(\frac{a}{b}\right)^2}\right\} \quad (3.22)$$

Contrastingly, results published by Hazlett et al. (2024) expressed total dimensionless average pressure, its Bourdet derivative and instantaneous flow rate of the system without matrix-fracture coupling term as follows:

$$\left(\frac{\bar{P}(t)}{P_i}\right)_{prev} = \frac{8}{\pi^2}\left(\frac{1}{\frac{V_f}{V_m}+1}\right)\left\{\sum_{m=0}^{\infty}\frac{e^{-\frac{\pi^2}{4}(2m+1)^2 t_D}}{(2m+1)^2} + \left(\frac{V_f}{V_m}\right)\sum_{n=0}^{\infty}\frac{e^{-\frac{\pi^2}{4}(2n+1)^2 t_D\left(\frac{k_f}{k_x}\right)\left(\frac{a}{b}\right)^2}}{(2n+1)^2}\right\} \quad (3.23)$$

$$\left(\frac{d\left(\frac{\bar{P}(t)}{P_i}\right)}{dlnt_D}\right)_{prev} = -2t_D\left(\frac{1}{\frac{V_f}{V_m}+1}\right)\left\{\sum_{m=0}^{\infty} e^{-\frac{\pi^2}{4}(2m+1)^2 t_D} + \left(\frac{V_f}{V_m}\right)\left(\frac{k_f}{k_x}\right)\left(\frac{a}{b}\right)^2\sum_{n=0}^{\infty} e^{-\frac{\pi^2}{4}(2n+1)^2 t_D\left(\frac{k_f}{k_x}\right)\left(\frac{a}{b}\right)^2}\right\} \quad (3.24)$$

$$q_{prev} = 2\frac{P_i V_m}{\mu}\left(\frac{k_x}{a^2}\right)\left\{\sum_{m=0}^{\infty} e^{-\frac{\pi^2}{4}(2m+1)^2 t_D} + \frac{V_f}{V_m}\left(\frac{k_f}{k_x}\right)\left(\frac{a}{b}\right)^2\sum_{n=0}^{\infty} e^{-\frac{\pi^2}{4}(2n+1)^2 t_D\left(\frac{k_f}{k_x}\right)\left(\frac{a}{b}\right)^2}\right\} \quad (3.25)$$

3.1.5 Introduction of Scaling Factor

Equations (3.20) and (3.22) were introduced for a system comprising of a single representative element size for a matrix block drained by parallel fractures. However, in order to make the model more realistic and entertain mixtures, a parameter is introduced that will account for different sized elements – scaling factor S.

The main goal of the scaling factor is to adjust dimensionless time t_D to reflect changes in physical matrix size:

$$t_D = \frac{k_x}{a^2}\frac{t}{\phi\mu c} \rightarrow t_D = \frac{k_x}{\left(S * a_{ref}\right)^2}\frac{t}{\phi\mu c} \rightarrow t_D = t_{D,ref} * \frac{1}{S^2}$$

Thus, *S* is a magnification factor on the characteristic block dimension, *a*. However, it should be noted that with this scaling factor, it is assumed that both fractures and matrices (meaning both *a* and *b*) scale altogether. Therefore, larger matrix blocks (larger *a*) shift t_D for the same physical time *t*, reflecting slower pressure diffusion in larger systems.

Therefore, Equations (3.5) and (3.13) will be affected as follows:

$$\frac{\bar{P}_m(t)}{P_i} = \frac{8}{\pi^2}\sum_{m=0}^{\infty}\frac{e^{-\frac{\pi^2}{4}(2m+1)^2\boldsymbol{t_{D,ref}}\frac{\mathbf{1}}{\boldsymbol{S^2}}}}{(2m+1)^2} + \frac{64}{\pi^4}\sum_{m=0}^{\infty}\sum_{n=0}^{\infty}\frac{e^{-\frac{\pi^2}{4}(2m+1)^2\boldsymbol{t_{D,ref}}\frac{\mathbf{1}}{\boldsymbol{S^2}}} - e^{-\frac{\pi^2}{4}\left[\left(\frac{k_f}{k_x}\right)\left(\frac{a}{b}\right)^2(2n+1)^2\right]\boldsymbol{t_{D,ref}}\frac{\mathbf{1}}{\boldsymbol{S^2}}}}{(2n+1)^2\left[\left(\frac{k_f}{k_x}\right)\left(\frac{a}{b}\right)^2(2n+1)^2 - (2m+1)^2\right]} \quad (3.26)$$

$$\frac{\bar{P}_f(t)}{P_i} = \frac{8}{\pi^2}\sum_{n=0}^{\infty}\frac{e^{-\frac{\pi^2}{4}(2n+1)^2\left(\frac{k_f}{k_x}\right)\left(\frac{a}{b}\right)^2\boldsymbol{t_{D,ref}}\frac{\mathbf{1}}{\boldsymbol{S^2}}}}{(2n+1)^2} \quad (3.27)$$

Accordingly, the overall system equations (3.20), (3.21), and (3.22) will also be reformulated to include the $\boldsymbol{t_{D,ref}}\frac{\mathbf{1}}{\boldsymbol{S^2}}$ term instead of the original t_D.

3.2 Numerical Implementation in Python

The Python programming language was implemented to calculate and plot dimensionless pressure $\frac{\bar{P}(t)}{P_i}$ (Equation 3.18), normalized rate $\frac{q}{q_i}$ (Equation 3.20), and their Bourdet derivatives as the function of dimensionless time t_D for various permeability ratios $\frac{k_f}{k_x}$, fracture volume fractions v_f, v_m, aspect ratios $\frac{a}{b}$ and scaling factors *S*.

Fracture volume fraction is defined as

$$v_f = \frac{V_f}{V_f + V_m}$$

and introduced instead of V_f/V_m for interpretation convenience. V_f/V_m can be computed from v_f by:

$$\frac{V_f}{V_m} = \frac{v_f}{1 - v_f}$$

Therefore, matrix volume fraction is $v_m = 1 - v_f$.

First, infinite sums in the equations were truncated by incrementing dummy indices m and n until the partial-sum residual fell below tolerance of 10^{-6}. All single-sum series converged below specified tolerance (See Appendix A-1 and A-2).

The obtained plots were then verified and compared with the previous work done by Hazlett, et al. (2024) and then further analyzed to retrieve any relationships between input variables. The results obtained are provided in the next chapter. The flowchart of code algorithm is depicted below.

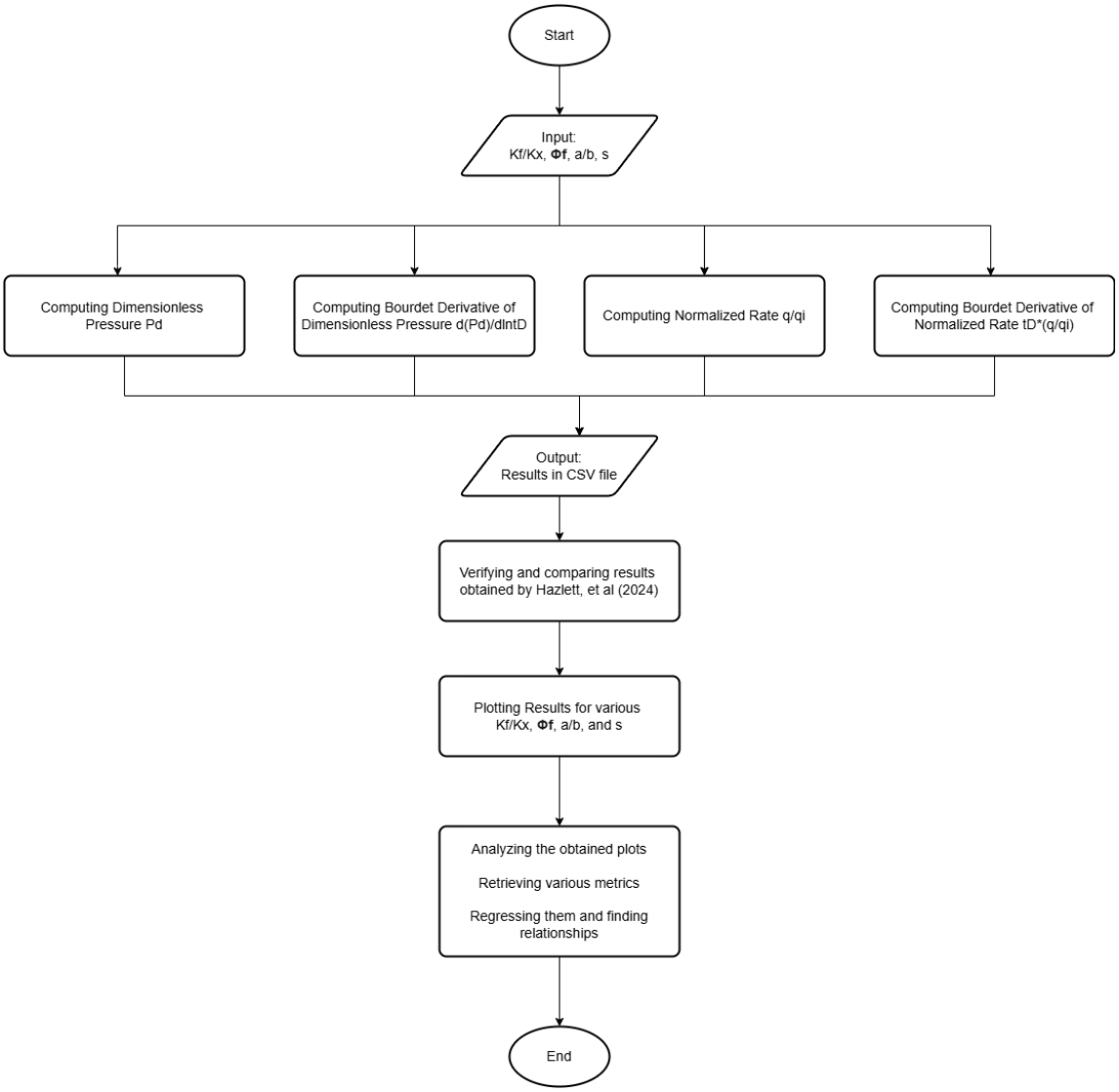

Figure 20. Flowchart of code algorithm

4. RESULTS

This chapter presents an analysis of the numerical outcomes derived from the analytical representative element model, focusing on validation against the study by Hazlett et al. (2024) and sensitivity to key parameters, namely the permeability ratio k_f/k_x, fracture volume fraction v_f, aspect ratio a/b, and scaling factor S.

4.1 Model Validation

The first objective is to verify that the proposed solution converges, and replicates reference results reported by Hazlett et al. (2024) for the limiting case in which fracture and matrix depletion act independently.

4.1.1 Dimensionless Pressure P_D and its Bourdet Derivative $\frac{dP_D}{dlnt_D}$

Two series of curves – dimensionless pressure $P_D(t_D)$ and its Bourdet derivative $\frac{dP_D}{dlnt_D}(t_D)$ – were generated using Equations (3.20) and (3.21). These curves were plotted as functions of dimensionless time t_D for various permeability ratios k_f/k_x and fracture volume fractions v_f for constant aspect ratio $a/b = 1$ and scaling factor $S = 1$. The obtained results were compared to the findings from previous work (Hazlett, et al., 2024) which were calculated using Equations (3.23) and (3.24).

Figures 21-24 compare the dimensionless pressure and its Bourdet derivative results obtained by the new model (solid lines) with Hazlett et al. (dashed). For permeability ratios of $k_f/k_x > 10^4$, there is a strong agreement between the new model and with previously reported findings by Hazlett et al. (2024). However, for permeability ratios of $k_f/k_x \leq 10^4$, there is a departure between dimensionless pressure responses, as can be seen from the figures. This departure is certainly expected as the new solution couples the matrix depletion with fracture depletion as dependent events, unlike the model used in previous work. Above $k_f/k_x > 10^4$ threshold, pressure decreases more rapidly, and derivative peak shifts left, reflecting quick fracture depletion during early times that is captured by both previous and new models.

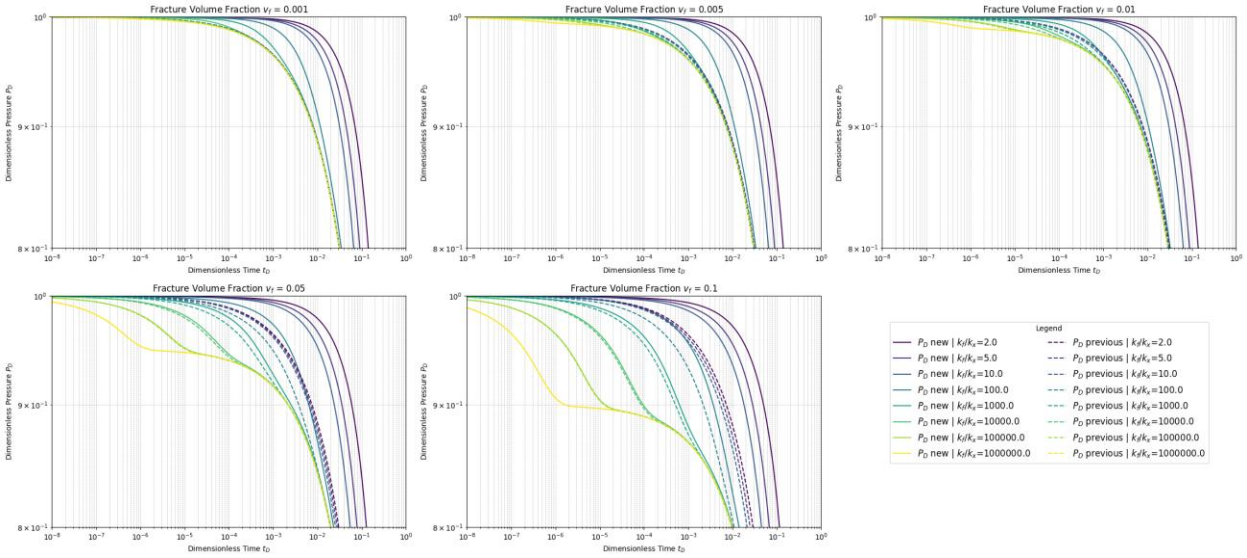

Figure 21. Dimensionless pressure P_D as a function of dimensionless time t_D for various v_f and k_f/k_x

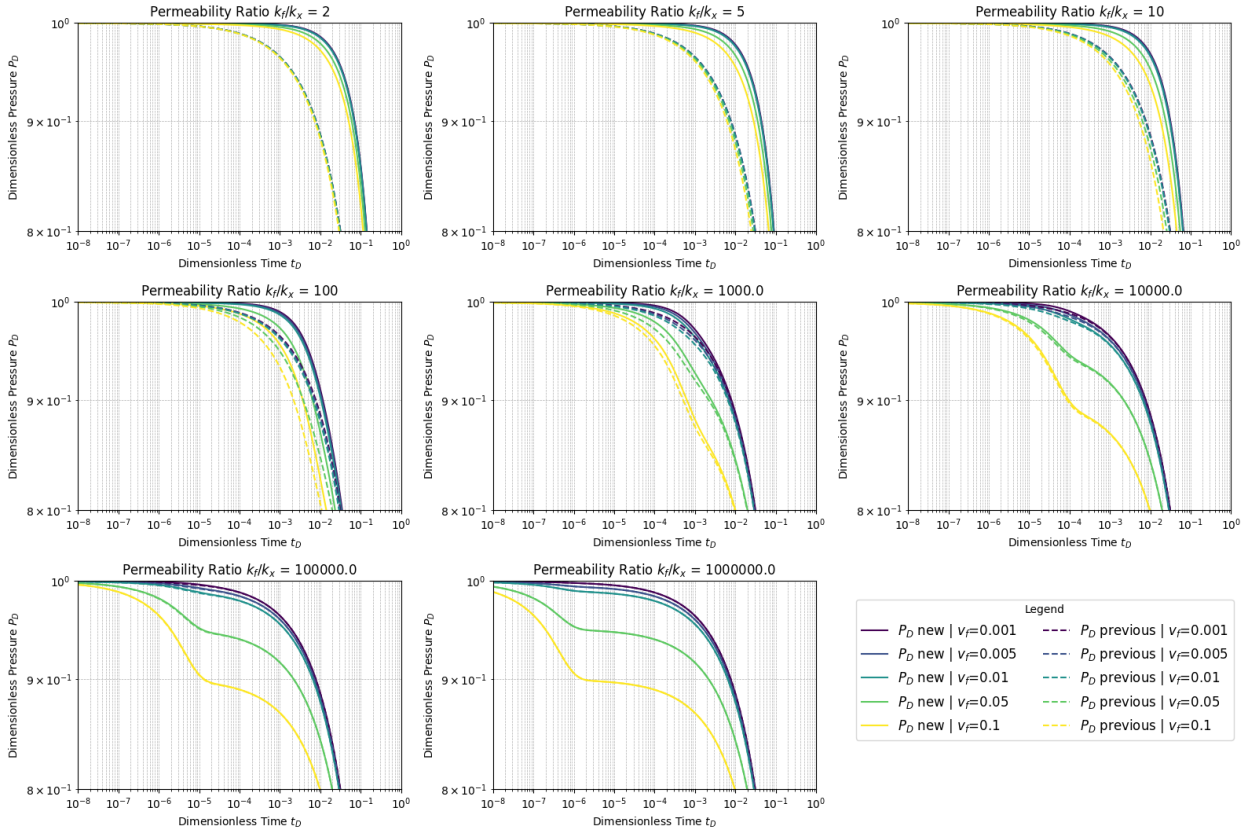

Figure 22. Dimensionless pressure P_D as a function of dimensionless time t_D for various k_f/k_x and v_f

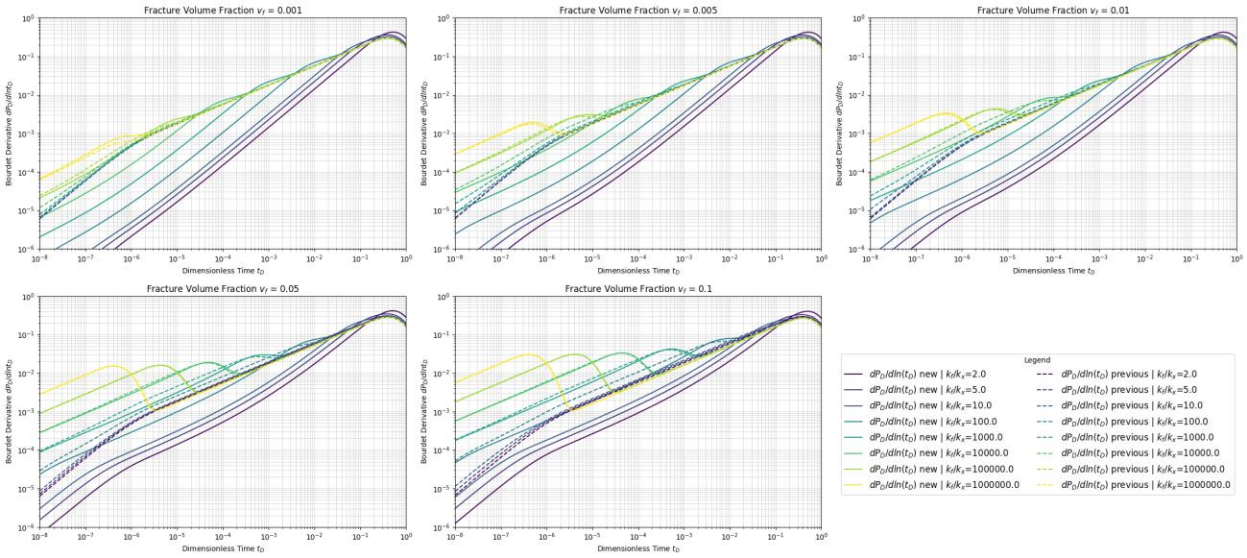

Figure 23. Bourdet Derivative of dimensionless pressure as function of dimensionless time t_D for various v_f and k_f/k_x

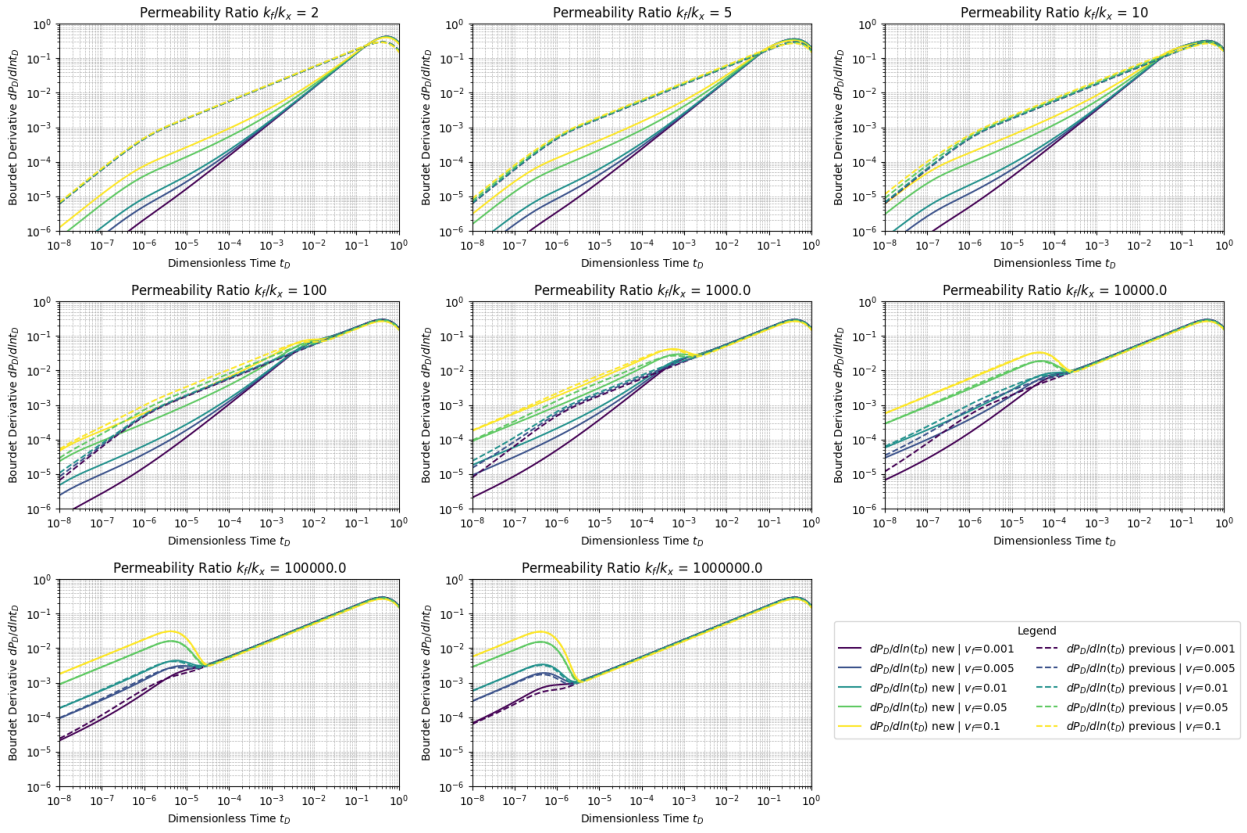

Figure 24. Bourdet Derivative of dimensionless pressure as function of dimensionless time t_D for various k_f/k_x and v_f

4.1.2 Normalized Rate q/q_i and its Bourdet Derivative $t_D(q/q_i)$

The normalized rate for q/q_i both previous and new approach was calculated using instantaneous flow rates for the total system using Equations (3.22) and (3.25), where initial rate $q_i = q(t_D = 10^{-8})$. Both normalized rate q/q_i and its Bourdet derivative $t_D\left(\frac{q}{q_i}\right)$ were plotted as functions of dimensionless time t_D for various permeability ratios k_f/k_x and fracture volume fractions v_f and fixed aspect ratio $a/b = 1$ and scaling factor $S = 1$ and were compared to the findings from previous work.

Figures 25 – 28 again show perfect agreement for ratios $k_f/k_x > 10^4$ and a systematic departure at lower ratios. Notably, even at high permeability ratios, a discrepancy between the new and previous approaches persists for fracture volume fractions of $v_f < 0.01$.

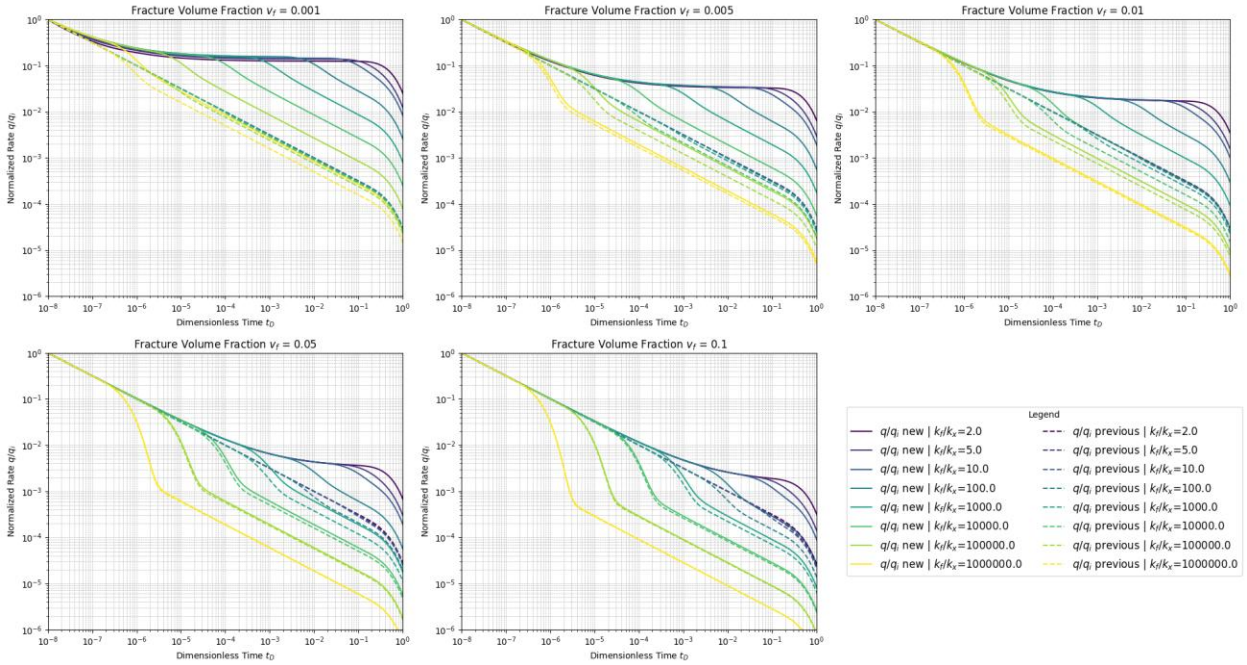

Figure 25. Normalized Rate q/q_i as a function of dimensionless time t_D for various v_f and k_f/k_x

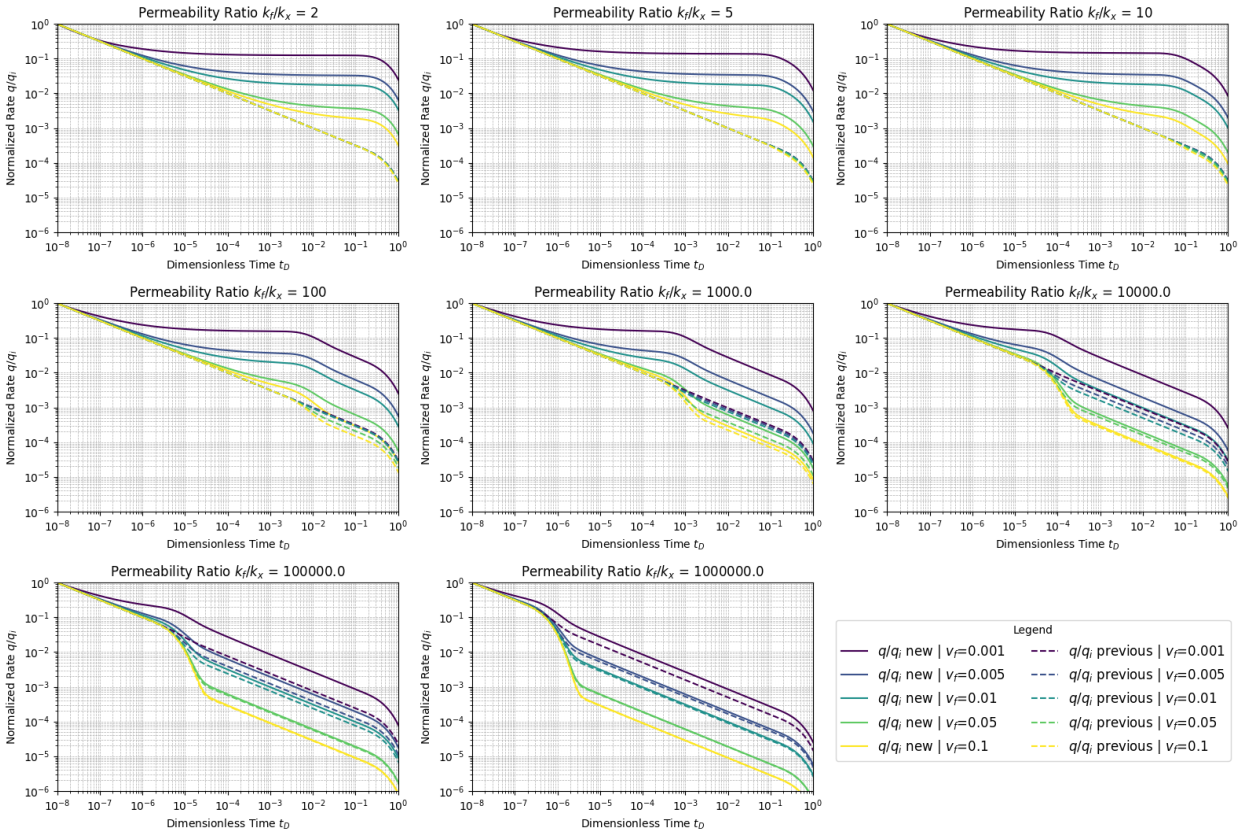

Figure 26. Normalized Rate q/q_i as a function of dimensionless time t_D for various k_f/k_x and v_f

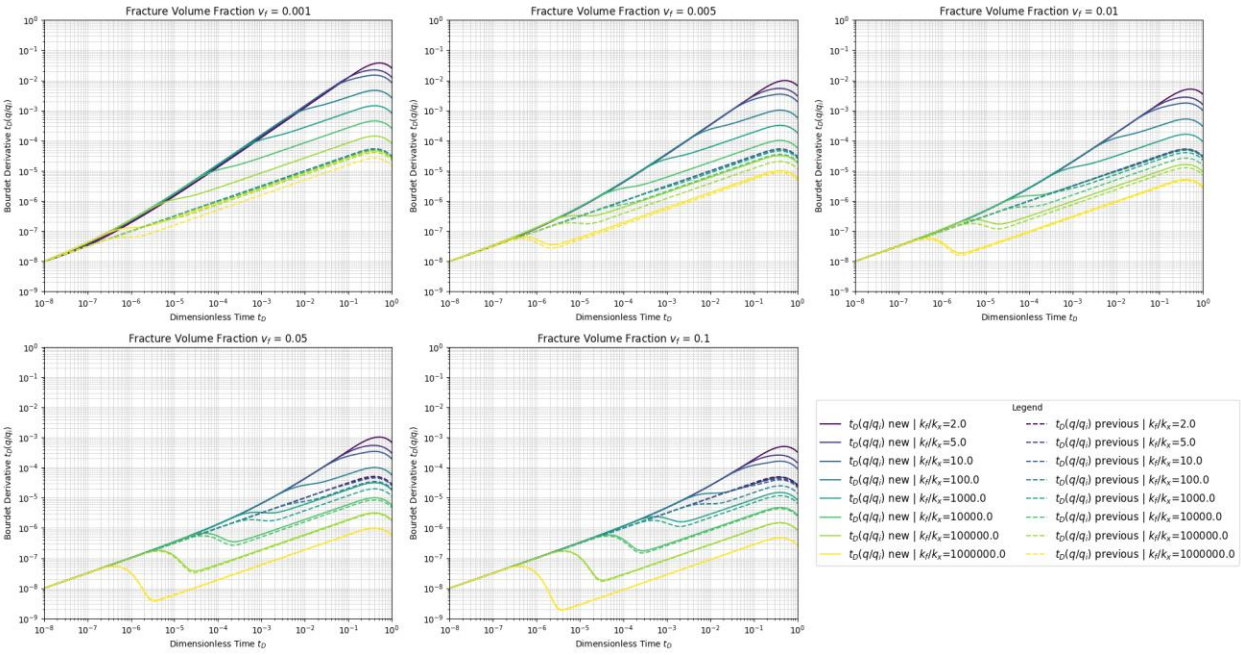

Figure 27. Bourdet Derivative of Normalized Rate as a function of dimensionless time t_D for various v_f and k_f/k_x

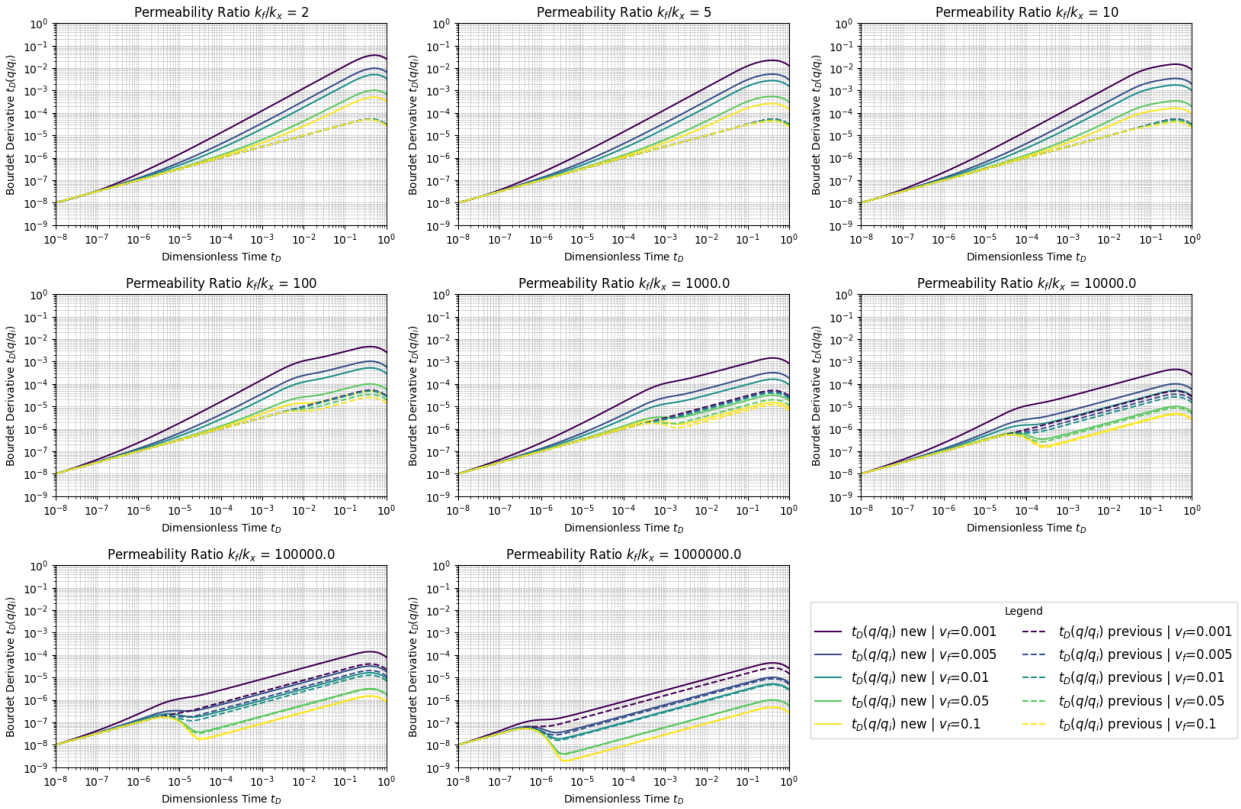

Figure 28. Bourdet Derivative of Normalized Rate as a function of dimensionless time t_D for various k_f/k_x and v_f

4.2 Sensitivity Analysis

The second objective is to quantify how model outputs respond to four key parameters: permeability ratio k_f/k_x, fracture-volume fraction v_f, matrix aspect ratio a/b, and scaling factor S. Each subsection begins with constant baseline values ($a/b = 1; S = 1$ unless otherwise stated) and varies the parameters of interest over the ranges specified in Table 7.

Table 7. Parameters investigated for sensitivity analysis

Parameter	Definition	Baseline	Range Investigated
k_f/k_x	Fracture / matrix permeability ratio	10^4	$10^3 - 10^6$
v_f	Fracture volume fraction	0.05	0.005 – 0.10
a/b	Matrix aspect ratio	1	0.1 – 10
S	Matrix-size scaling factor	1	0.1 – 10

4.2.1 Effect of k_f/k_x and v_f

Figures 29-32 isolate the role of k_f/k_x and v_f for square matrices $a/b = 1$ and $S = 1$. Each plot exhibits two ½ - slope log-log segments, corresponding to linear flow from the fracture (early) and from the matrix (late). Three quantitative metrics were extracted from every derivative curve:

1) Fracture slope and intercept
2) Matrix slope and intercept
3) Transition duration – time separation between the end of the first and start of the second ½ slope

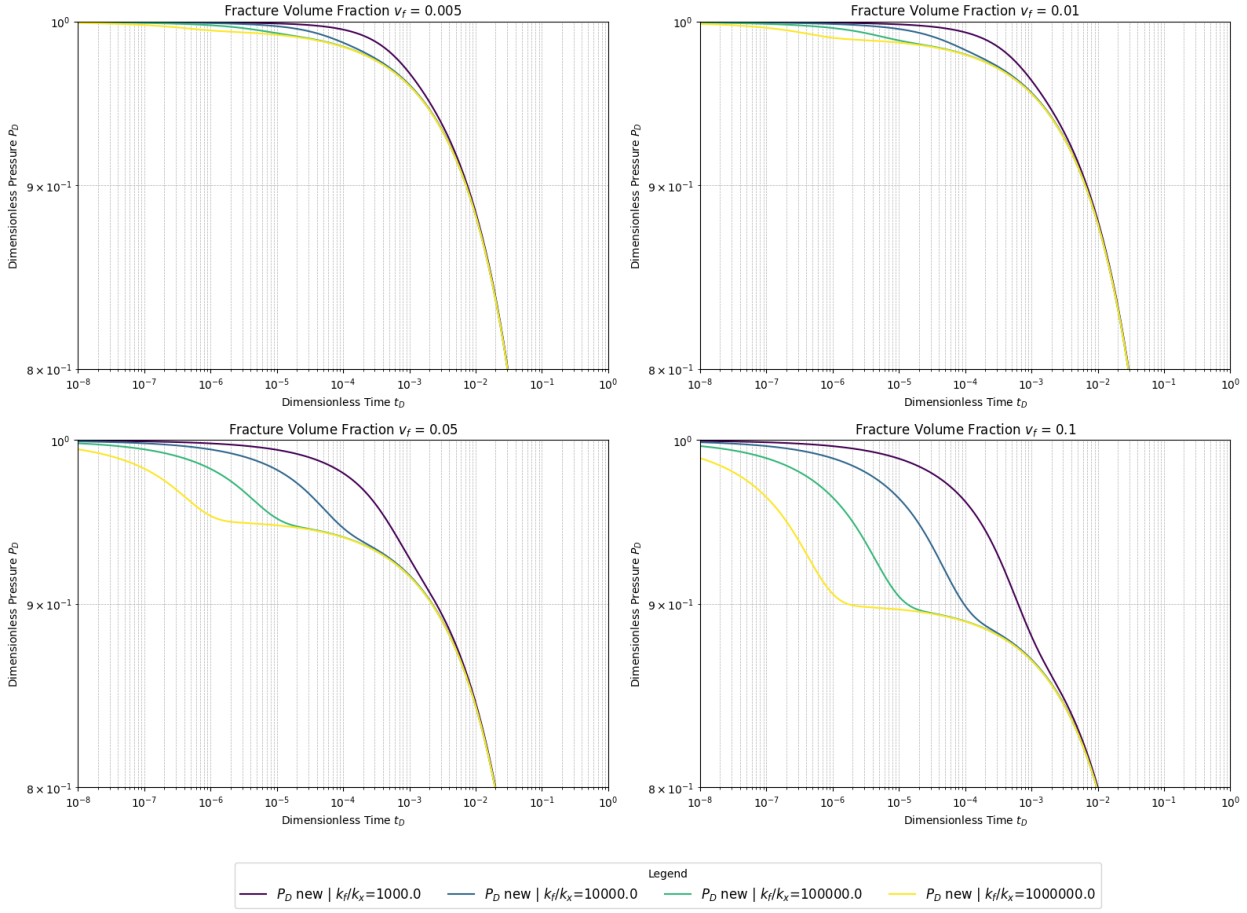

Figure 29. Dimensionless pressure P_D as a function of dimensionless time t_D for various k_f/k_x and v_f

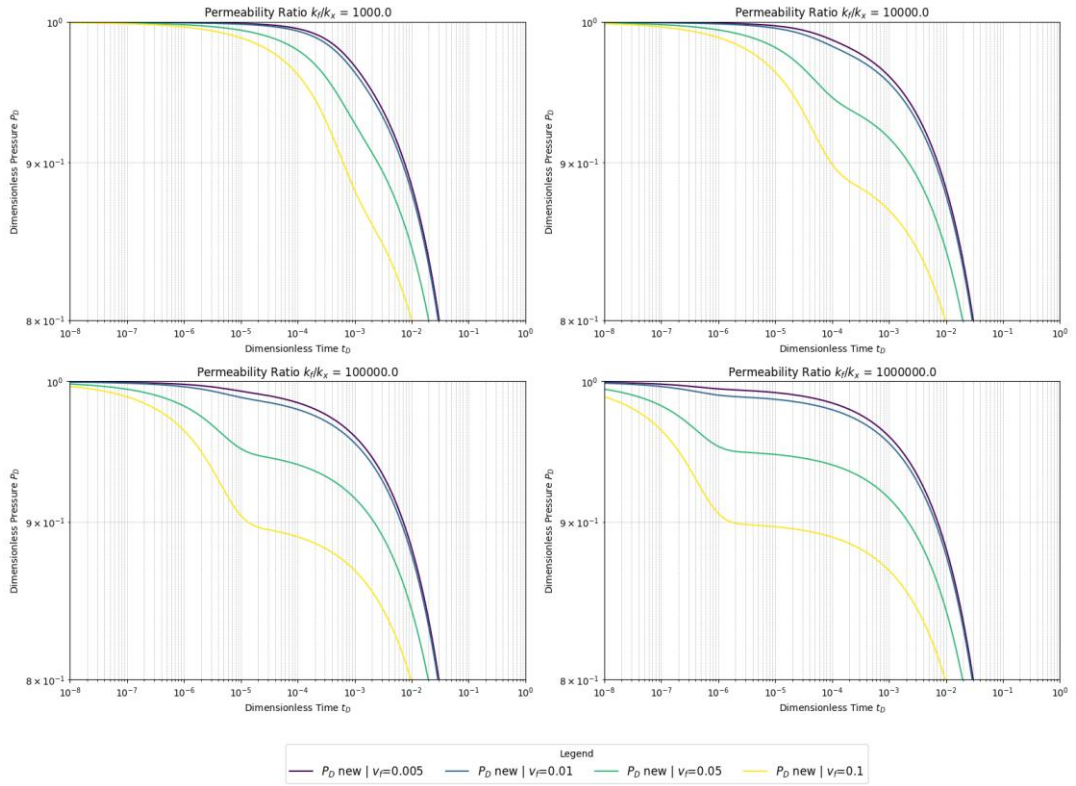

Figure 30. Dimensionless pressure P_D as a function of dimensionless time t_D for various v_f and k_f/k_x

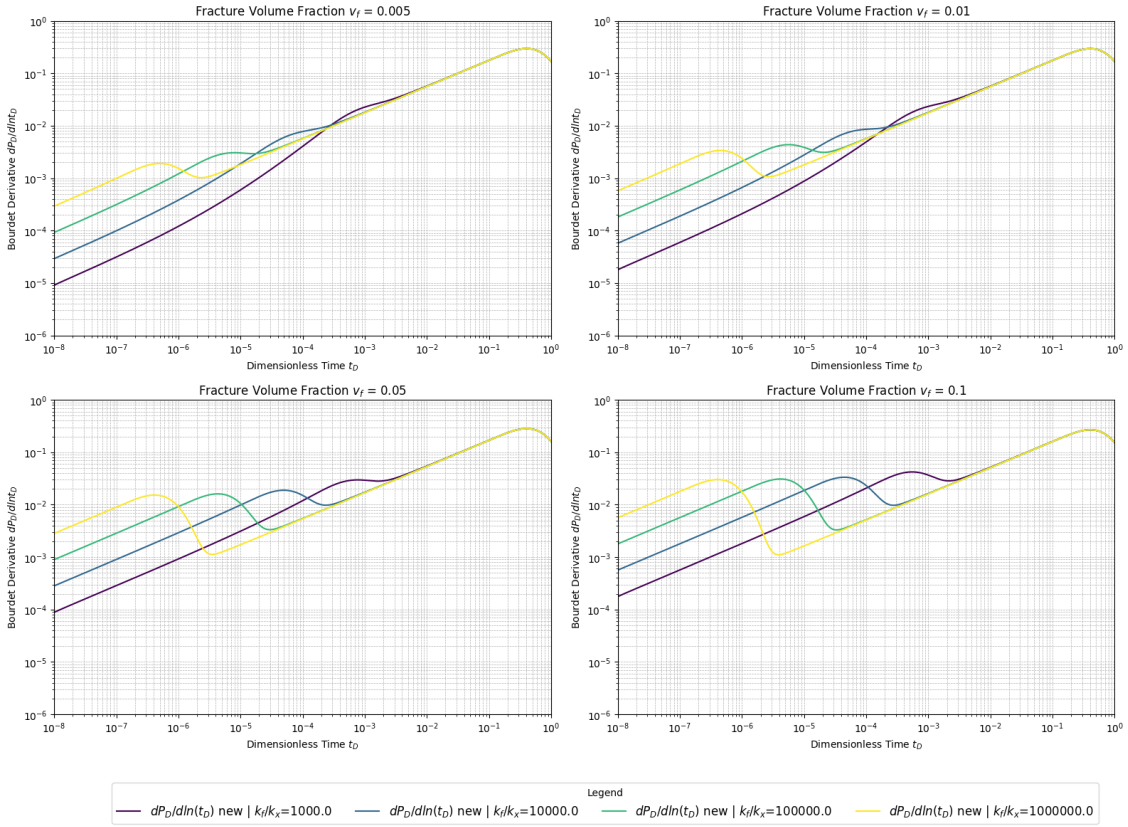

Figure 31. Bourdet Derivative of dimensionless pressure as a function of dimensionless time for various v_f and k_f/k_x

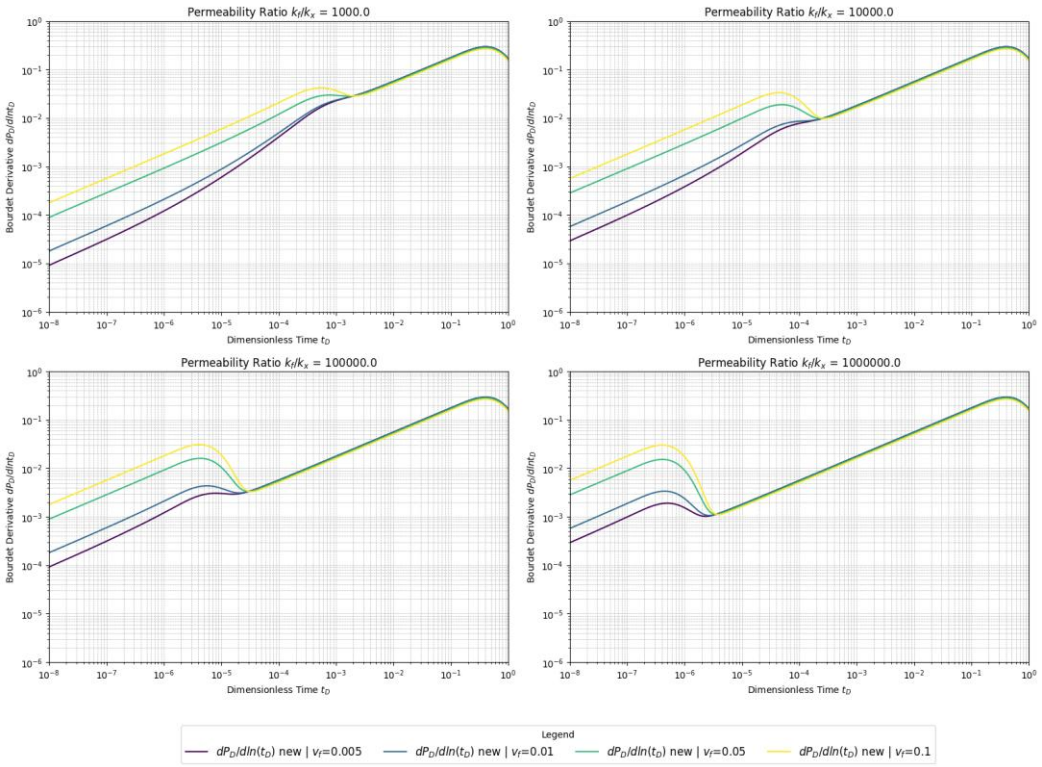

Figure 32. Bourdet Derivative of dimensionless pressure as a function of dimensionless time for various v_f and k_f/k_x

Using Bourdet derivative responses (Figures 31-32), ½ - slope log-log straight lines were identified and plotted for each k_f/k_x and v_f combinations. For instance, for $\frac{k_f}{k_x} = 10^4$ and $v_f = 0.05$, the following half-unit straight lines were identified:

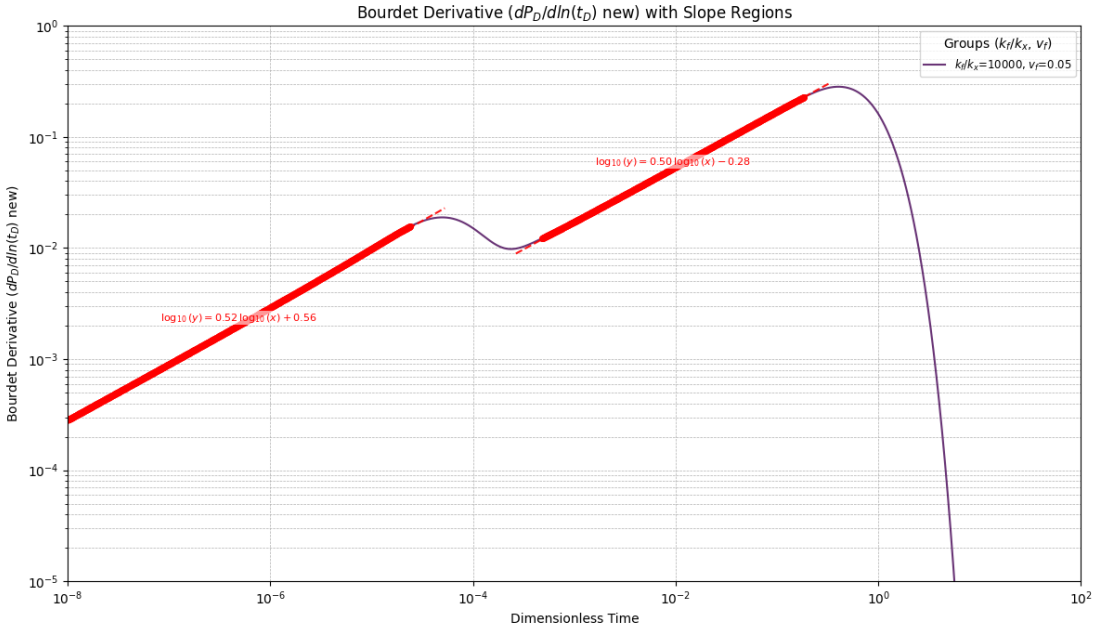

Figure 33. Bourdet Derivative response at $\frac{k_f}{k_x} = 10^4$ and $v_f = 0.05$ with half-unit slope regions

By plotting each of these combinations, it is possible to retrieve information about the exact value of the half-unit slopes, intercepts, and transition duration. A compact summary of the findings appears in Table 8. In brief, increasing k_f/k_x shortens transition duration by one order of magnitude at fixed v_f. In contrast, increasing v_f steepens difference in peak and trough of the derivative in transition zone.

Table 8. Half-unit slope and transition zone metrics based on Bourdet derivative of dimensionless pressure

k_f/k_x	v_f	Fracture contribution		Matrix contribution		Transition duration	dPd/dlntD difference in peak and trough of transition zone
		Slope	Intercept	Slope	Intercept		
1000	0.005	0.533	-0.777	0.491	-0.261	4.60E-03	1.85E-02
	0.01	0.524	-0.557	0.491	-0.263	4.60E-03	1.90E-02
	0.05	0.513	0.046	0.491	-0.281	3.90E-03	1.35E-02
	0.1	0.510	0.324	0.491	-0.304	4.66E-03	1.37E-02
10000	0.005	0.530	-0.294	0.495	-0.257	4.71E-03	6.10E-03
	0.01	0.523	-0.063	0.495	-0.260	4.62E-04	5.61E-03
	0.05	0.515	0.565	0.496	-0.277	4.64E-04	9.09E-03
	0.1	0.507	0.805	0.496	-0.301	4.56E-04	2.37E-02
100000	0.005	0.530	0.205	0.497	-0.256	4.74E-04	1.46E-03
	0.01	0.523	0.436	0.497	-0.258	4.65E-05	1.25E-03
	0.05	0.507	1.005	0.497	-0.275	4.69E-05	1.28E-02
	0.1	0.503	1.276	0.498	-0.299	4.84E-05	2.76E-02
1000000	0.005	0.531	0.708	0.498	-0.254	5.04E-05	8.86E-04
	0.01	0.517	0.895	0.498	-0.257	4.69E-06	2.31E-03
	0.05	0.503	1.472	0.498	-0.274	4.71E-06	1.42E-02
	0.1	0.501	1.758	0.499	-0.298	5.16E-06	2.91E-02

A similar analysis is done for normalized rate and its Bourdet derivative (Figures 34-37).

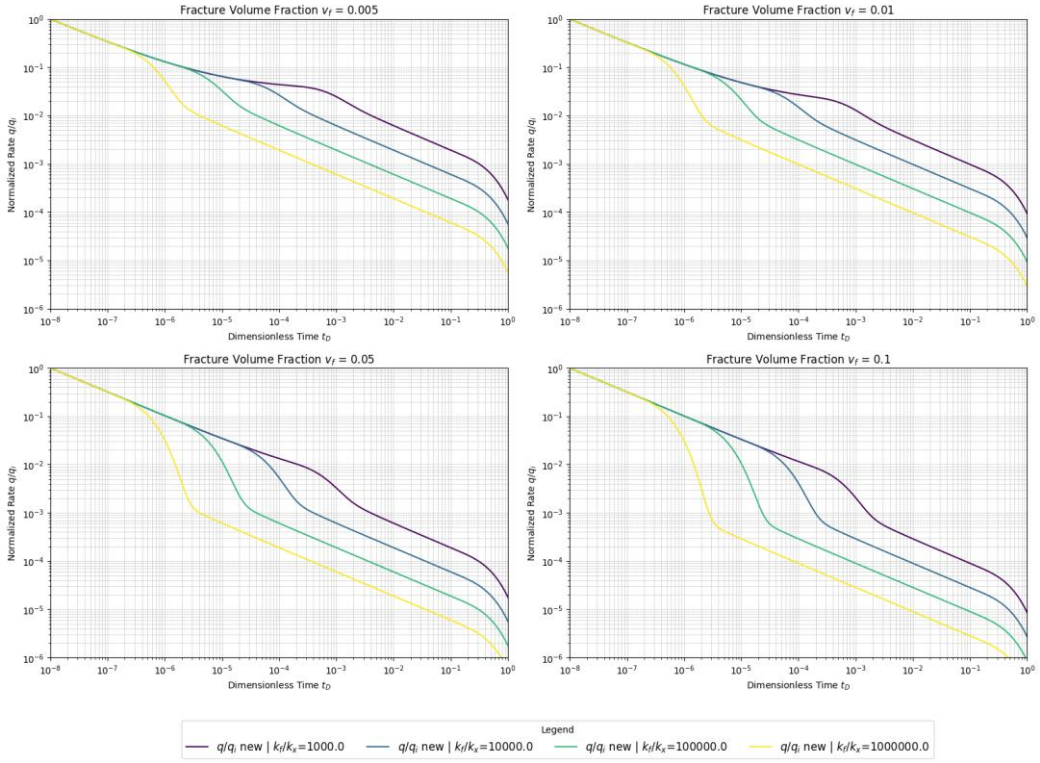

Figure 34. Normalized Rate q/q_i as a function of dimensionless time t_D for various k_f/k_x and v_f

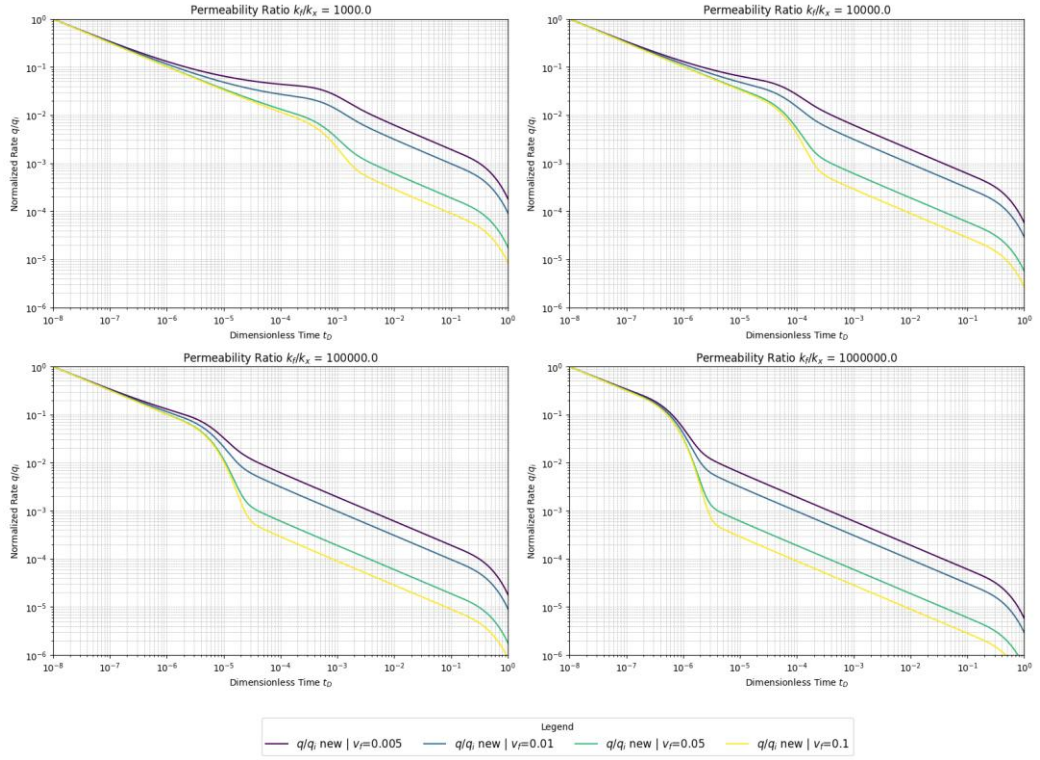

Figure 35. Normalized Rate q/q_i as a function of dimensionless time t_D for various k_f/k_x and v_f

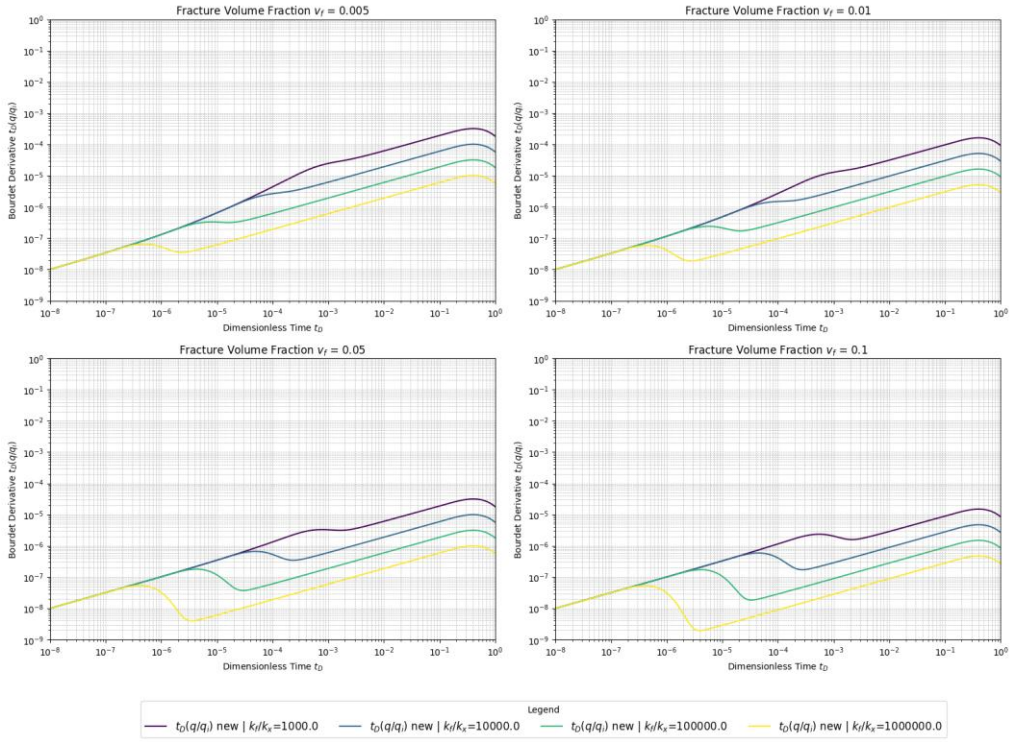

Figure 36. Bourdet Derivative of Normalized Rate as a function of dimensionless time t_D for various k_f/k_x and v_f

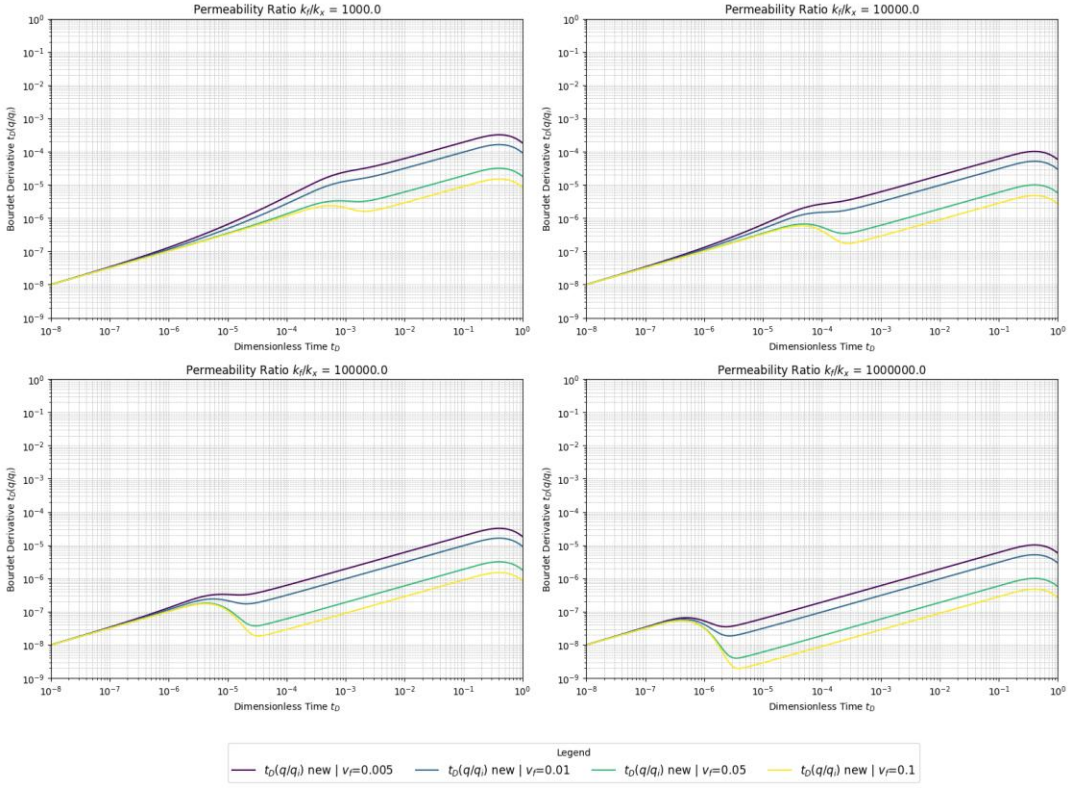

Figure 37. Bourdet Derivative of Normalized Rate as a function of dimensionless time t_D for various k_f/k_x and v_f

Similarly to Bourdet derivative of dimensionless pressure, Bourdet derivative responses of normalized rate (Figures 36-37) were also used to identify ½ - slope loglog straight lines and plotted for each k_f/k_x and v_f combinations. For instance, for $\frac{k_f}{k_x} = 10^4$ and $v_f = 0.05$, the following ½ slope straight lines were identified and corresponding metrics were recorded and summarized in Table 9.

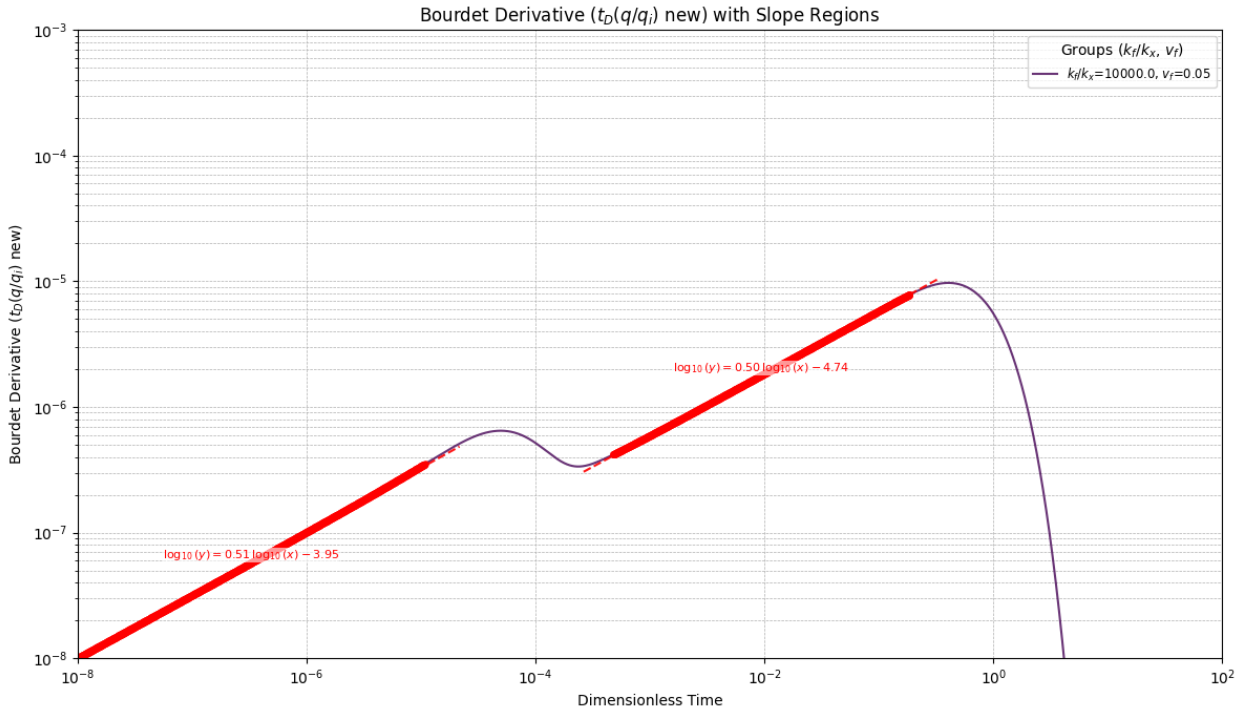

Figure 38. Bourdet Derivative response at $\frac{k_f}{k_x} = 10^4$ and $v_f = 0.05$ with half-unit slope regions

Table 9. Half-unit slope and transition zone metrics based on Bourdet derivative of normalized rate

k_f/k_x	v_f	Fracture contribution		Matrix contribution		Transition duration	tD(q/qi) difference in peak and trough of transition zone
		Slope	Intercept	Slope	Intercept		
1000	0.005	0.506	-3.956	0.491	-3.537	4.56E-03	9.70E-06
	0.01	0.506	-3.960	0.491	-3.706	4.58E-03	6.79E-06
	0.05	0.504	-3.970	0.491	-4.275	4.62E-03	1.36E-06
	0.1	0.504	-3.972	0.491	-4.577	4.67E-03	7.31E-07
10000	0.005	0.510	-3.928	0.495	-3.840	4.57E-04	1.58E-06
	0.01	0.508	-3.939	0.495	-4.081	4.61E-04	8.40E-07
	0.05	0.507	-3.953	0.496	-4.742	4.67E-04	3.11E-07

	0.1	0.505	-3.968	0.496	-5.059	4.72E-04	4.13E-07
100000	0.005	0.515	-3.885	0.497	-4.253	4.62E-05	1.45E-07
	0.01	0.512	-3.905	0.497	-4.533	4.65E-05	6.62E-08
	0.05	0.505	-3.963	0.498	-5.230	4.82E-05	1.41E-07
	0.1	0.502	-3.984	0.498	-5.552	5.04E-05	1.54E-07
1000000	0.005	0.524	-3.814	0.498	-4.724	4.67E-06	3.00E-08
	0.01	0.515	-3.882	0.498	-5.017	4.69E-06	4.01E-08
	0.05	0.502	-3.983	0.498	-5.726	5.16E-06	5.00E-08
	0.1	0.500	-3.996	0.499	-6.050	5.42E-06	5.14E-08

4.2.2 Effect of a/b and S

Figures 39-42 explore aspect ratio a/b effects at scaling factor in range of $S = 0.1 - 10.0$. For a given S larger a/b values accelerate fracture depletion and delay matrix depletion, amplifying the separation between the two linear-flow regimes. Conversely, at fixed a/b, an increase in S simply translates the entire response to later times, reflecting the larger matrix block.

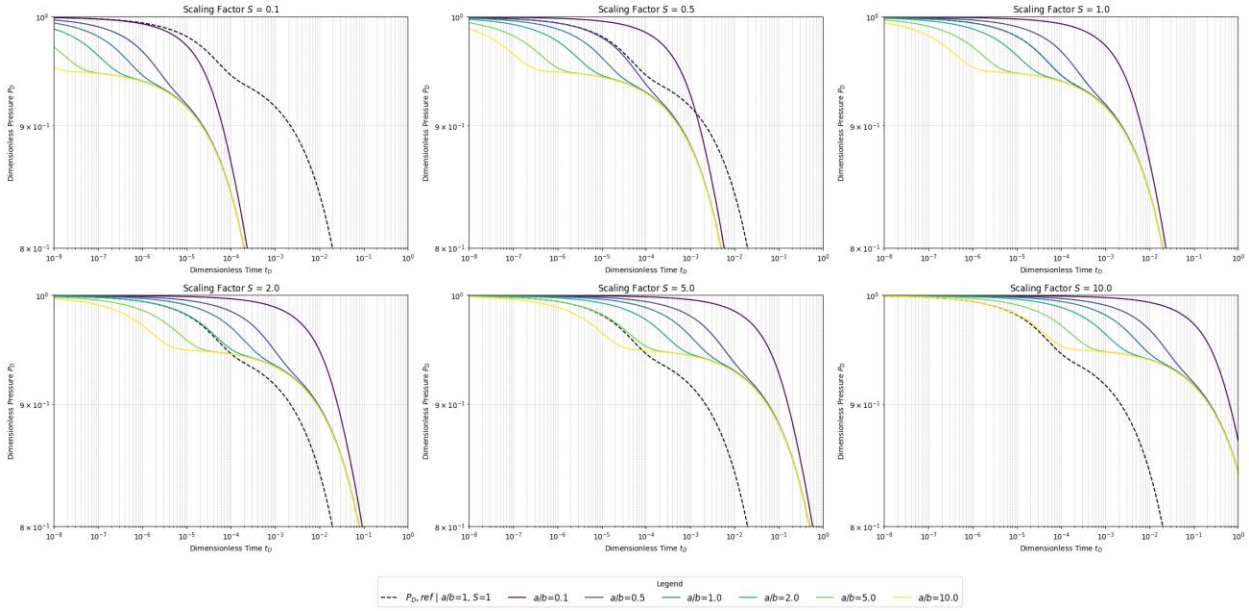

Figure 39. Dimensionless pressure P_D as a function of dimensionless time t_D for various a/b and S

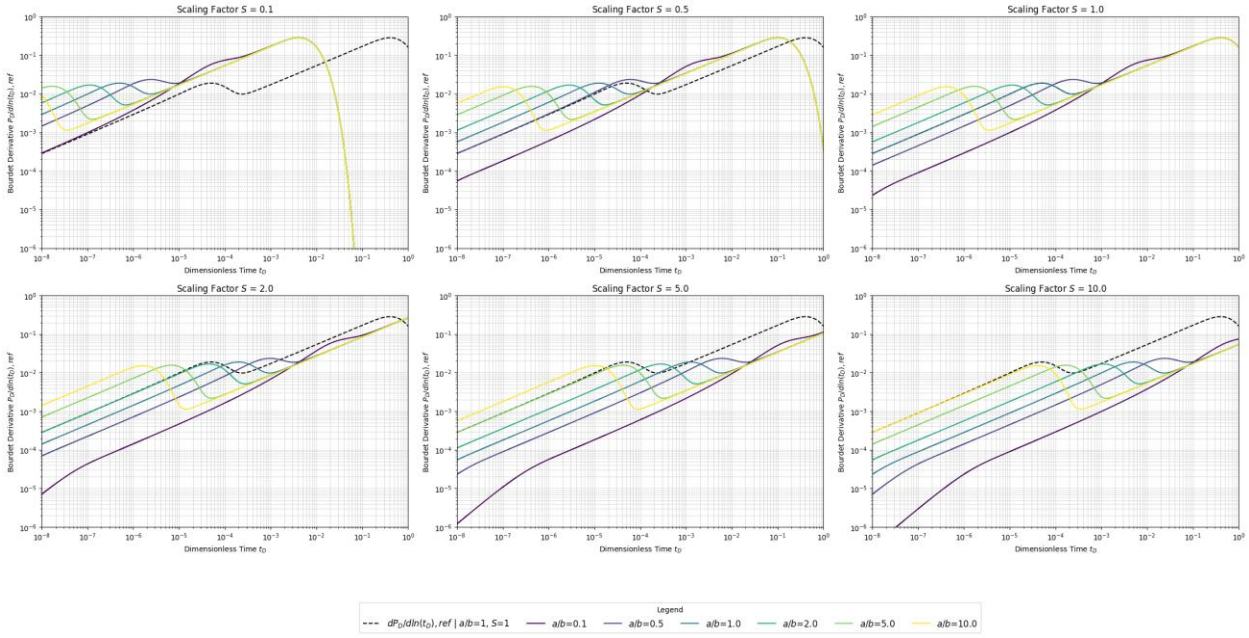

Figure 40. Bourdet derivative of dimensionless pressure as a function of dimensionless time t_D for various a/b and S

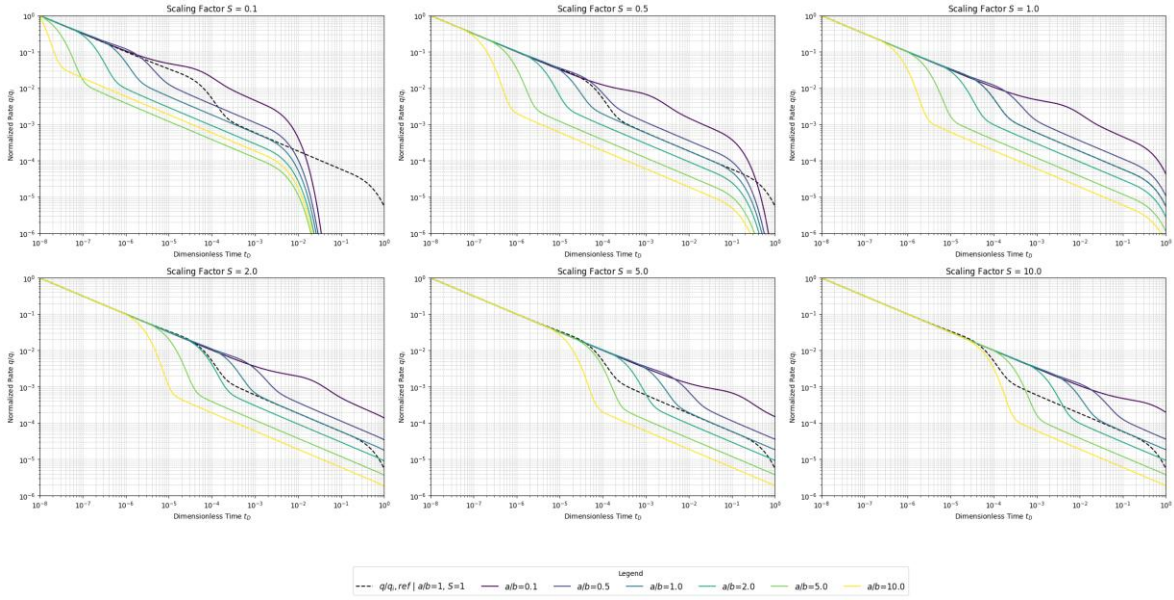

Figure 41. Normalized rate q/q_i as a function of dimensionless time t_D for various a/b and S

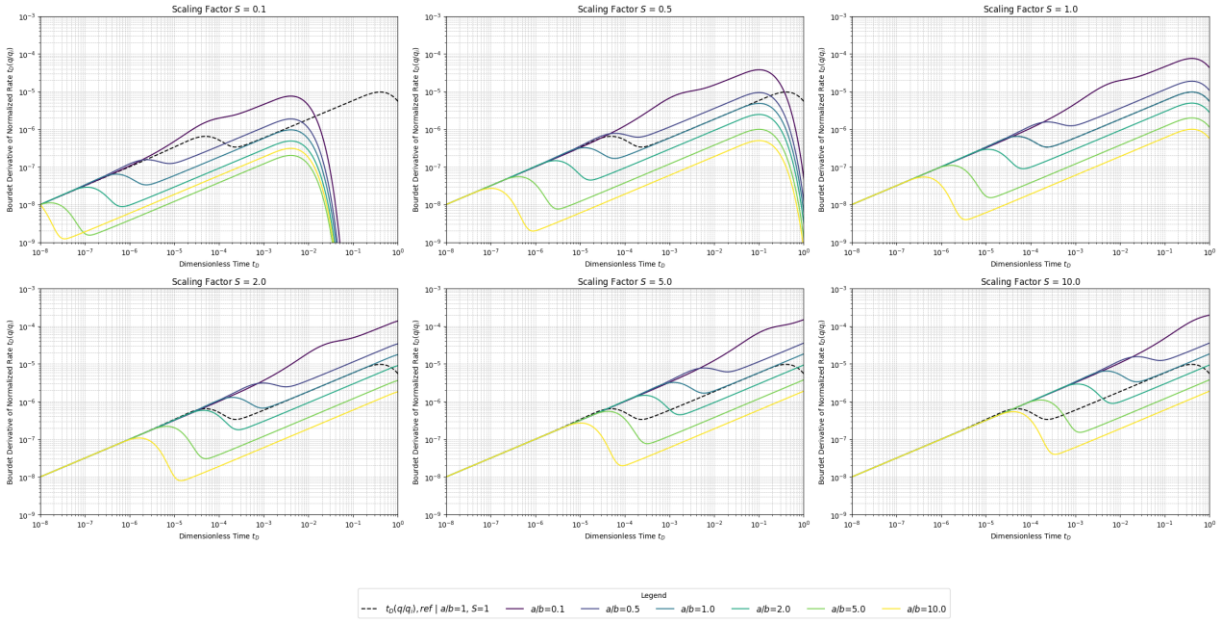

Figure 42. Bourdet derivative of normalized rate as a function of dimensionless time t_D for various a/b and S

4.2.3 Reservoir heterogeneity

To mimic heterogeneous reservoirs, volume-weighted averages were computed for mixtures of two matrix types while holding $\frac{k_f}{k_x} = 10^4$ and $v_f = 0.05$ constant. Two scenarios were considered:

- Geometry mixtures: $a/b = 1$ vs $a/b = 10$ at $S = 1$
- Size mixtures: $S = 1$ vs $S = 10$ at $a/b = 1$

Figures 43 to 46 reveal that pressure responses scale nearly linearly with the volume fraction of each matrix type, whereas rate-decline and derivative responses exhibit non-linearity – addition of 10% of $S = 10$ matrix can greatly extend transition duration. These non-linear effects are examined in detail in Chapter 5.

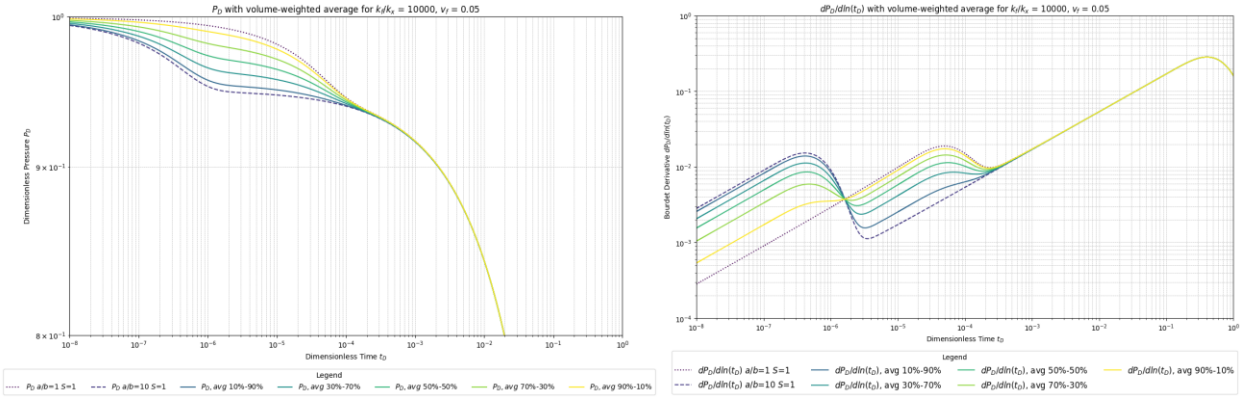

Figure 43. Volume-weighted average of dimensionless pressure and its Bourdet derivative for a reservoir with $k_f/k_x=10^4$, $v_f=0.05$, S=1 and different mixtures of aspect ratios.

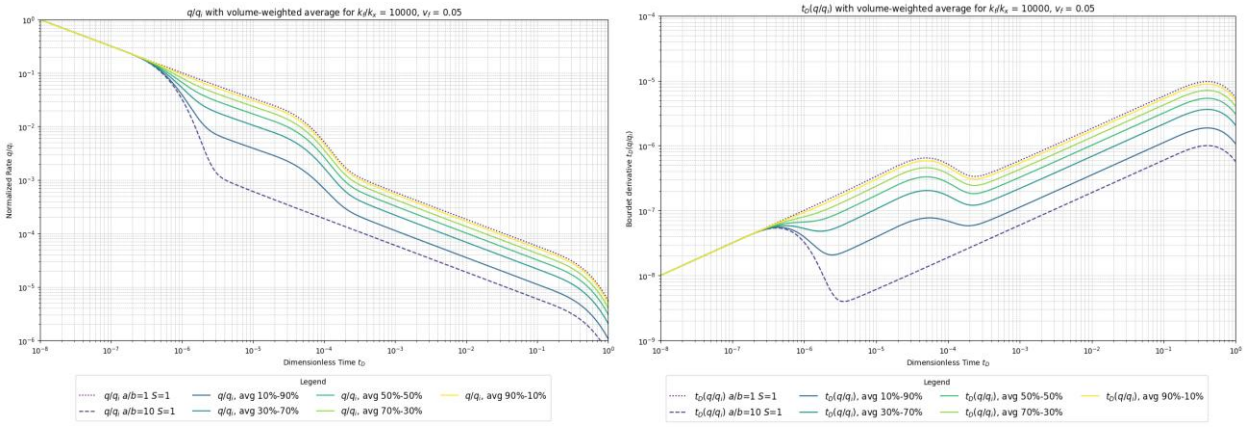

Figure 44. Volume-weighted average of normalized rate and its Bourdet derivative for a reservoir with $k_f/k_x=10^4$, $v_f=0.05$, S=1 and different mixtures of aspect ratios.

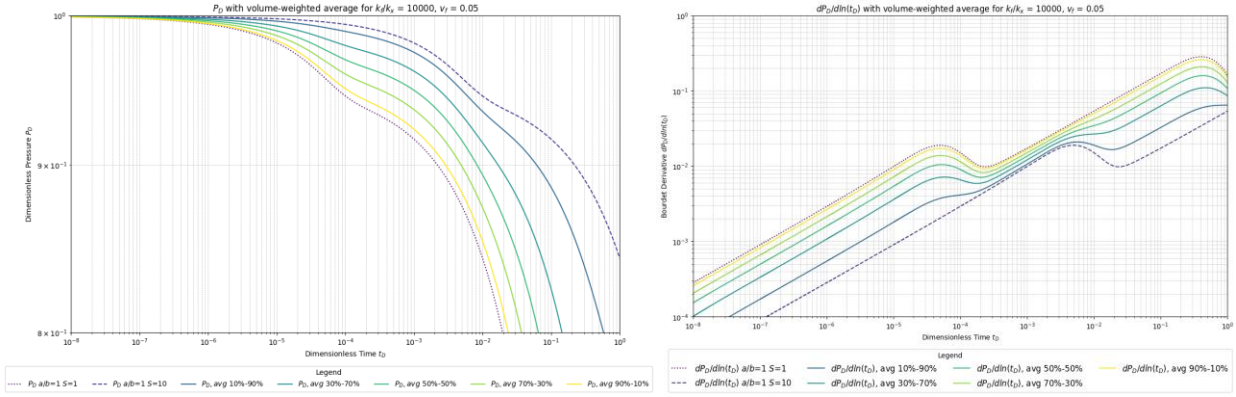

Figure 45. Volume-weighted average of dimensionless pressure and its Bourdet derivative for a reservoir with $k_f/k_x=10^4$, $v_f=0.05$, a/b=1 and different mixtures of scaling factors.

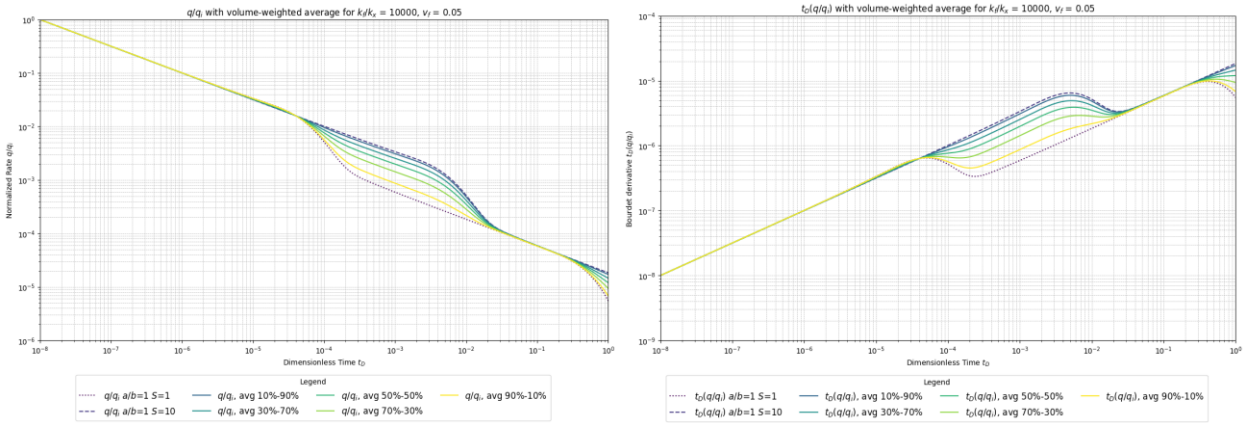

Figure 46. Volume-weighted average of normalized rate and its Bourdet derivative for a reservoir with $k_f/k_x=10^4$, $v_f=0.05$, a/b=1 and different mixtures of scaling factors.

5. DISCUSSION

5.1 Model Validation Insights

The analytical model developed herein was validated against the prior work of Hazlett et al. (2024). Comparative analysis, illustrated in Figures 21–28, corroborates that the coupled formulation converges to the Hazlett et al. (2024) solution for high permeability contrasts $k_f/k_x > 10^4$. However, for low permeability ratios of $k_f/k_x \leq 10^4$, a systematic divergence in the dimensionless pressure and rate profiles becomes evident. This departure is theoretically expected as the new solution couples matrix depletion with fracture depletion as dependent events, unlike the model used in previous work. Physically, under low permeability contrast conditions, the matrix begins feeding the fracture as it depletes, so both domains deplete near-synchronously. While, at high contrast ($k_f/k_x > 10^4$) the fracture drains substantially faster, establishing distinct fracture- and matrix-dominated flow regimes, corresponding to previous decoupled assumption.

Additionally, convergence analysis (Appendix A-1 and A-2) indicates that double summation present in matrix-fracture coupling term in a novel model, the computations take more time to converge. Therefore it may be recommended that for screening studies with $k_f/k_x > 10^4$, the approach by Hazlett et al. (2024) may offer practical advantages, potentially reducing computation times significantly (e.g., from several hours to several minutes) while maintaining acceptable accuracy for that specific regime.

It was noted that there is a discrepancy between the new and previous approaches at high k_f/k_x at $v_f < 0.01$. This finding could be explained by the increased relative contribution of matrix storage at $v_f < 0.01$, which makes the coupling effect non-negligible even in the presence of a high permeability contrast. Overall, the validation confirms the model's integrity and identifies the conditions $\left(\frac{k_f}{k_x} \leq 10^4, v_f < 0.01\right)$ under which the newly introduced coupling term provides a more physically representative description of NFR depletion.

5.2 Influence of Key Parameters on Pressure and Rate Decline

This section quantifies how each of the four governing variables — k_f/k_x, v_f, a/b, and S — modify the diagnostic metrics established in Chapter 4: half-slope gradients, intercepts, and transition duration. Systematic analysis of these metrics reveals the dominant controls on early- and late-time flow and highlights parameter combinations that produce non-linear interactions. The insights gained here may lay as the foundation for the practical recommendations and field data interpretations.

5.2.1 Permeability Ratio and Fracture Volume Fraction

Permeability ratio is a critical parameter influencing transient behavior. Figures 29-32 show that increasing permeability ratio compresses the transition zone between fracture- and matrix-dominated linear flow. Quantitative analysis of the metrics presented in Tables 8 and 9 reveals a distinct inverse relationship between k_f/k_x and the transition duration, characterized by the empirical correlation (Equation 5.1) with a high coefficient of determination $R^2 = 0.99$:

$$\frac{k_f}{k_x} = \frac{4.39}{Transition\ duration} \tag{5.1}$$

With transition duration expressed in dimensionless time units.

Qualitative inspection of the derivative plots (Figures 31-32, 36-37) suggests that an increase in k_f/k_x also results in an intense contrast between the peak and trough signatures within the transition zone. However, numerical analysis indicates that this peak-trough amplitude exhibits only a moderate correlation with k_f/k_x and v_f ($R^2 \approx 0.5$), therefore, no universal empirical relationship was proposed.

Fracture volume fraction also fundamentally affects the pressure and rate decline signatures. Higher v_f increases the relative contribution of fracture storage, resulting in an earlier onset and more rapid decline during the initial fracture-dominated flow period. The intercepts corresponding to the fracture and matrix linear flow regimes, derived via extrapolation of the half-unit slopes on the log-log Bourdet plots (summarized in Tables 8 and 9), are influenced by both v_f and k_f/k_x.

This interdependence facilitated the development of the following empirical relationships based on the dimensionless pressure derivative ($R^2 = 0.99$ for both relationships):

$$Fracture\ Intercept = -0.298 + 0.477 * \log\left(\frac{k_f}{k_x}\right) + 0.824 * \log v_f \quad (5.2)$$

$$Matrix\ Intercept = -0.27 + 0.033 * \log\left(\frac{k_f}{k_x}\right) + 0.454 * \log v_f \quad (5.3)$$

Similarly, the intercepts obtained from the Bourdet derivative of normalized rate yielded ($R^2 = 0.95$ for both relationships):

$$Fracture\ Intercept = -3.749 - 0.0693 * \log\left(\frac{k_f}{k_x}\right) + 0.1609 * \log v_f - 0.0521 * \log\left(\frac{k_f}{k_x}\right) * \log v_f \quad (5.4)$$

$$Matrix\ Intercept = -4.2546 - 0.3765 * \log\left(\frac{k_f}{k_x}\right) - 0.758 * \log v_f \quad (5.5)$$

These correlations suggest a potential diagnostic workflow for estimating fundamental NFR properties:

1. Estimating permeability ratio from transition duration using Equation (5.1).
2. Estimating fracture volume fraction using derived intercepts and the estimated permeability ratio via Equations (5.2 – 5.3) for pressure derivative analysis or Equations (5.4 – 5.5) for rate derivative analysis.

It should be noted that the range of applicability of these empirical relations corresponds to ranges of investigation defined in Table 7, which are $k_f/k_x = 10^3 - 10^6$ and $v_f = 0.005 - 0.1$.

5.2.2 Aspect Ratio and Scaling Factor

A novel contribution of this work is the explicit incorporation of the matrix aspect ratio (a/b), which characterizes the matrix block geometry—a feature absent in classical dual-porosity models (e.g., Warren & Root, Kazemi). Analysis based on Figures 39 – 42, demonstrates that for a fixed

S, the increase in a/b leads to a rapid fracture depletion and delay in a matrix depletion, amplifying the separation between the two linear-flow regimes. Mathematically, accelerated fracture depletion is governed by the $\left(\frac{a}{b}\right)^2$ factor in an exponential term of $P_f(t_D)/P_i$ (Equation 3.5). Whereas the matrix side also becomes affected by the presence of $\left(\frac{a}{b}\right)^2$ factor in fracture-matrix coupling term (Equation 3.13). Thus, this combined effect creates a more pronounced dual-porosity signature. This combined effect yields a more distinct and prolonged dual-porosity signature. Physically, increasing a/b implies a larger characteristic diffusion length within the matrix (a) relative to the fracture length (b), resulting in slower matrix diffusion rates and decreased communication between matrix and fractures.

The scaling factor was incorporated to represent variations in the characteristic matrix block dimension, enabling the analysis of size effects. Figures 39–42 illustrate that, for a constant aspect ratio (a/b), increasing S induces a purely horizontal shift of the response curves towards later times along the logarithmic dimensionless time axis, without altering the shape of the pressure or rate profiles. The magnitude of this horizontal shift translation is quantified by the relationship

$$t_D = t_{D,ref} * \frac{1}{S^2}$$

leading to a shift on the log-log plot given by:

$$Shift = \log\left(\frac{1}{S^2}\right) = -2\log S$$

For instance, increasing S from 1 to 5 results in a shift of $= -2\log 5 = 1.4$ logarithmic decades. Beyond this scaling, physically, an increased S relates to larger matrix blocks possessing greater storage capacity, thus leading to more prolonged, gradual depletion during the late-time matrix-dominated flow period.

5.2.3 Reservoir Heterogeneity

The introduction of heterogeneity effects through mixing matrix blocks of differing geometries a/b or sizes S, reveals important insights into how heterogeneity impacts overall system response

(Section 4.2.3, Figures 43-46). While the volume-weighted average dimensionless pressure P_D appeared to scale approximately linearly with the mixture fractions, the normalized rate q/q_i and, more significantly, the Bourdet derivatives ($dP_D/dlnt_D$ and $t_D(q/q_i)$) exhibited pronounced non-linear behavior. This difference emphasizes how differently pressure, rate, and rate derivatives respond to the underlying physics of flow in heterogeneous systems.

The average dimensionless pressure may exhibit apparent linear proportionality, because of its cumulative measure reflecting the overall volumetric depletion state of the combined system. It averages, thus "smoothes", the pressure contributions from all block types based on their volume fraction. However, the instantaneous flow rate and its derivative are far more sensitive to how and when different parts of the reservoir contribute to flow.

The non-linearity seen in the rate and derivative responses may result from the total system rate being the sum of contributions from matrix blocks draining on quite different timescales (controlled by S^2 and (a/b)^2). Adapted for mixtures, the governing equations for rate (Eq. 3.22) comprise sums of exponential terms dependent on these parameters. Especially, since on log-log derivative plots, all changes are magnified, a simple volume-weighted averaging of the individual rate or derivative curves does not reflect the behavior of the combined system.

Specifically, as seen in Figures 45 and 46, introducing even a small volume fraction (e.g., 10%) of larger, slower-draining blocks ($S = 10$) disproportionately affects the overall response. While the faster-draining blocks ($S = 1$) dominate the early-time behavior, the slower blocks continue to contribute significantly during the later stages of depletion. This has several key effects on the derivative plots:

1. Extended transition: The contribution from the bigger blocks prolongs the transition period between fracture-dominated and matrix-dominated flow, smoothing the characteristic trough observed in homogeneous systems.

2. Altered derivative shape: The derivative curve shape becomes a composite, thus making it hard to see the separate behaviors of different blocks. The matrix linear flow is delayed and may reflect the properties of the slowest-draining blocks present, even if they represent a small volume fraction.

3. Amplified sensitivity: Since the Bourdet derivative amplifies changes in the rate of production decline, the contribution from slow-draining blocks may significantly alter this rate of change during the transition and late-time periods, leading to a derivative shape that cannot be predicted or interpreted by simply averaging the derivative shapes of the constituent homogeneous systems based on volume fraction.

Similar effects are observed when mixing blocks of different aspect ratios (Figures 43 and 44), as aspect ratio also influences the characteristic depletion timescales.

Physically, this non-linearity signifies that heterogeneity causes a smoothing of flow regimes across the reservoir. Different matrix blocks are simultaneously experiencing different phases of depletion: fracture depletion, transition zone, and matrix depletion. The rate derivative captures this complex mix, while the average pressure provides a more smoothed-out picture. This implies that interpreting rate-transient data from heterogeneous NFRs requires models that explicitly account for the distribution of matrix properties, as simple averaging of homogeneous type curves based on volume fractions can be misleading, particularly when relying on derivative analysis for flow regime identification and parameter estimation.

5.3 Comparison with Commercial Software Approaches

This section compares model of this study with commercial software approaches, particularly Saphir, Pressure Transient Analysis module at KAPPA-Workstation, by KAPPA.

In The Dynamic Data Analysis (DDA) book by KAPPA Engineering (2023), the dual porosity reservoirs are modeled similar to Warren & Root (1963) approach. Reservoir is assumed to consist of matrix blocks and fractures surrounding them. The fluid flow is carried out from matrix to fractures and from fractures to the well as depicted in Figure below. The dual porosity system properties are quantified via:

- Storativity ratio $\omega = \frac{(V\Phi c_t)_f}{(V\Phi c_t)_f + (V\Phi c_t)_m}$

- Interporosity flow coefficient $\lambda = \alpha r_w^2 \frac{k_m}{k_f}$, where α is geometrical coefficient of matrix block.

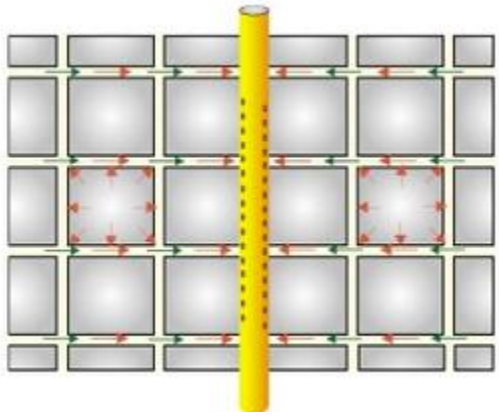

Figure 47. Dual porosity reservoir approximation by KAPPA *(Houzé, Viturat, & Fjaere, 2023)*

It can be observed that these parameters are similar to the new coupled model, however still have differences. Storativity ratio ω is conceptually analogous to fracture volume fraction v_f, whereas interporosity flow coefficient λ is an inverse of permeability ratio k_f/k_x. However, both v_f and k_f/k_x are direct measurements of dual porosity system, whereas ω and λ are composite parameters. Specifically, λ lumps matrix block geometry coefficient α to the permeability contrast. They are derived from matching transient well test responses and represent the system's bulk behavior, potentially obscuring the individual contributions of the underlying physical properties compared to the more direct parameters used here.

Additionally, Saphir module considers both PSS and transient interporosity flow. Particularly, for transient interporosity flow, Saphir model assumes pressure gradient within the matrix blocks and thus depending on the significance of pressure profile inside the blocks, the matrix block geometry coefficient α should be considered. In this study, the pressure gradient is not considered in the matrix blocks, but rather average value is computed.

6. CONCLUSION AND RECOMMENDATIONS

6.1 Conclusions

In this study, an enhanced analytical REV model incorporating fracture-matrix coupling for NFR depletion analysis was successfully developed and formulated. The new model converges to previous decoupled solutions (Hazlett et al., 2024) under conditions of high permeability contrast ($k_f/k_x > 10^4$), validating its formulation. Significant departures from decoupled models occur at lower permeability contrasts ($k_f/k_x \leq 10^4$) and low fracture volume fractions ($v_f < 0.01$), highlighting the importance of the coupling term under these conditions, providing a more physically representative description.

Sensitivity analysis identified distinct influences of key parameters:

- k_f/k_x primarily controls the duration of the transition between fracture-dominated and matrix-dominated flow regimes.
- v_f affects the intercepts of the linear flow regimes and the magnitude contrast during the transition.
- Matrix aspect ratio (a/b) influences the timing and separation of fracture and matrix depletion signatures.
- Scaling factor (S) introduces a predictable time shift in the response curves, reflecting matrix block size effects.

Based on the conducted sensitivity analysis, empirical correlations were developed relating transient diagnostic features (transition duration, intercepts) to reservoir parameters (k_f/k_x, v_f), offering a potential workflow for parameter estimation.

Analysis of heterogeneous mixtures revealed non-linear behavior in rate and derivative responses, demonstrating that simple volume-weighted averaging of homogeneous type curves can be misleading, especially for derivative analysis. Even small fractions of slower-draining blocks significantly impact the overall system response and derivative shape.

The coupled model, while more computationally intensive due to the double summation term, provides necessary accuracy for systems where fracture and matrix depletion timescales are not vastly different.

6.2 Recommendations for Future Work

Based on the assumptions, limitations, and outcomes of the study the following recommendations for future work can be considered:

- Extend the model to incorporate multi-phase flow to broaden its applicability.
- Investigate the impact of more complex fracture network geometries beyond simple parallel fractures.
- Explore the inclusion of non-uniform initial pressure distributions or more complex boundary conditions.
- Develop methods to handle distributions of matrix block properties (size, aspect ratio, permeability) beyond simple binary mixtures to better represent complex reservoir heterogeneity.
- Apply the developed model and diagnostic techniques to analyze real field production data from NFRs to test its practical utility and identify parameter range. Compare the model results with the commercial software such as Saphir (by KAPPA) and analyze differences and/or limitations of each approach.
- Investigate the potential for optimizing the numerical evaluation of the double-summation terms to reduce computation time for the coupled model.

7. REFERENCES

Aguilera, R. (1980). *Naturally Fractured Reservoirs* (2nd ed.). Tulsa: PennWellBooks.

Aguilera, R. (1983). Exploring for Naturally Fractured Reservoirs. *SPWLA 24th Annual Logging Symposium.* Calgary: Society of Petrophysicists and Well-Log Analysts.

Ahmed, T. (2019). *Reservoir Engineering Handbook* (5th ed.). Gulf Professional Publishing.

Arps, J. (1945). Analysis of Decline Curves. *Transactions*, 228-247. doi:10.2118/945228-G

Bahrami, N., Pena, D., & Lusted, I. (2016). Well test, rate transient analysis and reservoir simulation for characterizing multi-fractured unconventional oil and gas reservoirs. *Journal of Petroleum Exploration Production Technology,* 675-689. doi: 10.1007/s13202-015-0219-1

Barenblatt, G. I., Zheltov, I. P., & Kochina, I. N. (1960). Basic concepts in the theory of seepage of homogeneous liquids in fissured rocks [strata]. *Journal of applied mathematics and mechanics, 24*(5), 1286-1303.

Berkowitz, B., Bour, O., Davy, P., & Odling, N. (2000). Scaling of fracture connectivity in geological formations. *Geophysical Research Letters, 27*(14), 2061-2064. doi:10.1029/1999GL011241

Bonnet, E., Bour, O., Odling, N. E., Davy, P., Main, I., Cowie, P., & Berkowitz, B. (2001). Scaling of fracture systems in geological media. *Reviews of Geophysics, 39*(3), 347-383. doi:10.1029/1999RG000074

Carslaw, H. S., & Jaeger, J. C. (1959). *Conduction of Heat in Solids.* Oxford University Press.

Cooke, M., & Underwood, C. (2001). Fracture termination and step-over at bedding interfaces due to frictional slip and interface opening. *Journal of Structural Geology, 23*(2-3), 223-238. doi:10.1016/S0191-8141(00)00092-4

De Swaan, O. A. (1976). Analytic solutions for determining naturally fractured reservoir properties by well testing. *Society of Petroleum Engineers Journal, 16*(3), 117-122.

Dershowitz, W. S., & Herda, H. H. (1992). Interpretation of fracture spacing and intensity. *The 33rd U.S. Symposium on Rock Mechanics (USRMS).* Santa Fe. doi:ARMA-92-0757

Duguid Jr, J. O. (1973). Flow in porous media. *Doctoral dissertation, PhD thesis*. Princeton University.

Duong, A. N. (2011). Rate-Decline Analysis for Fracture-Dominated Shale Reservoirs. *SPE Reservoir Evaluation & Engineering,* 377-387. doi:10.2118/137748-PA

Ghosh, K., & Mitra, S. (2009). Two-dimensional simulation of controls of fracture parameters on fracture connectivity. *AAPG Bulletin, 93*(11), 1517-1533. doi:10.1306/07270909041

Gomaa, S., Gouda, A., Mohamed, E., Ragab, G., Hesham, A., El-Faramawy, A., & Ahmed, R. (2020). Buildup Test Analysis in Naturally Fractured Oil Reservoir. *International Journal of Petroleum and Petrochemical Engineering, 6*(2), 23-35. doi:10.20431/2454-7980.0602004

Han, Z., Wang, C., Jiao, Y. Y., Wang, C., & Wang, J. (2020). A proposed method for mathematical quantitative description of fractures from borehole wall images. *IOP Conference Series: Earth and Environmental Science.* doi:10.1088/1755-1315/570/4/042001

Hazlett, R. D., Farooq, U., & Babu, D. K. (2021). A complement to decline curve analysis. *SPE Journal, 26*(04), 2468-2478.

Hazlett, R. D., Syrymov, T., & Younis, R. (2024). Analytic representative element rate decline models for naturally fractured reservoir depletion. *Scientific Reports*. doi:10.1038/s41598-024-59023-5

Hill, R. (1963). Elastic properties of reinforced solids: Some theoretical principles. *Journal of the Mechanics and Physics of Solids, 11*(5), 357-372. doi:10.1016/0022-5096(63)90036-X

Houzé, O., Viturat, D., & Fjaere, O. S. (2023). *Dynamic Data Analysis.* KAPPA Engineering. Retrieved 2025 from https://www.kappaeng.com/documents/flip/dda560/

Huitt, J. L. (1956). Fluid Flow in Simulated Fractures. *AIChE Journal*, 259-264. doi:10.1002/aic.690020224

Ilk, D., Rushing, J. A., Perego, A. D., & Blasingame, T. (2008). Exponential vs. Hyperbolic Decline in Tight Gas Sands — Understanding the Origin and Implications for Reserve Estimates Using Arps' Decline Curves. *SPE Annual Technical Conference and Exhibition.* Denver. doi:10.2118/116731-MS

Kazemi, H. (1969). Pressure transient analysis of naturally fractured reservoirs with uniform fracture distribution. *Society of petroleum engineers Journal, 9*(4), 451-462.

McNaughton, D. A., & Garb, F. A. (1975). Finding and evaluating petroleum accumulations in fractured reservoir rock. *Exploration and Economics of the Petroleum Industry*, 23-49.

Najurieta, H. L. (1980). A theory for pressure transient analysis in naturally fractured reservoirs. *Journal of Petroleum Technology, 32*(7), 1241-1250.

Narr, W., Schechter, D. S., & Thompson, L. B. (2006). *Naturally Fractured Reservoir Characterization.* Richardson: Society of Petroleum Engineers.

Nelson, R. A. (2001). *Geologic Analysis of Naturally Fractured Reservoirs* (2nd ed.). Houston: Gulf Professional Publishing.

Odeh, A. S. (1965). Unsteady-state behavior of naturally fractured reservoirs. *Society of Petroleum Engineers Journal, 5*(1), 60-66.

Odling, N. E. (1997). Scaling and connectivity of joint systems in sandstones from western Norway. *Journal ofStructural Geology, 19*(10), 1257-1271.

Odling, N. E., Gillespie, P., Bourgine, B., Castaing, C., Chiles, J., Christensen, N., . . . Trice, R. (1999). Variations in fracture system geometry and their implications for fluid flow in fractures hydrocarbon reservoirs. *Petroleum Geoscience, 5*(4), 373-384.

Ozkaya, S. I., & Mattner, J. (2003). Fracture connectivity from fracture intersections in borehole image logs. *Computers & Geosciences, 29*, 143-153.

Parsons, R. (1966). Permeability of idealized fractured rock. *Society of Petroleum Engineers Journal, 6*(2), 126-136.

Reiss, L. H. (1976). Reservoir engineering in fractured reservoirs. *French Institute of Petroleum*.

Robertson, S. (1988). Generalized Hyperbolic Equation. *SPE*.

Rubino, G. J., Guarracino, L., Muller, T. M., & Holliger, K. (2013). Do seismic waves sense fracture connectivity? *Geophysical Research Letters, 40*, 692-696. doi:10.1002/grl.50127

Sanderson, D., & Nixon, C. (2018). Topology, connectivity and percolation in fracture network. *Journal of Structural Geology*, 167-177.

Sharp, J., Maini, Y., & Brekke, T. (1972). Evaluation Of Hydraulic Properties Of Rock Masses. *The 14th U.S. Symposium on Rock Mechanics (USRMS).* Pennsylvania.

Snow, D. T. (1968). Rock Fracture Spacings, Openings, and Porosities. *Journal of the Soil Mechanics and Foundations Division*. doi:10.1061/JSFEAQ.0001097

Snow, D. T. (1969). Anisotropie Permeability of Fractured Media. *Water Resources Research, 5*(6), 1273-1289. doi:10.1029/WR005i006p01273

Streltsova, T. D. (1983). Well Pressure Behavior of a Naturally Fractured Reservoir. *SPE*, 769-780. doi:10.2118/10782-PA

Sun, S., & Pollitt, D. A. (2021). Optimising development and production of naturally fractured reservoirs using a large empirical dataset. *Petroleum Geoscience, 27*. doi:10.1144/petgeo2020-079

Valkó, P. P., & Lee, J. W. (2010). A Better Way To Forecast Production From Unconventional Gas Wells. *SPE*.

van Golf-Racht, T. D. (1982). *Fundamentals of fractured reservoir engineering.* Elsevier Scientific Publishing Company.

Vermilye, J. M., & Scholz, C. H. (1995). Relation between vein length and aperture. *Journal of Structural Geology, 17*(3), 423-434. doi:10.1016/0191-8141(94)00058-8

Warren, J. E., & Root, P. J. (1963). The behavior of naturally fractured reservoirs. *Society of Petroleum Engineers Journal, 3*(3), 245-255.

Warrlich, G., Taberner, C., Asyee, W., Stephenson, B., Esteban, M., Boya-Ferrero, M., . . . Van Konijnenburg, J.-H. (2010). The Impact of Postdepositional Processes on Reservoir Properties: Two Case Studies of Tertiary Carbonate Buildup Gas Fields in Southeast Asia (Malampaya and E11). In W. Morgan, A. D. George, P. Harris, J. Kupecz, & J. F. Sarg, *Cenozoic Carbonate Systems of Australasia* (pp. 99-127). SEPM. doi:10.2110/sepmsp.095.99

Witherspoon, P. A., & Gale, J. E. (1977). Mechanical and hydraulic properties of rocks related to induced seismicity. *Engineering Geology, 11*(1), 23-55.

8. APPENDICES

Appendix A

Table A-1. Maximum number of dummy variables *m* and *n* used to reach convergence of tolerance 10^{-6}

Equation	Matrix contribution			Fracture contribution
	Single sum	Double sum		Single sum
	m_{max}	m_{max}	n_{max}	n_{max}
Equation (3.20) $\left(\frac{\bar{P}(t)}{P_i}\right)_{new}$	495	501	1	489
Equation (3.21) $\left(\frac{d\left(\frac{\bar{P}(t)}{P_i}\right)}{dlnt_D}\right)_{new}$	12125	132778	11	304
Equation (3.23) $\left(\frac{\bar{P}(t)}{P_i}\right)_{prev}$	495	-	-	489
Equation (3.24) $\left(\frac{d\left(\frac{\bar{P}(t)}{P_i}\right)}{dlnt_D}\right)_{prev}$	304	-	-	304

Table A-2. Maximum number of dummy variables *m* and *n* used to reach convergence of tolerance 10^{-6}

Equation	Matrix contribution			Fracture contribution
	Single sum	Double sum		Single sum
	m_{max}	m_{max}	n_{max}	n_{max}
Equation (3.22) q_{new}	11832	493871	489	8367

$\left(t_D * \frac{q}{q_i}\right)_{new}$	11832	493871	2	8367
Equation (3.25) q_{prev}	11832	-	-	8367
$\left(t_D * \frac{q}{q_i}\right)_{prev}$	11832	-	-	8367